Recent Advances in Vanadium-based Nanomaterials and Their Composites as High-performance Electrode Materials for Supercapacitors

Journal:	*Sustainable Energy & Fuels*
Manuscript ID	SE-REV-06-2020-000897.R1
Article Type:	Review Article
Date Submitted by the Author:	14-Jul-2020
Complete List of Authors:	Qin, Huizhen; Chongqing University Liang, Shunfei; Chongqing University Chen, Lingyun; Chongqing University, Department of Application Chemistry, School of Chemistry and Chemical Engineering Li, Yang; Chongqing University Luo, Ziyang; Chongqing University Chen, Shaowei; University of California, Department of Chemistry and Biochemistry

Recent Advances in Vanadium-based Nanomaterials and Their Composites for Supercapacitors

Huizhen Qin[a], Shunfei Liang [a], Lingyun Chen [a,*], Yang Li [a], ZiyangLuo [a], Shaowei Chen [b,*]

[a] School of Chemistry and Chemical Engineering, Chongqing University, Chongqing 400044, China

[b] Department of Chemistry and Biochemistry, University of California, 1156 High Street, Santa Cruz, California 95060, United States

* E-mail addresses: lychen@cqu.edu.cn (L. Chen) and shaowei@ucsc.edu (S. Chen)

Abstract

In recent years, supercapacitors (SCs) have attracted great attention in the field of energy storage, and design and engineering of effective electrode materials represent a critical part of the research efforts. Towards this end, vanadium (V)-based nanocomposites are of particular interest, primarily because vanadium possesses a variety of valence states (i.e., V^{2+}, V^{3+}, V^{4+}, and V^{5+}) and is low-cost. In this review article, there are mainly vanadium oxides, vanadium nitrides, vanadium sulfides, and mixed metal vanadates for V-based materials. And these compounds do their unique properties. In addition, recent advances in the preparation and electrochemical activity of V-based nanocomposites for SCs applications will be summarized, within the context of synthetic methods, nanocomposite morphologies, and electrochemical performances. This review is concluded with a perspective, where promises and challenges of functional nanocomposites for SCs applications will be highlighted.

KEYWORDS: Vanadium-based nanomaterials; Vanadium oxide; Vanadium sulfide; Vanadium nitride; Supercapacitor; Electrochemical Energy Storage

1 Introduction

The ever-increasing energy depletion and environmental deterioration issues have prompted people to conduct in-depth research on the development of new energy and environmental benignity energy storage system. In recent years, with the increasing progress of society, lithium-ion battery has become the most widely used energy storage system due to its advantages of high energy density, long service life, no memory effect, and low cost.[1] However, lithium in lithium-ion batteries is restricted in nature. Developing innovation energy storage equipment as much as possible is the current research focus. Supercapacitors (SCs), also known as electrochemical capacitors, gold capacitors, and Faraday capacitors, are a new type of energy storage device between batteries and plate capacitors. SCs, which are the new generation of energy storage equipment, have been broadly used in applications such as communication equipment, hybrid electric vehicles, and portable electronics, due to their high specific power (>10 $kW \cdot kg^{-1}$), rapid charge/discharge capability (within seconds), long cycle lifetimes (>100 000 cycles), and environmental friendliness.[2-4] According to the charge storage mechanism, SCs can be classified into two categories: electrochemical double-layer capacitors (EDLCs), and pseudocapacitors (PCs) that exhibit a much higher capacitance. Mechanistically, charge/discharge arises from adsorption/desorption of ions at the electrode-electrolyte interface in the former, whereas it is primarily due to faradaic redox reactions of electroactive materials in the latter.[5, 6] In addition, the hybrid capacitor, assembling with electrode materials of EDLCs and PCs, was proposed. Its energy storage mechanism is relatively complicated, and it is generally considered to have both EDLCs and PCs mechanism. The use of electroactive electrode materials with a high surface area and redox-active mediators represents a critical strategy to enhance the capacitive performance, as the energy density (E) of a SC is depending on the capacitance (C) and the operating potential window (V), $E = 1/2\ CV^2$.

To meet the ever-increasing demand for high-performance SCs, a range of electrode materials have been developed, including oxides[7] sulfides[8], nitrides[9], and tellurides of transition metals[10], conductive polymers[11], and carbon-based materials[12], and their corresponding advantages and disadvantages are shown in table 1. For example, Theerthagiri et al. discussed recent progress and emerging challenges of transition metal sulfides, and summarized corresponding electrode materials for electrochemical supercapacitive energy storage.[8] Shi et al. emphasized on the current evolution of transition metal nitrides and transition metal nitrides/carbon nanocomposites.[9] As mentioned above, transition metal oxides (TMOs) as electrode materials in energy storage devices, especially in SCs, have attracted great attention of researchers, such as RuO_2, MnO_2, Co_3O_4, and so on.[13] However, RuO_2 for traditional TMOs has been limited to its practical application in SCs by its low abundance, toxicity, and high cost. Therefore, the TMOs electrode materials for widely used SCs by people must have the advantages of high theoretical capacity, environmental friendliness, low cost, and abundant resources.

The content of vanadium (V) is about 0.02% of the earth's crust, and it is a trace element widely distributed on the earth. Due to the existence of multiple valence states of vanadium, many materials exist in nature. For example, vanadium oxide has several forms, such as vanadium dioxide, vanadium trioxide, vanadium pentoxide, and so on. And most V-based materials are non-toxic or slightly toxic, and the price is cheap. And V-based materials have been applied as electrode materials in SCs due to various oxidation states. In addition, V-based materials, which have several merits, such as unique layered structure, low cost, easy availability, wide potential window, high energy density, and novel physical and chemical properties, is ideal energy storage material.

However, V-based materials are unstable during charging and discharging and are easy to be converted into other substances, resulting in their electrochemical and cycle performance not reaching the ideal values. It is well known that the composition, crystal phase and morphology of V-based materials have a significant influence on electrochemical properties. Some effective approaches including element doping, metal/metal compound combination, carbon material, conductive polymer or nanostructure design have been adopted to compensate the aforementioned limitations of V-based materials. In addition, V-based materials have been extensively studied, and their synthesis methods include the hydrothermal method, co-precipitation method, solvothermal method, sol-gel method, electrodeposition method, chemical vapor deposition method, electrospinning method, spray drying and wet impregnation method, and so on. This review can understand the current situation and the development of V-based materials in the future.

2 The crystal structure of vanadium-based material and its electrochemical reaction

Vanadium(IV) dioxide (VO_2) has different polymorphs, including VO_2(B), VO_2(M), VO_2(R), and VO_2(A), which can be converted into each other in near room temperature. In VO_2, the transformation of the first-order monoclinic (M) insulator phase to rutile (R) metallic phase was found, and its electrical and optical properties changed greatly.[14-16] Fig. 1a shows a crystal structure of VO_2(M) (space group P21/c (No.14)), with unit cell parameters of a = 0.575 nm, b = 0.452 nm, c= 0.538 nm, and β =122.6°, its long-distance for V-V bonds is 0.312 nm and short space is 0.265

nm. The crystal structure of VO_2(R) with the space group of P24/mnm (No. 136) is shown in Fig. 1b, and its cell parameters are: a = b = 0.455 nm, c = 0.286 nm, and the distance between the nearest V-V atoms is 0.287 nm. The d electrons of each V atom in VO_2(R) are bound to these V-V bonds resulting in the insulating properties. Vanadium(III) trioxide (V_2O_3) exhibit a rhombohedral corundum-type structure at ambient temperature, due to the formation of three-dimensional (3D) V-V chains and a twisted octahedron composed of the oxygen atoms around the vanadium sites (Fig. 1f). Because V^{3+} on the V_2O_3 surface can be easily oxidized into V^{4+} or V^{5+} in air, V_2O_3 shows low stability. Vanadium pentoxide (V_2O_5) crystallizes, is another common oxide of vanadium, which typically crystallizes into a layered structure, displaying an orthorhombic unit cell with the Pmmn space group and lattice constants of a = 1.1512 nm, b = 1.3564 nm, c = 0.4368 nm.[17-21] It consists of distorted VO_5 square pyramids periodically arranged up and down by sharing the edges and corners, as shown in Fig. 1e. Due to a weak van der Waals force, the layered structure can easily accommodate metal ions, a unique feature conducive for energy storage. In addition, Fig. 1d depicts $V_2O_5{\cdot}nH_2O$ structure with specific properties, different from V_2O_5.

For other vanadium compounds, vanadium nitride (VN) is cubic structure (space group Fm-3m (225); a = 4.1328(3) Å; V = 70.588(9) Å^3; Z = 4) (Fig. 1c), and has lower electronic conductivity than other transition metal nitrides.[22-24] Vanadium sulfides mainly consist of VS_2 and VS_4. VS_2 exhibits a layered structure and metallic conductivity.[25] VS_2 presents a two-dimensional (2D) sandwiched S-V-S layer with an interlayer space of 0.576 nm (Fig. 1g).[26] VS_4 is a chain-like structure in which the V atom is bridged to S_2^{2-}, as shown in Fig. 1h.[27] $Co_2V_2O_8$ and $Ni_2V_2O_8$ both exhibit an orthorhombic structure with somewhat different cell parameters, a = 8.24 Å, b = 11.38 Å, and c = 5.906 Å for the former, and a = 8.3 Å, b = 11.50 Å, and c = 6.030 Å for the latter.[28]

When used as a SC electrode, these materials will undergo electrochemical reactions, as listed below in varied electrolytes (Fig. 1i depicts the reactions of VO_2):

VO_2 (Na_2SO_4): $VO_2 + xNa^+ + xe^- \leftrightarrow Na_xVO_2$ (1)

V_2O_3 (Na_2SO_4): $V_2O_3 + xNa^+ + xe^- \leftrightarrow Na_xV_2O_3$ (2)

V_2O_5 ($LiNO_3$): $V_2O_5 + xLi^+ + xe^- \leftrightarrow Li_xV_2O_5$ (3)

VN (KOH): $VN_xO_y + OH^- \leftrightarrow VN_xO_y // OH^- + VN_xO_y\text{-}OH$ (4)

VS_2 (KOH): $VS_2 + OH^- \leftrightarrow VS_2OH + e^-$ (5)

VS_4 (KOH): $VS_4 + OH^- \leftrightarrow VS_4OH + e^-$ (6)

$Co_2V_2O_8$ (KOH): $Co^{2+} + 3OH^- \leftrightarrow CoOOH + H_2O + e^-$ (7)

$Ni_2V_2O_8$ (KOH): $Ni^{2+} + 3OH^- \leftrightarrow NiOOH + H_2O + e^-$ (8)

During the electrochemical test, V-based materials (vanadium oxides or vanadium nitride) may be oxidized or dissolved into an oxide in the aqueous electrolyte, and its oxide is represented by VO_x. The possible electrochemical reactions are as follows:

VO_x (KOH): $VO_x + yK^+ + ye^- \leftrightarrow K_yVO_x$ (9)

In order to prevent the dissolution or oxidation of V-based materials, various strategies have been proposed: 1) Synthetic composites, that is, nanostructured materials synthesized with carbon materials and/or conductive polymers; 2) Gel electrolyte; 3) Add a protective film layer (carbonaceous thin film).

However, the electrochemical reaction of V-based materials in SCs is similar to that of batteries, and it is easy to cause confusion. In fact, their reaction mechanism is completely different. In SCs, the highly reversible Faraday reaction stores charge on or near the surface of the electrode active material, that is, the electrode material does not undergo a phase change. In batteries, the active electrode or ions in electrolyte react reversibly to store and release charge. In other words, SCs come from delocalized electron transfer, and battery behavior is localized valence electron transfer.[29]

3 The synthesis method

It is important for the morphology and structure of V-based materials to choose the synthesis method. Various synthesis techniques have been developed to meet the preparation need of materials. We mainly introduce several commonly used synthesis method.

3.1 Hydrothermal and solvothermal method

Hydrothermal method is a method of dissolving and recrystallizing insoluble substances under high temperature and high pressure in a closed reaction container with aqueous solution as reaction medium.[19] It can adjust the reaction conditions and control the crystal structure, crystal morphology and crystal grain purity of materials Compared with other methods, the main differences are temperature (130-250 °C) and pressure (0.3-4 MPa). The solvothermal technique, like hydrothermal method, is a method of reacting raw materials in a closed system at a certain temperature and pressure. The biggest difference between the two methods is that the solvent of hydrothermal method is water, and the solvothermal method is organic solvent or non-aqueous solvent.[30] Most V-based materials can be fabricated by hydrothermal method, such as VO_2 nanosheets[31], VO_2(B) hollow spheres[32], V_2O_3@C core-shell nanorods[33], porous VN nanowires[34], $NiCo_2S_4$@VS_2[35], and

$Co_3V_2O_8$-$Ni_3V_2O_8$ nanocomposite[36]. Some was synthesized by solvothermal technique.

3.2 Sol-gel method

The sol-gel method is a low-temperature wet-chemistry method, in which raw materials are uniformly mixed to synthesis new material (metal oxide) in process of chemical solution converted into sol and then gel.[37] Generally, typical raw materials that include metal alkoxides and metal chlorides are mixed in the liquid phase and undergo hydrolysis and condensation reactions to form a stable transparent sol system. After aging, a gel with a 3D network structure is formed. In this method, metal oxide is fabricated by connecting metal center to oxo (M-O-M) or hydoxo (M-OH-M) to generate metal-oxo or metal-hydroxo polymers. Then polymer is deposited on the substrate to form specific structure. Kiruthiga et al. successfully prepared V_2O_5@rGO nanorods by combining V_2O_5 obtained by sol-gel method and rGO obtained by the modified Hummers method.[38] Wu et al. firstly synthesis V_2O_5 sol and then multi-walled carbon nanotubes (MWCNTs) aqueous dispersion was add in sol to fabricate 3D V_2O_5/MWCNTs hybrid aerogel.[39]

3.3 Chemical vapor deposition

Chemical vapor deposition (CVD) is a common industrial method that one or more volatile precursors react and/or decompose on the gas phase or gas-solid interface to generate deposits.[40] The CVD include atmospheric pressure, low pressure, ultrahigh vacuum, laser, metal-organic, plasma enhanced CVD. And those techniques with gases of different pressures and specific flows have been successfully applied to various fields. Many scientists have devoted themselves to the development of high-quality materials by CVD, and found that the main factors are as follows: 1) The selection of the partial pressure of the reaction mixture and its relative ratio; 2) Deposition temperature; 3) Substrate material; 4) Total pressure and total gas flow rate in the system; 5) Reaction gas device (sealing, reaction tube, gas pipeline material, etc.); 6) Purity of raw materials. The CVD technique for V-based materails based on organometallic precursors is called organometallic CVD or metal-organic CVD. Basu et al. reported VO_2 nanoporous structure using carbon paper (an open mesh of carbon fibers) as substrate in different Ar flows.[41] VN-graphene foams, in which graphene synthesized via CVD by using Ni foam as the growth substrate and methane as the carbon source and employing the gas flow recipe: CH_4 (30 sccm (standard cubic centimeter per minute)), H_2 (50 sccm), and Ar (150 sccm) in ambient pressure at 1000 °C for 30 min, was reported by Yu et al.[42]

3.4 Electrospinning method

Electrospinning technology is a continuous and universal method to obtain superfine fibers below micron level. The electrospinning device is mainly composed of three parts: high voltage DC power supply, spinning device and target electrode. High-voltage DC power supply provides high voltage for high-power stretching of charged polymer. The as-prepared fibers have small diameter, large specific surface area, high porosity and consistent fineness. Therefore, electrospinning technology plays an important role in biomedical materials, filtration and protection, catalysis, energy, optoelectronics, food engineering, cosmetics and other fields. In addition, it also can be used as the preparation of V-based materials (V_2O_5 nanofibers[43], VN nanofibers[34]).

4 Vanadium oxide

4.1 VO_2 and its composite materials

4.1.1 VO_2 materials

In the past decades, VO_2(B), as a promising material for SCs, has attracted considerable interest than other polymorphs (VO_2(M), VO_2(R), and VO_2(A)) due to its special optical and electrical properties. However, the performance is limited because of its low rate capability and cycling stability, improved which have two categories: the first is that deliberate engineering of the materials structure. Zhang et al. developed a template-free method to prepare 3D VO_2(B) solid sphere, which were then converted to hollow spherical cages by hydrothermal and calcination treatment.[32] As electrode materials, the VO_2(B) hollow cages exhibited a specific capacitance of 1175 $mF\cdot cm^{-2}$ (336 $F\cdot g^{-1}$), apparently higher than that of the solid counterpart (951 $mF\cdot cm^{-2}$, 272 $F\cdot g^{-1}$) at 2 $mA\cdot cm^{-2}$. VO_2(B) hollow spheres also displayed enhanced stability, with 68% of the capacitance retained after 10 000 cycles, as compared to only 49% for the solid spheres. Using the same method to synthesize different morphologies of VO_2 is helpful to compare which morphology can increase the ion accessible area, reduce the ion transmission resistance, and improve the electrochemical performance. Ndiaye et al. prepared VO_2 of different morphologies (nanospheres and nanosheets) by a solvothermal method for a varied period of time, 2.5, 4, 6 and 12 h at the temperature of 200 °C.[44] VO_2(A) samples prepared at 2.5 h and 12 h revealed a yolk-shell structure with a less dense interior, whereas VO_2(B) samples prepared at longer hydrothermal times of 4 h and 6 h displayed a double-shell structure. In electrochemical tests in a three-electrode cell using 6 M KOH aqueous electrolyte, the resulting VO_2(B) nanosheets (6 h) possessed a higher specific discharge capacity than other samples, with a specific capacitance of 663 $F \cdot g^{-1}$ at the scan rate of 5 $mV \cdot s^{-1}$ and excellent cycling stability after 5000 cycles at the current density of 10 $A \cdot g^{-1}$. It shows that nanosheets have higher research value than nanospheres.

One of the unique properties of 2D nanosheets is the large specific surface area, which reduces the ion diffusion path and can effectively carry out the redox reaction. Rakhi et al. prepared VO_2 nanosheets (lateral dimensions in the range of 60 nm to 2 mm) and investigated their electrochemical behaviors in an organic gel electrolyte (1 M $LiClO_4$ in propylene carbonate (PPC)).[31] The ultrathin nanosheets were then used to fabricate SC electrodes by drop-casting the suspension of VO_2 nanosheets, conducting carbon and sodium carboxymethylcellulose (CMC) binder in water onto carbon paper, as shown in Fig. 2a, which exhibited a specific capacitance of about 405 $F \cdot g^{-1}$ at the current density of 1 $A \cdot g^{-1}$. The VO_2 based organic symmetric capacitor retained nearly 82% of its maximum capacitance (more than 95% of the initial capacitance) even after 6000 charge-discharge cycles. Ndiaye et al. developed a solvothermal method for large-scale production of poly-crystallinity, monoclinic VO_2 nanosheets. and used the materials to assemble an asymmetric SC (ASC) with the structure of carbonized iron-polyaniline (C-FP)/6 M KOH/VO_2, which exhibited 47 $mAh \cdot g^{-1}$ specific capacity and the specific energy of 30 $Wh \cdot kg^{-1}$ with an associated specific power of 713 $W \cdot kg^{-1}$ at a gravimetric current of 1 $A \cdot g^{-1}$ in a potential window of 1.6 V.[45] Meanwhile, the development of porous material is a trend in energy storage research. Nanosheets have high research value, at the same time, it is important to emphasize the diversity of morphology in the experimental process, so we should avoid studying only nanosheets.

Moreover, VO_2 thin film, a nanostructured semiconductor film, possesses novel physical and chemical properties and is suitable for various new applications. Basu et al. prepared monoclinic

VO_2 nanorods thin films through the CVD technique and coated VO_2 porous structure on carbon fiber (CF).[41] Field-emission scanning electron microscopic (FESEM) analysis showed a porous structure of the obtained thin films with an average pore diameter of approximately 200 nm (Fig. 2b and 2c). Electrochemically, the VO_2 arrays exhibited a specific capacitance of 20.7 $mF \cdot cm^{-2}$ at the current density of 0.3 $mA \cdot cm^{-2}$, a capacitance retention of 93.7% and coulombic efficiency of 98.2% for 5000 charge-discharge cycles. This suggests excellent rate capability, reversibility, and durability. Reddy et al. employed radio-frequency reactive magnetron sputtering to deposit thin films of monoclinic $VO_2(M)$ nanorods on indium tin oxide (ITO)-coated glass substrates at 300 °C and under various O_2 flow rates ranging from 2 to 6 sccm.[46] The film coated on ITO-coated glass substrates were treated at a substrate temperature of 300 °C and various O_2 flow rates ranging from 2 to 6 sccm. The thin films of $VO_2(M)$ nanorods prepared at the flow rate of 6 sccm revealed a specific capacitance of ~486 $mF \cdot cm^{-2}$ at the scan rate of 10 $mV \cdot s^{-1}$, and the specific capacitance remained virtually invariant at ~118 $mF \cdot cm^{-2}$ after 5000 cycles at the scan rate of 100 $mV \cdot s^{-1}$. In addition, the sample grown at the argon/oxygen flow ratio of 8:4 (V84, Fig. 2d) manifested a small resistance and excellent cycle stability (Fig. 2e). The electrochemical properties of the same morphology synthesized by different methods are completely different, which is mainly due to the different specific surface area and pore size. It mainly affects the ion transport path.

Different morphologies are synthesized by the same method or a morphology is synthesized by many methods, all of which mainly change the contact area and ion transmission channel between electrode materials and electrolyte to improve their electrochemical performance.

4.1.2 VO_2 hybrid materials

The second category to improve the electrochemical performance of VO_2 materials: formation of functional nanocomposites. Its mechanism mainly is that increased pseudocapacitance, increase ed the ion accessible area, and reduced the ion transmission resistance. Carbon materials (graphene, activated carbon, and carbon nanotubes/fibers) have been proved to be good electrode materials in SCs due to their excellent chemical stability, low cost, high power density, and long cycle life. And they are often used as a substrate for material in energy storage, such as VO_2/carbon onion hybrid materials [47], Fe_3O_4/carbon nanocomposites [48], RuO_2/rGO nanocomposites [49], r-GO/beta-$Cu_2V_2O_7$/TiO_2 nanorods composites [50]. When VO_2 and carbon materials are combined, it can make up for the defects of low conductivity and poor cycle stability of VO_2 and prevent its agglomeration, as well as improve its electrical conductivity. Zhang et al. prepared a VO_2(B) and carbon core-shell structure by a facile hydrothermal method. When tested as the electrodes for SCs, the VO_2(B)/C core-shell composites displayed a specific capacitance of 203 $F{\cdot}g^{-1}$ at the current density of 0.2 $A{\cdot}g^{-1}$ and an excellent energy density of 198.9 $Wh{\cdot}kg^{-1}$at a power density of 504.5 $W{\cdot}kg^{-1}$.[51] However, the cycling stability of VO_2(B)/C core-shell composites was poor in 1 M Na_2SO_4 aqueous solution.

Lightweight and high conductivity graphene materials are favorable to transport electron and ion and increase electrochemical performance. VO_2 NF@3DG growing VO_2 nanoflowers (NFs) on 3D graphene (3DG) networks with porous and stability were prepared by Wang et al.[52] The synthesis process of VO_2 NF@3DG hybrid is shown in Fig. 2h. The mass of VO_2 NFs on 3DG was around 0.91 $mg{\cdot}cm^{-2}$, and 3DG had a mass density of 8.22 $mg{\cdot}cm^{-2}$ after the hydrothermal reaction. VO_2 NF@3DG hybrid electrodes were found to exhibit a large specific capacitance of 466 $mF{\cdot}cm^{-2}$, and to retain capacitance retention of 63.5% after 3000 cycles in a 0.5 M K_2SO_4 aqueous electrolyte. Furthermore, VO_2 NF@3DG hybrid provided high energy density (279.6 $mWh{\cdot}m^{-2}$)

and high power density (60 000 mW·m^{-2}). Lv et al. utilized a simple method to prepare VO_2(B) nanobelts/rGO composites with a porous framework.[53] Combined the amorphous structure of rGO with VO_2 nanobelts is beneficial to improve the stability of VO_2 in electrochemical measurements. When tested as the electrode of all-solid-state symmetrical SCs (SSC), this composite was measured in a three-electrode system with a 0.5 M K_2SO_4 aqueous solution as the electrolyte. Electronic impedance spectra (EIS) showed that the resistance of VO_2/rGO was smaller compared with VO_2 nanobelts, which means that the VO_2/rGO composites had a highly interconnected porous structure and were easy to diffuse electrolyte ions and electrons. For the assembled all-solid-state SSC, the VO_2/rGO composites exhibited a good energy storage performance with 7152 W·kg^{-1} power density at the energy density of 3.13 Wh·kg^{-1}. After 10 000 cycles, 78% of the specific capacitance retention was retained at 10 A·g^{-1}.

More importantly, edge-oriented graphene foam (EOGF) is a continuous conductive frame for growing graphene on nickel foam by CVD method, which can minimize the ion diffusion length, increase the interface between electrolyte and electrode, and provide fast electron conduction path and strong mechanical support. Ren et al. synthesized VO_2 nanoparticles/EOGF composites to enhance the specific capacitance.[54] The electrochemical performance was investigated by cyclic voltammetry (CV) measurements, which showed a desirable quasi-rectangle profile, due to the high-rate capability arising from the synergistic effect of EOGF and VO_2 nanoparticles. The VO_2/EOGF electrode exhibited a capacitance of 119 mF·cm^{-2} at the scan rate of 2 mV·s^{-1}, about two orders of magnitude higher than that of the bare EOGF. At the high scan rate of 1000 mV·s^{-1}, a capacitance of 26 mF·cm^{-2} remained, and 70% of the capacitance was retained after 1500 cycles.

Hydrogen molybdenum bronze (HMB) is not only an n-type semiconductor with high electrical conductivity (10^3 to 10^5 $S \cdot m^{-1}$) but also a fast ionic conductor with an ionic conductivity of 0.001-0.01 $S \cdot m^{-1}$. Meanwhile, it also is a kind of shell material that can construct core-shell nanoarray electrodes based on metal oxides and enhance electrochemical performances. Xia et al. employed a hydrothermal and CVD method to synthesize VO_2-based core-shell composites (Fig. 2f), where HMB was first electrochemically deposited onto graphene foam (GF) surface, and then VO_2 nanoflakes were grown on the hybrid surface.[55] When applied as the electrode, the GF + VO_2/HMB composites expressed a better electrochemical performance with weaker polarization, higher specific capacitance, and better cycling life, than those of the GF + VO_2. After 500 cycles, a high reversible capacity was obtained, of 305 $mAh \cdot g^{-1}$ at 5 C (capacity retention of 91.8%), and 209 $mAh \cdot g^{-1}$ at 30 C (capacity retention of 95.4%). The GF + VO_2/HMB electrode showed a stable capacitance of 473 $F \cdot g^{-1}$ at 2 $A \cdot g^{-1}$ after 5000 cycles and 340 $F \cdot g^{-1}$ at 12 $A \cdot g^{-1}$ after 11 000 cycles, respectively.

By an organic-inorganic liquid interface, Fan et al. prepared 2D mesoporous VO_2 microarrays with the needle-like particles.[56] According to the difference of the aqueous phase, all VO_2-N (organic phase), VO_2-S (ultrapure water), and VO_2-F (hydrazine added in aqueous solution) can be synthesized, as shown in Fig. 2i, the VO_2-N microarray achieved a specific capacitance of 265 $F \cdot g^{-1}$ at 1 $A \cdot g^{-1}$, with a higher retention rate at high current density (182 $F \cdot g^{-1}$ at 10 $A \cdot g^{-1}$) than those of VO_2-S and VO_2-F (Fig. 2g). Pan et al. reported that hydrogen treatment of VO_2 powder resulted to an increase of the electrical conductivity, a specific discharge capacitance of 300 $F \cdot g^{-1}$ and specific energy density of 17 $Wh \cdot kg^{-1}$, along with excellent stability, which may be attributed to the formation of oxygen vacancies, slightly reduced vanadium valence state, and their synergetic effects.[57]

In the study process, there are two main strategies for improving the electrochemical performance of VO_2: 1) synthesis of novel structures; and 2) synthesis of VO_2 hybrid materials. But little research has been done on doping elements and changing the type of electrolyte. Doped elements in the material are a promising research trend.

4.2. V_2O_3 and its composites materials

V_2O_3, like other TMOs, is also an ideal energy storage material. For example, the conductivity of V_2O_3 is $10^3\ \Omega^{-1}\cdot cm^{-1}$,which is much higher than that of V_2O_5 ($10^{-3}\ \Omega^{-1}\cdot cm^{-1}$) and monoclinic VO_2 ($4\ \Omega^{-1}\cdot cm^{-1}$). But V_2O_3 nano-structured materials suffer from poor cycling stability and are liable to form soluble species in aqueous solution.[58, 59] It has been proved that the combination of nanostructured vanadium oxides and carbon can not only protect them from dissolution and structural deterioration but also improve the electron transfer efficiency and prevent the agglomeration of nanoparticles.[60] And V_2O_3/carbon composites can have different morphologies, such as fiber [61], core-shell structure [33, 62], nanofoam [63], nanoparticles [64], nanoflakes [65], and so on, depending on the synthesis method. Some V_2O_3/C nanocomposites with good electrochemistry performance can be prepared by hydrothermal reaction. For example, Hu et al. developed V_2O_3@C core-shell nanorods (Fig. 3a) with porous structures and large specific surface area ($246\ m^2\cdot g^{-1}$), and observed 228, 221, 207, 158, and 127 $F\cdot g^{-1}$ specific capacitances at current densities of 0.5, 1, 2, 5, and 10 $A\cdot g^{-1}$, respectively.[33] In addition, 86% of the capacitance was retained for a V_2O_3@C//C SC after 1000 cycles. V_2O_3@C had good cycling performance for SC applications. V_2O_3/C nanocomposites (the specific surface area: $106.8\ m^2\cdot g^{-1}$, Fig. 3d) were synthesized by Zheng et al. exhibited 458.6 $F\cdot g^{-1}$ high specific intercalation pseudocapacitance at 0.5 $A\cdot g^{-1}$, with a retention rate of 86% after 1000 cycles in aqueous electrolyte.[64] Notably, in some other studies, the electrochemical performance is unremarkable. Zheng et al. showed that the specific capacitances of the as-obtained V_2O_3@C core-shell composites (the specific surface area: 83.2 $m^2 \cdot g^{-1}$, Fig. 3c) were 146, 128, 83, and 58 $F \cdot g^{-1}$ in the 1st, 10th, 50th, and 100th cycle, respectively, and the corresponding retentions were 87.7, 56.8, and 39.7% of the initial discharge capacity.[62] The composites prepared by the same method have different morphologies (different specific surface areas) due to their different reactants and reaction conditions. At the same time, different electrolytes, test methods, environments, and personnel make their electrochemical performances completely different.

Zhang et al. produced a V_2O_3 nanofoam@activated carbon composite (the specific surface area: 42.6 $m^2 \cdot g^{-1}$) by solvothermal method, which exhibited a specific capacitance of 185 $F \cdot g^{-1}$ at 0.05 $A \cdot g^{-1}$.[63] The capacitance was found to decrease rapidly in the first 30 cycles, and only 49% of the initial value was maintained after 100 cycles. In addition, a self-supported film electrode (V_2O_3/N-rGO) was fabricated where nitrogen-doped rGO was intertwined with V_2O_3 nanoflakes, as shown in Fig. 3f, and it was found that it manifested an area capacitance of 216 $mF \cdot cm^{-2}$ at a current density of 1 $mA \cdot cm^{-2}$ and had excellent cycling stability with 81% of the initial capacitance retention after 10 000 cycles.[65] Different methods, reactants will prepare different nano-materials to obtain different electrochemical properties.

Nowadays, the study of V_2O_3 and composite in SCs is superficial, the nanocomposites, such as the novel V_2O_3 structure, V_2O_3/conducting polymers, V_2O_3/transition metal compounds, the doped element, should be explored in the future, which deserves many researchers to spend more time and energy.

4.3 V_2O_5 and its composites

4.3.1 V_2O_5 materials

There are many factors affecting the electrochemical properties of materials, such as morphology, electrolytes, surfactant and so on. The excellent electrochemical performance requires active electrode materials, such as TMOs, carbon-based materials, and conducting polymers, which will help to improve the energy storage of equipment. V_2O_5, TMOs, is another promising candidate as electrode materials for SCs, with a high theoretical specific capacity (2120 $F{\cdot}g^{-1}$), economic feasibility, and natural abundance. However, V_2O_5 has a low surface area, poor electrical conductivity, and structural stability, and its nanostructures typically exhibit only a relatively low energy density. Therefore, to enhance electrochemical properties, structural engineering, unique shapes, and suitable electrolytes are effective strategies.

The porosity of nanomaterials is helpful to the diffusion of ions and electrons and prolongs the material life in energy storage systems. It was considered as excellent electrode materials in terms of achieving high specific capacitance. Saravanakumar et al. developed a simple capping-agent-assisted precipitation technique to synthesize V_2O_5 nanoporous network.[66] When utilized as electrode material in a three-electrode system, the V_2O_5 nanoporous network achieved a higher specific capacitance of 316 $F{\cdot}g^{-1}$ compared to as-prepared samples with annealing. When annealing temperature increased to 300 °C, the specific capacitance decreased accordingly to 135 $F{\cdot}g^{-1}$ due to shrinking pores of the sample. In addition, this material exhibited comparatively excellent capacity retention. Hollow V_2O_5 spheres, as a class of porous material, were fabricated by a solvothermal process from Yang et al..[67] When used as an electrode for SCs in a solution of 5 M $LiNO_3$, these materials showed a tremendous pseudocapacitance effect with a high capacitance of

479 $F \cdot g^{-1}$ at 5 $mV \cdot s^{-1}$. When polypyrrole (PPy) was deposited onto the surface of the hollow V_2O_5 spheres, the capacitance was increased to 566 $F \cdot g^{-1}$ at 5 $mV \cdot s^{-1}$ with a capacity retention rate of 70% after 100 cycles. As mentioned above, the materials with the porous structure remain a high specific area and more active site, which facilitated ion transport and improved electrochemical performance.

Surfactants can change the morphology of materials to enhance the specific surface area and electrochemical properties. Yang et al. synthesized $V_2O_5 \cdot H_2O$ by the hydrothermal method in several surfactants, such as Polyethylene glycol 6000 (PEG-6000), sodium dodecylbenzene sulfonate (SDBS), and Pluronic P-123 (P123).[68] As an electrode, $V_2O_5 \cdot H_2O$ nanowire (NW) in the presence of PEG-6000 exhibited the highest capacitance of 349 $F \cdot g^{-1}$ at a scan rate of 5 $mV \cdot s^{-1}$ than those surfactants of SDBS (flower-like stacks of flakes) and P123 (perforated networks with curly bundled NWs), which may be due to electronic migration along the homogeneous and straight NWs would be smooth. However, the symmetric P123 electrode showed a specific capacitance of 127 $F \cdot g^{-1}$ in comparison with PEG-6000 (45 $F \cdot g^{-1}$) after 200 cycles, which may be ascribed to the morphology. Therefore, the morphology has a positive effect on the specific capacitance, which does not mean that it also has a good impression on its cycle performance.

In addition, the variability of vanadium oxide in aqueous solutions is ascribed to material dissolution and weak structural stability during electrochemical measurement.[59, 69] Deng et al. synthesized 3D network V_2O_5 by electrodeposition and tested its electrochemical performance in gel electrolytes.[70] The synthetic route and the structure of the porous V_2O_5/conductive printing paper (U-paper) and 3D network V_2O_5/Pt/U-paper are depicted in Fig. 3b. Fig. 3e shows the 3D network V_2O_5/Pt/U-paper with a high surface area of ~122 $m^2 \cdot g^{-1}$ and pore-size distribution containing 21.3% (micropores, <2 nm), 70.1% (mesopores, 2-50 nm), and 8.6% (macropores, >50 nm). When inorganic electrolyte (1 M KCl solution) was used, porous V_2O_5/U-paper, 3D network V_2O_5/Pt/U-paper, and V_2O_5/carbon cloth (CC) as symmetric pseudocapacitor (SPC) electrodes were carried out, and 3D network V_2O_5/Pt/U-paper electrode (the operating voltage range from 0.0 to 1.6 V) showed higher capacitance retention (72% after 5000 cycles). It means that the nanostructures from the 3D network V_2O_5/Pt/U-paper based SPC are uniform and the novel 3D network V_2O_5 and Pt layer can reduce the dissolution of V_2O_5 and improve structural stability. Interestingly, with urea-$LiClO_4$-polyvinylalcohol (ULP) gel electrolytes, wearable SPCs (WSPCs) based on the porous V_2O_5, 3D network V_2O_5 (the operating voltage range from 1.0 to 4.0 V), and V_2O_5/CC presented a great level of retention of ~80.1, 91.1, and 77.6% after 5000 cycles, respectively. Electrospinning method, considered as a simple, one-step, cost-effective method, control the structure, and morphology and diameter (~ten nanometers to several micrometers) of the nanofiber. Wee et al. fabricated V_2O_5 nanofibers through this method and measured it in the difference of electrolytes (the different pH aqueous electrolyte and an organic electrolyte).[43] The specific capacitance for this material annealed at 400 °C yielded 190 $F \cdot g^{-1}$ in aqueous electrolyte (2 M KCl, the operating voltage window: 0.0-0.9 V) and 250 $F \cdot g^{-1}$ in organic electrolyte (1 M $LiClO_4$ in PPC, the operating voltage window: 0.0-3.0 V). As mentioned above, the gel electrolytes in V_2O_5 WSPCs not only enhance mechanical stability but also minimize the V_2O_5 chemical dissolution. And organic electrolytes has excellent ionic transfer rates, and contribute to higher operating voltages and excellent cycling stability than inorganic electrolytes, which proves the solubility and structural instability of the material in aqueous solution.

Thin films are generally synthesized through vacuum evaporation, sputter deposition, pulsed laser deposition, CVD, thermal oxidation, and sol-gel processes. Pandit et al. developed a simple and inexpensive chemical bath deposition (CBD) to grow V_2O_5 on a pliable stainless steel substrate and used the resulting nanocomposites as an electrode for SCs. And the electrode exhibited a high specific capacitance of 735 $F \cdot g^{-1}$ at 1 $mV \cdot s^{-1}$ in 2 M $LiClO_4$ electrolyte and good capacitors retention of 71% after 1000 cycles.[71] Fig. 3g is a schematic representation of the fabricated complete flexible solid-state SC device. It consists of polyvinylalcohol (PVA)-$LiClO_4$ gel electrolyte as a separator and the two symmetric V_2O_5 electrodes. The flexibility test (Fig. 3h) was performed by CV measurements at 20 $mV \cdot s^{-1}$ at different bending angles from 0° to 175°. The device showed 91% capacitance retention even at 175° bending angles, demonstrating exceptional flexibility.

4.3.2 V_2O_5/carbon based materials

Carbon-based SCs in acid media can only provide a low operating voltage between 1.0 and 3.0 V, which limits its energy and power density.[72, 73] Generally, carbon-based materials will select alkaline electrolytes during electrochemical behavior. The hydrothermal method is one of the most promising methods and can provide high vapor pressure and suitable temperature in closed vessels, thus resulting in optimal structures of as-fabricated electrodes for high-performance SCs. The rGO/V_2O_5 compounds were synthesized via this method and subsequent annealing process by Liu et al..[74] Fig. 4a shows holey-graphene oxide (HGO) and rGO/V_2O_5 synthesis diagram. When rGO/V_2O_5 composite was used as an electrode, the CV curve had a working potential of -0.8 V to 0.8 V in 1 M $LiClO_4$/PPC electrolyte. For the rGO/V_2O_5 composites prepared at 300 °C (RGV-300), the specific capacitance was 386, 338, 294, 241, and 197 $F \cdot g^{-1}$ at 0.1, 0.2, 0.5, 1, and 2 $A \cdot g^{-1}$, respectively. The asymmetric system composed of RGV-300 and rGO as the cathode and anode respectively was observed to excellent performance, with an almost 82.2% specific capacitance retention after 10 000 cycles. Choudhury et al. then developed a simple, hydrothermal method and in-situ chemical process to prepare V_2O_5 nanofiber/exfoliated graphene nanohybrid with the mass ratio of 1:0.25 and 1:0.5 (the as-prepared nanohybrids were denoted as $V_1G_{0.25}$ and $V_1G_{0.5}$, respectively).[75] When the CV test was carried out in the voltage range of -0.4 to 1.2 V at the scan rate of 25 $mV{\cdot}s^{-1}$, $V_1G_{0.5}$ showed a larger area than $V_1G_{0.25}$ and V_2O_5 nanofiber. It can be clearly seen that $V_1G_{0.5}$ suggested a high charge-storage capacity. Besides, $V_1G_{0.5}$ nanohybrid in acetonitrile electrolyte of 1 M LiTFSi exhibited the best capacitive among the series, with a specific capacitance of 218 $F{\cdot}g^{-1}$ at 1 $A{\cdot}g^{-1}$, energy density of 22 $Wh{\cdot}kg^{-1}$, and power density of 3594 $W{\cdot}kg^{-1}$. In addition, it is a challenge to realize the strong interaction between modified materials and aerogel graphene. The rGO nanosheets/V_2O_5 nanobelts hybrid prepared by hydrothermal process has been reported by Yao et al..[76] They successfully obtained hybrid nanobelts and demonstrated its porous structure features (Fig. 4b). And resultant rGO/V_2O_5 hybrid aerogel electrode remained a high specific capacitance of 310 $F{\cdot}g^{-1}$ at 1 $A{\cdot}g^{-1}$ scan rates. Moreover, a SSC based on rGO/V_2O_5 hybrid aerogel was assembled, which recorded high gravimetric capacitance of 225.6 $F{\cdot}g^{-1}$ (0.5 $A{\cdot}g^{-1}$), a high energy density of 31.3 $Wh{\cdot}kg^{-1}$ (249.7 $W{\cdot}kg^{-1}$) and excellent long-term cycle stability (90.2% after 5000 cycles). The hydrothermal method, a simple, effective method, can control a suitable structure of material in different experiment environment. And hybrid aerogel can to be a hot research topic in the next few years.

Different morphologies (nanosheets[77, 78], nanonords[38] and nanospheres[79]) provide larger surface area, shorten ion/electron the diffusion distance, further offer more active site and alleviates the concentration polarization of electrode materials, resulting in different electrochemical performance. Nagaraju et al. reported 2D heterostructures of V_2O_5/rGO nanosheets, which was obtained by 2D heterostructures of V_2O_5 nanosheets growing on rGO flakes.[77] This material had relatively high specific (653 $F\cdot g^{-1}$ at 1 $A\cdot g^{-1}$) and cyclic stability (94% after 3000 cycles). Moreover, Yilmaz et al. successfully synthesized the cross-linking of a V_2O_5-graphene hybrid with the surface area up to 83.4 $m^2\cdot g^{-1}$ using vanadium-thiourea redox system (Fig. 4c).[78] After the initial 5000 cycles, it maintained 85% of the initial capacitance, while only 5% capacitance was lost between 5000 and 10 000 cycles, revealing good long-term cycling stability. Moreover, Kiruthiga et al. embedded V_2O_5 nanorods into rGO as a high energy density-battery type faradaic anode, and used activated porous carbon as a high power density-SC type non-faradaic cathode, which delivered a specific capacitance of 289 and 224 $F\cdot g^{-1}$ at 0.01 $A\cdot g^{-1}$ respectively.[38] The sodium-ion capacitor assembled with V_2O_5@rGO anode and activated porous carbon cathode exhibited an energy density of 65 $Wh\cdot kg^{-1}$, a power density of 72 $W\cdot kg^{-1}$ at 0.03 $A\cdot g^{-1}$ and a capacity retention of 74% after 1000 cycles at the current density of 0.06 $A\cdot g^{-1}$. Meanwhile, Ghaly et al. summarized the previous results and successfully synthesized 3DG-wrapped V_2O_5 nanospheres as the positive electrode and Fe_3O_4@3DG electrode as the negative electrode, which exhibited a maximum energy density of 54.9$Wh\cdot kg^{-1}$ with a power density of 898 $W\cdot kg^{-1}$ with an extended voltage of 1.8 V in 1.0 M Na_2SO_4 aqueous electrolyte.[79] Furthermore, the ASC device demonstrated excellent cycling stability with 89.6% capacitance retention over 10 000 cycles.

Fabricating freestanding graphene SC electrode can reduce equivalent series resistance (ESR) and allow higher load density. To obtain lower ESR, the ionic resistance of the electrolyte, the intrinsic resistance of the active material, and the contact resistance between active material and electrode in the SC system were adjusted by Too et al..[80] Experimentally, V_2O_5-rGO free-standing electrode was synthesized through the modified Hummers method, and a high areal capacitance (511.7 mF·cm^{-2}) was achieved. Fig. 4d shows the CV of the asymmetric device at flat and bent state at 25 mV·s^{-1}, which demonstrates the performance of its electrodes. More importantly, the assembling asymmetric flexible device based on rGO/V_2O_5-rGO, which was composed of about 20 mg of active mass, exhibited a low ESR of 3.36 Ω with excellent cycling stability.

As mentioned above, V_2O_5 as electrode materials for SCs has potential application prospects. And V_2O_5/carbon composite materials with many advantages were recently discussed. The carbon-coated flower V_2O_5 as electrode materials in SCs have been reported by Balasubramanian et al..[81] The morphology of carbon-coated V_2O_5 was examined by FESEM, as shown in Fig. 4e, which displayed flowery architecture with a well-resolved urchin-like structure. Moreover, the selected area diffraction pattern (SAED, Fig. 4f) measurements suggested the amorphous nature of the carbon layer. The specific capacitance of this composite was 417 F·g^{-1} at a current density of 0.5 A·g^{-1}. However, the capacitance of the material gradually increased due to the activation process and attained the maximum capacitance (100%) around 2000 cycles and decreased to 92.3% after 2250 cycles. Zhu et al. developed a simple “liquid phase impregnation template” strategy to fabricate hierarchically porous V_2O_5/C (HPVC) nanocomposites using commercial V_2O_5 and phenol-formaldehyde (PF) resol as precursors and polystyrene opal microspheres as template.[82] The preparation route of the HPVC is seen in Fig. 5a. Hierarchical porous HPVC nanocomposites with high surface area (645 m^2·g^{-1}) exhibited the high specific capacitance up to 492.1 F·g^{-1} at a scan rate of 5 mV·s^{-1} in 2 M $LiNO_3$ electrolyte solution. Besides, the assembled symmetric electrode based on HPVC reached an energy density as high as 87.6 Wh·kg^{-1} at a power density of 210 W·kg^{-1}, as well as excellent cycling stability (93% after 10 000 cycles). Tian et al. fabricated nanostructured V_2O_5 impregnated mesoporous carbon microspheres (MCM/V_2O_5) by a facile wet impregnation method (Fig. 5b), which entailed three steps, spray drying, carbonization, and wet-impregnation process.[83] The electrochemical performance of capacitors was evaluated by CV curves using a symmetrical two-electrode system in Na-ion, Mg-ion, and Al-ion capacitors. Compared with Na-ion, Mg-ion capacitors, the Al-ion capacitor achieved more effective reactions and higher capacitance enhancement, with the specific capacitance of 290 $F \cdot g^{-1}$ at 0.5 $A \cdot g^{-1}$, a high energy density up to 18.0 $Wh \cdot kg^{-1}$ at 147 $W \cdot kg^{-1}$ and great cycling stability up to 88% capacitance retention after 10 000 cycles.

Carbon nanotubes (CNTs) have hierarchically porous structures to enhance the ion transport channel. Chen et al. synthesized CNT/V_2O_5 nanocomposites through a one-pot hydrothermal process. For pseudocapacitive materials composed of CNTs and V_2O_5 NW interpenetrating networks, it gave a capacity of 86 $C \cdot g^{-1}$ between 1.8 and 4.0 V in 1 M $LiClO_4$ in PPC solution, an energy density value of 40 $Wh \cdot kg^{-1}$ with a power density of 210 $W \cdot kg^{-1}$ at a current density of 0.5 $mA \cdot cm^{-3}$.[84] Using the electrospinning method, Kim et al. prepared the V_2O_5/carbon nanofiber composites (CNFCs) at the different ratios of V_2O_5 concentration (5%, 10%, 20%), which were identified as V_2O_5-5, V_2O_5-10, and V_2O_5-20. Of those, V_2O_5-20 obtained the highest specific capacitance.[85] MWCNTs are commonly used electrode materials and composite materials for enhancing porous structure, conductivity, and surface area. V_2O_5/MWCNT core/shell hybrid aerogels at different MWCNT contents using the sol-gel method were reported by Wu et al..[39] Fig. 5c shows the mixed growth and self-assembly methodology for controlled synthesis of 3D V_2O_5/MWCNT core/shell hybrid aerogels. There are the charge transfer resistance (R_{ct}) values of as-prepared aerogels and other samples in electrochemical impedance spectroscopy measurements

(Fig. 5d). The hybrid aerogel exhibited the maximum specific capacitance (625 F·g^{-1}) and outstanding cycle performance (>20 000 cycles) because of its high specific surface area, favorable electrical conductivity, and unique 3D and core/shell structures. Shakir et al. reported a composite consisting of ultrathin V_2O_5 anchored on MWCNTs and graphene by the layer-by-layer assembly (LBL) technique, in which a graphene layer was alternatively inserted between the MWCNT films coated with ultrathin (3 nm) V_2O_5 (Fig. 5e).[86] Such a structure mitigated the issues of low surface area and poor electrical conductivities of nanostructured V_2O_5 for electrochemical SCs. When measuring LBL assembled electrodes composed of MWCNTs coated with a 3 nm thick V_2O_5 layer and graphene in three electrodes system using KCl aqueous electrolyte, the specific capacitance achieved 2590 F·g^{-1} at a scan rate of 1 mV·s^{-1} compared with the 20 nm thick V_2O_5 layer on MWCNTs (510 F·g^{-1}). In addition, the energy density reached 96 Wh·kg^{-1} at a power density of 800 W·kg^{-1} and reduced to 28 Wh·kg^{-1} at a power density of 9 kW·kg^{-1} when SC electrode assembled by LBL was tested in an organic electrolyte ($LiClO_4$). Kim et al. prepared MWNT/V_2O_5 NW composites by sol-gel method for the assembly of a flexible micro-SC (MSC) with a solid electrolyte.[87] The MSC using MWNT/V_2O_5 NW composites of hybrid electrodes with 10 vol % of V_2O_5 NWs exhibited excellent electrochemical performance with a high volume capacitance of 80 F·cm^{-3} at a scan rate of 10 mV·s^{-1} in a PVA-LiCl electrolyte and good cycle performance with 82% of the capacitance after 10 000 cycles at a current density of 11.6 A·cm^{-3}. Fig. 5f displays the rate of voltage drop (dV/dt) with UV was initially accelerated (30.8 mV·s^{-1} vs. 9.8 mV·s^{-1}) but later became almost the same as that without UV (3 mV·s^{-1} vs. 2.8 mV·s^{-1}). That is, the photosensitivity estimated from the ratio of dV/dt with and without UV was ca. 5 in the initial 25 s, and then became saturated to 1. These results showed the potential application of MSCs as a power supply for the operation of nano-devices including NW sensors. MWCNTs are a good supporting material, after combined with V_2O_5, presented a super specific capacitance.

To overcome the extreme hydrophobicity of carbonaceous materials and strengthen the connection between the carbon host and V_2O_5, it is necessary to introduce additional heteroatoms, especially nitrogen atoms, into the carbon framework. Sun et al. reported self-assembled 3D N-carbon nanofibers (CNFs)/V_2O_5 aerogels forming the stable and homogeneous core/shell morphology (Fig. 6a and 6b).[88] In addition, the specific capacitance of N-CNFs/V_2O_5 aerogels was always higher than that of CNFs/V_2O_5 aerogels and CNFs@V_2O_5 aerogels. It is distinctly observed from Fig. 6f that the semicircle (R_{ct}) of N-CNFs/V_2O_5 aerogels (1.04 Ω) was much lower than that of CNFs/V_2O_5 aerogels (2.72 Ω). After 12 000 cycles, the specific capacitance was 575.6 $F\cdot g^{-1}$ and 97% of the initial capacitance was retained (Fig. 6g). Sun et al. also synthesized hierarchical nanocomposites of V_2O_5 NWs arrays (NWAs) on a 3D N-doped graphene aerogel (N-GA) with different reaction intervals.[89] The SEM of this material with the porous structure is illustrated in Fig. 6c. When used as the electrode materials for SCs in 8 M LiCl aqueous solution, the specific capacitance of the N-GA@V_2O_5 NWAs was calculated to be 710 $F\cdot g^{-1}$, which was much higher than that of the GA@V_2O_5 (320 $F\cdot g^{-1}$) at a current density of 0.5 $A\cdot g^{-1}$. Furthermore, the N-GA@V_2O_5 NWAs exhibited outstanding rate performance and good cycling behavior of 95% retention of specific capacitance after 20 000 cycles. Nitrogen atoms were introduced into carbon-based materials, and its hydrophobicity was greatly limited, which makes it possible to improve the specific capacitance and cycle performance of composite materials.

4.3.3 V_2O_5/conducting polymers

The combination of V_2O_5 and carbon materials is an effective method to improve the performance of SCs, but its structure is unstable, that is, it cannot prevent V from dissolving, resulting in the loss of active sites. To mitigate this issue, conducting polymers, such as poly (3, 4-ethylenedioxythiophene) (PEDOT), PPy, and polyaniline (PANI) have been integrated into V_2O_5 to enhance the electrical conductivity, storage capacity, and chemical stability. Qian et al. successfully prepared interconnected 3D V_2O_5/PPy network nanostructures by in situ polymerization process, which showed a high specific capacitance of 448 $F·g^{-1}$ as compared to stacked V_2O_5.[90] When an all-solid-state SSC device was assembled, the V_2O_5/PPy core/shell 3D network maintained good cyclic stability (capacitance retention of 81% after 1000 cycles) and high energy density (14.2 $Wh·kg^{-1}$) at a power density of 250 $W·kg^{-1}$. Wang et al. synthesized V_2O_5@PPy core-shell NWs by a facile in situ interfacial synthesis approach (Fig. 6e).[91] As the binder- and additive-free SC electrodes, it achieved a specific capacitance of 334 $F·g^{-1}$, along with superior rate capability. Moreover, with the whole lattice unchanged, the electronic structure was adjusted, so that oxygen vacancies appear in the V_2O_5 conductive polymer, thereby effectively improving the electrochemical performance. Bi et al. developed V_2O_5-conductive polymer nanocables with oxygen vacancies.[92]. The schematic illustration of the enhanced ionic transfer kinetics around oxygen vacancies (ö) by the formation of a local electric field (E) is illustrated in Fig. 6d. When tested as an electrode for SCs, the specific capacitance of Vö-V_2O_5/PEDOT (614 $F·g^{-1}$) was higher than that of Vö-V_2O_5/PANI (523 $F·g^{-1}$) and Vö-V_2O_5/PPy (437 $F·g^{-1}$). It is observed from Fig. 6h that Vö-V_2O_5/PEDOT, Vö-V_2O_5/PANI and Vö -V_2O_5/PPy manifested 111%, 108%, and 101% capacitance retention after 15 000 cycles, respectively.

4.3.4 V_2O_5/transition metal composites

Because of transition metal compounds have the advantages of multivalent valence, various crystal structure, and morphologies, they typically have obtained high theoretical specific capacitance (such as V_2O_5 (2020 $F{\cdot}g^{-1}$)[93], RuO_2 (1358 $F{\cdot}g^{-1}$)[94], MnO_2 (1370 $F{\cdot}g^{-1}$)[95], TiO_2 (1260 $F{\cdot}g^{-1}$)[96] and MnS_2 (1504 $F{\cdot}g^{-1}$)[97]). The combination of transition metal compounds and V_2O_5 can further improve the electrochemical properties. Xu et al. grew V_2O_5 nanobelts/TiO_2 nanoflakes composites directly on nickel foam via a two-step hydrothermal process.[98] Fig. 7e shows that TiO_2 nanoflakes were intersected perpendicularly to one another in the hierarchical VNBs/TNFs heterojunction composite, which exhibited high porosity, a high specific surface area, and capacitive performance. Notably, the morphology of V_2O_5 nanobelt/TiO_2 nanoflake composites could be readily manipulated from nanoparticles, nanoflakes to nanoflake spheres, thick nanoflakes in different times range from 1 to 8 h. When used as an electrode of SCs in 1 M $LiNO_3$ electrolyte, the crystal structure and charge-discharge process are shown in Fig. 7a. The composites expressed a high specific capacitance (587 $F{\cdot}g^{-1}$ at 0.5 $A{\cdot}g^{-1}$) and good cyclic stability (97% after 5000 cycles). Yang et al. also reported V_2O_5-TiO_2 nanotube by self-organizing anodization of Ti-V alloys, thermally annealed at 300 °C, and then used as the electrodes in SCs.[99] The specific capacitance of the nanotubes illustrated 220 $F{\cdot}g^{-1}$ with an energy density of 19.56 $Wh{\cdot}kg^{-1}$ and was found to be very stable in repeated cycles. The V_2O_5-doped α-Fe_2O_3 composites were prepared through a simple one-step electrospinning technique followed by calcination treatment by Nie et al..[100] The weight ratio 1.0% of the composites with mesoporous structures maintained a capacitance of 150 $F{\cdot}g^{-1}$ over 200 cycles at 6 $A{\cdot}g^{-1}$. Wang et al. fabricated V_2O_5/Ni_3S_2 nanoflakes by a simple one-step hydrothermal method.[101] V_2O_5 is an n-type semiconductor, while Ni_2S_3 is used as a p-type semiconductor, Ni_3S_2/V_2O_5 can constitute a p-n heterojunction, leading to an improved energy storage performance with charge-transfer kinetics and high-rate capability. Fig. 7c shows the charge transport in the V_2O_5/Ni_3S_2 nanoflake nanostructures. As the SC electrode, the nanoflakes displayed the specific capacitances of 3060, 2676, 2089.6, and 1520 $F{\cdot}g^{-1}$ at scan rates of 1, 2, 5, and 10 mV·s^{-1}, respectively, and maintained 85% of capacitance after 2500 cycles. Meanwhile, Zhong et al. reported hierarchical V_2O_5@Ni_3S_2 hybrid nanoarray supported on nickel foam synthesized by a hydrothermal method.[102] The synthesis of hierarchical V_2O_5@Ni_3S_2 hybrid nanoarray was seen in Fig. 7d. When the V_2O_5@Ni_3S_2 electrode conducted out by galvanostatic charge-discharge (GCD) at various current densities, its calculated capacitances are close to each other, indicating good rate capability. After 1000 cycles, V_2O_5@Ni_3S_2 retained 60% of its initial capacitance in comparison to 85% for Ni_3S_2. But the capacitance was higher for the former than that of the latter. Manikandan et al. employed a simple co-precipitation technique to prepare polycrystalline $V_2O_5/Na_{0.33}V_2O_5$ with different molar ratios of $VOSO_4 \cdot xH_2O$ and NaOH: V1 (1:2), V2 (1:1) and V3 (1:0.1).[103] The capacitive behavior (phase angle) of V1(-60°), V2(-55°), and V3(-62°) was lower than that of an ideal capacitor (-90°) at low frequency region, and at high frequency region, the electrode shows a broad peak, representing the decrease in diffusion resistance of ions into the electrode, further indicating V2 had a small resistance, as shown in Fig. 7i. However, the V2 electrode showed comparatively low cyclic stability (62%) than V1 (96%) and V3 (85%) electrodes in GCD cycles.

Nowadays, the synthesis of two materials cannot meet people's needs. People try their best to develop high-performance materials by compounding materials with good properties. Jayalakshmi introduced SnO_2-V_2O_5 composites by a hydrothermal method in an autoclave, while SnO_2-V_2O_5-CNT composites were prepared by the simple mixture of carbon nano-tubes and the oxides. SnO_2-V_2O_5-CNT composites exhibited the highest specific capacitance compared with CNT, V_2O_5, CNT-V_2O_5 at the scan rates of 100 mV·s^{-1} whether used as anodic or cathodic materials.[104] The presence of SnO_2 improved the electronic and redox properties of V_2O_5 in composites. More importantly, there were synergistic interactions among the three structural components of SnO_2,

V_2O_5, and CNT. Guo et al. synthesized V_2O_5/PEDOT/MnO_2 nanosheets, consisting of layer V_2O_5, conducting polymer PEDOT, and layer MnO_2. [105]. The fabrication of the composites is presented in Fig. 7b. In an ASCs (Fig. 7h) with V_2O_5/PEDOT/MnO_2 nanosheets as the cathode and activated carbon as the anode in 1 M Na_2SO_4 aqueous electrolyte, its capacitance retention of 93.5% was observed with the energy density of 39.2 $Wh{\cdot}kg^{-1}$. When V_2O_5 combined with metal oxides and carbon materials or conducting polymer, its electrochemical performance has been greatly improved.

At present, the nanocomposite, combined V_2O_5 with various materials (carbon material, conductive polymer, metal compounds), has been greatly improved in many aspects, such as material structure, flexibility, and electrochemical performance. And the V_2O_5 system is relatively complete compared to other vanadium oxides (VO_2 and V_2O_3). However, practical application is the subject of our research, and higher performance products are our pursuit.

5 VN and its composites material

5.1 VN materials

Transition metal nitrite based SC electrodes has attained considerable attention as high capacity energy storage material, wide potential range (1.2 V), and low cost compared to traditional TMOs. The impressive electrochemical performance of VN is attributed to the combination of its high electronic conductivity and the redox reactions provided by a few layers of vanadium oxides or oxynitrides on the surface. The former is responsible for fast electronic transmission and the latter for high pseudocapacitance. Glushenkov et al. prepared porous nanocrystalline VN by temperature-programmed NH_3 reduction of V_2O_5.[106] An SEM image of the initial V_2O_5 nanorods is presented in Fig. 7f. Fig. 7g shows porous VN nanorods with a pore size range of 15 to 110 nm. VN had an acceptable rate capability in three aqueous electrolytes (1 M H_2SO_4, 1 M KOH, and 3 M NaCl solutions). The highest capacitance was 186 $F \cdot g^{-1}$ at the current density of 1 $A \cdot g^{-1}$ in 1 M KOH electrolyte. Moreover, Djire et al. fabricated nanostructured VN using the same method.[107] The capacitance retention of the VN material in 0.1 M KOH/H_2O was over 93% after 2700 cycles, indicating good electrochemical stability. VN, as the anode material in SCs, undergoes irreversible electrochemical oxidation reaction to generate vanadium oxide (VO_x) in aqueous solution. Lu et al. proposed a strategy to improve the stability of NWs by using LiCl/PVA gel electrolyte for asymmetric quasi-solid-state SCs with VN NW anode and VO_x NW cathode.[34] VN NW, uniformly interlaced VO_x NWs after nitridation, exhibits a high specific area of VN NW. Fig. 7j presents essentially the same shape as the scan rate increases from 10 to 100 $mV \cdot s^{-1}$, indicating good capacitive behavior of VN NWs. It is clear that the LiCl/PVA gel electrolyte prominently improves the stability of the VN electrode compared with the 5 M LiCl aqueous electrolyte, with extremely high capacitance retention of 95.3% after 10 000 cycles, as seen in Fig. 7k. Zhang et al. synthesized polyporous VN nanofibers by a facile electrospinning method and calcination at 550 °C (specific capacitance 110.8 $F \cdot g^{-1}$) for symmetric all-solid-state SCs, which had higher cycling stability and exhibited a higher specific capacitance than these of the VN nanofibers synthesized at 600 °C (specific capacitance 71.5 $F \cdot g^{-1}$) and 650 °C (specific capacitance 76.0 $F \cdot g^{-1}$).[108]

5.2 VN/carbon-based material

The small specific surface area limits electroactive sites for capacitive storage, resulting in compromised capacitance. Ran et al. successfully developed a novel method combining surface-initiated electrochemical mediated atom transfer radical polymerization technology (ATRP) and heat treatment process to synthesis a negative electrode material of nano VN/interconnected porous carbon (Nano-VN/IPC) with 483 $m^2 \cdot g^{-1}$ specific surface area.[109] The Nano-VN/IPC electrode remained a high specific capacitance of 284 $F \cdot g^{-1}$ at 0.5 $A \cdot g^{-1}$, an ultrahigh energy density of 35.6 $Wh \cdot kg^{-1}$ and a power density of 362.5 $W \cdot kg^{-1}$ in 2 M KOH. The hybrid composite of IPC@VN consisting of VN nanoparticles (VNNPs) on the surface of porous carbon was reported by Zhang et al..[110] The m-IPC@VN was obtained by thermo-treatment with a temperature of 600 °C for 90 min at a constant heating rate of 5 $°C \cdot min^{-1}$ in an ammonia atmosphere. Fig. 8c depicts the process of vanadate ion adsorption and electrode preparation. An ASC was assembled with $Ni(OH)_2$ and m-VN/IPC electrodes as the positive and negative electrodes, respectively, and exhibited a high specific capacitance of 129 $F \cdot g^{-1}$ at the current density of 1 $A \cdot g^{-1}$. Li et al. synthesized spatially confined the composite of VN nanodots intercalated carbon nanosheets (VNNDs/CNSs).[111] The preparation procedure is shown in Fig. 8a. The VNNDs/CNSs electrode showed an ultrahigh volumetric capacitance of 1203.6 $F \cdot cm^{-3}$ at 1.1 $A \cdot cm^{-3}$ and rate capability of 703.1 $F \cdot cm^{-3}$ at 210 $A \cdot cm^{-3}$ in comparison to those of CNSs and mesoporous VN nanosheets (VNNSs) materials, as well as extraordinary cycling stability with 90% capacitance retention after 10 000 cycles.

Recently, it has been found that different preparation methods can affect the surface area, crystallite size, surface oxidation states, and oxygen content of the material, which directly determines its capacitance. Ouldhamadouche et al. used electron cyclotron resonance (ECR)-plasma enhanced CVD (PECVD) process to synthesize the composite of nano-tree-like VN and CNTs.[112] It can be observed from Fig. 8d that the capacitance increased with VN deposit thickness, and only 15% capacity decayed after 15 000 and 20 000 consecution cycles at a scan rate of 200 $mV \cdot s^{-1}$, indicating its long-term electrochemical stability. Zhao et al. fabricated the porous VN NW/CNT film (CNTF) via a facile one-step hydrothermal process, followed by a thermal annealing process.[113] The synthesis of VN NW/CNTF is shown in Fig. 8b. The all-solid-state flexible ASC device, which comprises porous VN NWs/CNTF as the negative electrode material, cabbage-like $ZnCo_2O_4$/CNTF as the positive electrode material, and PVA/KOH gel electrolyte as a separator, exhibited the capacity retention of 87.9% and the coulombic efficiency of 100% after 4000 cycles, as shown in Fig. 8e. Fig. 8f shows that the high energy density of the device can reach 64.76 $mWh\cdot cm^{-3}$ at a power density of 800 $mW\cdot cm^{-3}$. Composite materials, containing the fibrous VNNPs and MWCNT, were developed by Su et al. using chemical method.[114] It was found that VNNPs coated on the MWCNT matrix enhanced electrochemical performance.[115] However, the capacitance decreased with increasing VN mass loading. The hybrid cell assembled with VN-MWCNT as the negative electrode and MnO_2-MWCNT as positive electrode exhibited the energy density of $38.7Wh\cdot g^{-1}$ (19.4 $mWh\cdot cm^{-3}$) and the power density of 7.3 $W\cdot kg^{-1}$ ($mW\cdot cm^{-3}$) in a voltage window of 1.8 V in aqueous 0.5 M Na_2SO_4 electrolyte.

In the process of cycles, the instability of transition metal nitride is attributed to the presence of oxygen and/or water containing electrolytes, which leads to low capacitance. An et al. proposed a novel structure comprising VN encapsulated CF networks with furrowed porous surfaces prepared by electrospinning followed by an optimal stabilization and carbonization treatments (Fig. 9h).[116] Commercial VN has low specific capacitance, because it can be easily oxidized in oxygen and/or water, which impedes the electrochemical reaction of VN, as illustrated in Fig. 9b. Meanwhile, it can be seen from Fig. 9c that CF coating prevents the oxidation of VN. When tested as an electrode for SCs, the VN-CF electrode displayed excellent cycling stability with superb capacitance retention of 96.4, 95.3, and 92.9% at current densities of 4, 40, and 80 $A\cdot g^{-1}$, respectively, even after 10 000 cycles, as indicated in Fig. 9d. Zhang et al. developed a facile and effective approach to directly grow well-aligned 3D VN NWAs on CNT fiber for assembling fiber-shaped SCs (FSSs).[117] The areal specific capacitance of the VN@C NWA/CNT electrode was 715 $mF\cdot cm^{-2}$ at a current density of 1 $mA\cdot cm^{-2}$. When manufacturing a prototype asymmetric coaxial FSS (ACFSS) (Fig. 9e, 9f and 9g) with a maximum operating voltage of 1.8 V, the CNT fiber core coated with VN@C NWAs was used as the negative electrode, achieving 90% capacitance retention after 6000 cycles. In addition, the ACFSS device was woven into the flexible powering textile, which demonstrated its favorable stitchability.

Nitrogen-doped carbon (NC) has attracted great attention due to its excellent hydrophilic properties, electrical conductivity and electrochemical stability. As a supporting skeleton, NC nanosheets (NCS) are beneficial to prevent the aggregation of VNNPs and improve the cycling life and the electrical conductivity of the composites. Jiang et al. prepared VN/NC nanocomposites using g-C_3N_4 as the nitrogen source by a facile one-step annealing process.[118] For X-VN/NCB, X-VN/NCS2, X-VN/NCS4, X-VN/NCS6, NCB refers to the NCS synthesized from the bulk g-C_3N_4, NCS2, NCS4 and NCS6 indicate the NCS obtained from the g-C_3N_4 nanosheets with different thickness through thermal exfoliating of the bulk g-C_3N_4 for 2 h, 4 h and 6 h, respectively, “X” denotes the mass of NH_4VO_3. The specific capacitance valves of 0.06-VN/NCS2, 0.04-VN/NCS2, 0.03-VN/NCS2, NCS2 and commercial VN electrodes at a current density of 1 $A\cdot g^{-1}$ were respectively 137 $F\cdot g^{-1}$, 299 $F\cdot g^{-1}$, 187 $F\cdot g^{-1}$, 28 $F\cdot g^{-1}$ and 16 $F\cdot g^{-1}$. Even after 5000 cycles, 72% initial capacitance of the 0.04-VN/NCS2 composite electrode still remained, suggesting an exceptional cycling life.

Recently, flexible quasi/all-solid-state SCs as flexible energy storage systems have aroused great interest due to their high-power density, long cycle life, ease of operation, excellent reliability upon deformation, as well as cost-effectiveness. However, a reliable, flexible electrode, an important component of SCs, must have both high electrical conductivity and excellent mechanical robustness. The composite material of carbon-based materials (graphene) with low specific capacitance and VN with high capacitance and electrical conductivity prepared by Yu et al. utilized as flexible quasi/all-solid-state SC electrodes. The VN-G electrode showed high specific capacitance and good cycling stability of retaining 90% after 3000 cycles in KOH/PVA solid electrolyte.[42] More importantly, VN-G material delivered favorably high sensitivity (40 kPa^{-1} at the range of 2-10 kPa), fast response time (~130 ms), and outstanding stability under static and dynamic pressure conditions, which indicate it can detect various physiological signals in ultrasensitive health monitoring.

Graphene oxide (GO), as an energy-related substrate, shows excellent electrical, mechanical, thermal properties, and so on. He et al. firstly used the method combining electrochemically controlled surface-initiated atom transfer (SI-eATRP) technique and thermal-treatment to synthesize VNNP/GO.[119] The fabrication process is illustrated in Fig. 9a. The synergistic effect of VN and GO significantly improved electrochemical properties. The specific capacitance of VNNP@GO retained 109.7 $F\cdot g^{-1}$ at 1 $A\cdot g^{-1}$ and its capacitance retention rate still reached 93% of the initial capacity after 5000 cycles.

To improve the electrochemical performance of VN/G, N doped plays an indispensable role in energy storage. Liu et al. reported hybrid VN/N-doped graphene (VN/N-G) nanocomposites by pyrolysis of a mixture of GO, V(IV) oxide sulfate hydrate and cyanamide under an N_2

atmosphere.[120] Fig. 10a shows the preparation of VN/N-G nanocomposites. By the in situ method, N can be doped uniformly in the carbon matrix, while for the heat treatment under NH_3 gas, only at the defect sites and/or the edges of the carbon matrix. In addition, calcination temperature greatly influenced the structure, VN_xO_y and doping N content of VN/N-G, as well as the corresponding electrochemical performance. It was found that VN/N-G at 700 °C manifested a high specific capacitance of 342.1 $F\cdot g^{-1}$ at 0.5 $A\cdot g^{-1}$ in a 2 M KOH aqueous electrolyte. Balamurugan et al. synthesized the novel VN/nitrogen-doped graphene (VN/NG) composite (Fig. 10c) using a modified Hummers method.[121] Fig. 10d shows the HR-TEM image indicating the thin layer of porous VN nanostructure homogeneously distributed on the NG surface. When applied as an electrode, the as-prepared composites exhibited excellent storage capacity, with a specific capacitance of 445 $F\cdot g^{-1}$ at 1 $A\cdot g^{-1}$, a wide operation window (-1.2 to 0 V), and a capacity retention rate of 98.44% after 10 000 cycles at 10 $A\cdot g^{-1}$.

5.3 VN/transition metal materials

Although VN has large theoretical specific capacitance, reversible faradaic redox response, and low cost, its low conductivity and inefficient ionic transport are still a significant challenge. By designing 3D hierarchical architecture and using conductive addition, it is possible to resolve this problem. Ji et al., utilizing Ni nanoparticle as conductive addition, introduced Ni nanoparticles doped VN 3D hierarchical hollow microspheres with 2-4 nm mesopores and surface area of 57.3 $m^2\cdot g^{-1}$ and the nitridation treatment of $Ni_{1-x}V_xO_2$ material.[122] The synthesis process is shown in Fig. 10b. Assembled Ni/VN//$Ni_{1-x}V_xO_2$ ASC exhibited excellent cycling stability, with 87% specific capacitance retention after 1000 cycles. To improve VN material electrochemical performance, Jiang et al. synthesized the X-Ni/VN/NCs-Y (X denotes the mass percent of Ni nanoparticles, Y indicates the mole ratios of melamine to VNNPs) composite of ultra-small Ni nanoparticles and VNNPs embedded in NCs nanosheets.[123] The 3-Ni/VN/NCs-7 nanocomposite with the large specific area (58 $m^2·g^{-1}$) and the even pore size (about 22 nm) had rapid ion/molecule transport pathways and exhibited the specific capacitance of 236 $F·g^{-1}$ at 1 $A·g^{-1}$ and superb cycling stability.

Transition metal nitrides are desirable candidates for SCs due to their low cost, high molar density, superior chemical resistance. However, titanium nitride (TiN) showed a better electronic conductivity but with low capacity. Therefore, utilizing VN with high capacity and TiN via the coaxial electrospinning and subsequently annealed in the ammonia, Zhou et al. obtained core-shell (TiN-VN) fibers with 169 $m^2·g^{-1}$ of the surface area and the average pore size of 30.2 nm.[124] The TiN-VN fiber indicated higher specific capacitance (2 $mV·s^{-1}$, 247.5 $F·g^{-1}$) and better rate capability (50 $mV·s^{-1}$, 160.8 $F·g^{-1}$). Wei et al. introduced TiVN composites hollow mesospheres (HMs) by combining the higher capacitance of VN and higher electronic conductivity of TiN through a facile solvothermal method issuing nitridation by C_3N_4.[125] According to the Ti/V different molar ratio of 1:1, 2:1 and 3:1, three TiVN-HMs samples were prepared, which were denoted as Ti_1V_1-HMs, Ti_2V_1-HMs and Ti_3V_1-HMs, respectively. Fig. 10e and Fig. 10f shows that the nanospheres were homogeneously distributed with a diameter of about 100 nm and hollow structure and 15 nm of the shell thickness. Moreover, Ti_2V_1-HMs exhibited a high specific capacitance of 729 $F·g^{-1}$ at 2 $A·g^{-1}$.

In summary, VN materials have various preparation methods and good cycle stability. Although many research mechanisms of VN have been put forward, various theories are still a controversial case, which needs to more theoretical calculation and technical proofs. Moreover, it is very difficult to produce VN materials on a large scale because of some synthesis conditions are still hardly realized. So a preparation technique with low energy consumption and high yield should be explored.

6 Vanadium sulfide and its composites

6.1 VS_2 and its composites

VS_2 is considered to be a promising candidate for SC application as maximum electrical conductivity, high surface area and unique electronic structure, which is attributed to the fact that VS_2 essentially maintains a V-shaped structure and layered structure crystals stacked by van der Waals forces. Pandit et al. successfully used successive ionic layer adsorption and reaction (SILAR) method to deposit VS_2 thin film onto flexible and light-weight stainless steel substrates (Fig. 11c).[126] When assembled into a flexible symmetric solid-state SC device, the VS_2 electrode exhibited strong cycling stability by gaining its 89% capacitive value of its initial cycle after 6000 cycles and obtaining specific energy of 25.9 $Wh \cdot kg^{-1}$ at a specific power of 1.5 $kW \cdot kg^{-1}$. Feng et al. developed a unique ammonia-assisted strategy to obtain VS_2 thin film with less than five S-V-S single layers for the construction of high performance in-plane SCs.[127] The process of thin-film is shown in Fig. 11d, 11e and 11f. In 150 nm in-plane configuration, VS_2 thin-film realized a capacitance of 4760 $\mu F \cdot cm^{-2}$ in PVA gel with a water-soluble ionic liquid of $BMIMBF_4$. Meanwhile, no obvious degradation of capacitance was observed even after 1000 charge/discharge cycles, revealing the excellent cycling behavior. Guo et al. prepared ultrathin VS_2 nanoplates by a colloidal method.[128] When utilized as the anode materials for a three-electrode systems, these rich-defect nanoplates showed ultrahigh specific capacitance of 2200 $F \cdot g^{-1}$ at a current density of 1 $A \cdot g^{-1}$. It is found in Fig. 11g that two ASCs (VS_2//AC) light an OUC light-emitting diode (LED) panel for at least 10 minutes, demonstrating its great potential for application.

However, VS_2 nanosheets are vulnerable to stacking and aggregating to multilayers during the drying process owing to the high surface energy and interlayer van der Waals attraction, which leads to dramatic changes in physical and chemical properties, especially the decrease in the number of the active sites and electrical conductivity. Zhang et al. constructed a novel type of nonaqueous Na-ion hybrid micro-supercapacitors with wide potential window (0.01-3.5 V) and ultrahigh areal energy density, using VS_2 nanosheets grown on electrochemically exfoliated graphene as the negative electrode and activated carbon as the positive electrode in nonaqueous sodium-ion electrolyte.[129] The as-fabricated nonaqueous Na-ion hybrid MSCs exhibited an excellent cyclability of up to 5000 cycles without capacitance fading. And the areal capacitance reaches 110.7 $mF \cdot cm^{-2}$ at 0.2 $mA \cdot cm^{-2}$ and the areal energy density can be as high as 188.3 $\mu Wh \cdot cm^{-2}$ at 0.35 $mW \cdot cm^{-2}$.

ZnO has the advantages of high theoretical capacitance, high energy density and low cost but its poor conductivity and low mechanical stability. Therefore, Fang et al. synthesized cauliflower-like nanocomposite by in situ growth of ZnO nanospheres on the ultrathin VS_2 nanosheets using a facile wet chemical method.[130] Fig. 11b shows the schematic diagram of the formation of the ZnO/VS_2 nanoarchitecture. The ZnO/VS_2 nanocomposite contributed an ultrahigh specific capacity of 2695.7 $F \cdot g^{-1}$ at a current density of 1 $A \cdot g^{-1}$ with remarkable stability where 92.7% of its capacity retained after 5000 cycles due to the synergetic effects. Zhang et al. fabricated 2D VS_2 nanosheets along with the $NiCo_2S_4$ needle arrays ($NiCo_2S_4@VS_2$) via an in situ sulfurization-assisted hydrothermal process to prevent stacked property and to increase its active sites.[35] Fig. 11a illustrates the synthesis route of free-standing $NiCo_2S_4@VS_2$ nanoneedle arrays on

3D sponge-like nickel foam. The large surface area, short ion transport path and increased active site for redox reaction contributed to the increased capacity, as shown in Fig. 11h. $NiCo_2S_4@VS_2$ exhibited extremely excellent SCs performance including high specific capacitance (1023.4 $C\cdot g^{-1}$ at a current density of 0.45 $A\cdot g^{-1}$) and long term cycling stability (96% capacitance retention after 2000 cycles).

6.2 VS_4 and its composites

VS_4 has 1D crystal structure and high content of sulfur compared with transition mental sulfides such as MoS_2, CoS_2, NiS_2, which facilitates the charge-transfer kinetics due to the weak interaction between neighbor chains, performing excellent electrochemical behavior. Further, the interval between the atomic chains offers abundant active sites for ions diffusion and storage and high electronic conductivity. However, the synthesized method of pure VS_4 has not been explored in the past time. It was reported recently that pure VS_4 can be prepared using carbon-based material as active templates. VS_4/CNTs composite had been reported by Wang et al. through a one-step hydrothermal reaction, whose preparation route is shown in Fig. 13d.[131] For 1 M $LiClO_4$ in PPC electrolyte, the VS_4/CNTs composite electrode delivered an outstanding specific capacitance of 330 $F\cdot g^{-1}$ (924 $C\cdot g^{-1}$) at 1 $A\cdot g^{-1}$ in the potential window of -1.4 V to 1.4 V. The VS_4/rGO containing 0.75 wt % of rGO, 1.5 wt % of rGO and 3 wt % of rGO reported by Ratha et al. was hereafter denoted VS_4/rGO_0.75, VS_4/rGO_1.5 and VS_4/rGO_3, respectively.[132] Among these, VS_4/rGO_1.5 showed a high specific capacitance of about 877 $F\cdot g^{-1}$ at a current density of 0.5 $A\cdot g^{-1}$ compared to those of VS_4/rGO_0.75 (223 $F\cdot g^{-1}$) and VS_4/rGO_3 (259 $F\cdot g^{-1}$). To improve the performance of the electrode material, the VS_4/CNTs/rGO hybrid was introduced by Ratha et al.[133] Compared with VS_4/CNTs and VS_4/rGO, the hybrid expressed excellent energy density and capacitance values due to the synergistic interaction between CNTs and rGO in VS_4/CNTs/rGO. In addition, binder-free patronite (VS_4) flower-like nanostructures were synthesized on CC by a facile hydrothermal method, and then VS_4-CC@VS-3 (the mass loading of VS_4 on CC is 1.3 $mg{\cdot}cm^{-2}$) was received by controlling the concentrations of V and sulfur sources along with the complexing agent in the growth solution by Ramu et al..[134] The synthesis process of ferox fruit-like patronite nanostructures on flexible CC under the pH-controlled growth medium is illustrated in Fig. 13a. As shown in Fig. 13e, VS_4-CC@VS-3 electrode for the SSCs displayed better areal capacitance retention of ~93% even after 1000 cycles 1 M 1-ethyl-3-methylimidazolium trifluoromethanesulfonate ([EMIM][OTf]) electrolyte. To further improve the electrochemical properties, Wang et al. synthesized hierarchical VS_4/rGO/CoS_2@Co (VRCS@Co) nanocomposite cathode material with multidimensional structure by in-situ synthesized on Co foam through a simple one-step hydrothermal process in the presence of GO.[135] The nanocomposite manifested a high capacitance of 274.3 $mAh{\cdot}g^{-1}$ (1353 $F{\cdot}g^{-1}$) at 0.625 $A{\cdot}g^{-1}$. Fig. 13f shows that the specific capacitance retentions of VRCS@Co cathode was 89.6% even after 20 000 cycles, while that of GO + $NaVO_3$@Co (VRC@Co) and thiourea (3) + $NaVO_3$@Co (VCS@Co) were 42% and 63.2% after 10 000 cycles. It was found that the outstanding cyclic stability may be attributed to its unique architecture of 0D CoS_2 spheres-anchored 2D VS_4 lamellae.

7 Metal vanadate and its composite materials

7.1 Cobalt vanadate and its composites

Cobalt vanadate and its composites are one of the well-known SC materials because of its natural abundance, environment friendliness, low cost, and better chemical properties. A variety of morphologies and structures have been achieved, such as 3D porous hydrated cobalt pyrovanadate microflowers[136], CoV_2O_6 micron blocks[137], $Co_3V_2O_8$ nanoparticles[137] and so on. The electrochemical performance of cobalt vanadate is affected by the valence of V (conductivity), morphology, crystallinity, crystal structure and mass loading in composites. The cobalt vanadate-based electrode stores the electric charges by pseudocapacitive mechanism. The charge storage arises from the II/III oxidation state change at or near the surface of cobalt vanadate nanostructures.

To store electric charge, faraday reaction occurs on the electrode surface, which is the adsorption/desorption of electrolyte ions and/or protons on the electrode surface, whereas the bulk pseudocapacitive reaction depends on the intercalation/deintercalation process of either protons or cations into the bulk of cobalt vanadate. Sun et al. prepared the 3D porous $Co_2V_2O_7 \cdot 3.3H_2O$ microflowers by a facile co-preparation method.[136] Fig. 12a shows the fabrication of $Co_2V_2O_7 \cdot 3.3H_2O$ microflowers. The specific capacitance was 351 $F \cdot g^{-1}$ at a current density of 1 $A \cdot g^{-1}$, and an ultralong cycle lifetime with 103% capacitance retention after 30 000 cycles (Fig. 12e). Teng et al. firstly used the microwave-assisted hydrothermal method to synthesize CoV_2O_6 miron blocks and CoV_2O_8 nanoparticles.[137] When used as an electrode, CoV_2O_8 nanoparticles displayed a higher specific capacity compared to CoV_2O_6 miron blocks. Meanwhile, the specific capacity of CoV_2O_6 and CoV_2O_8 maintained 81.91%, 94.67% of the initial value after 1000 cycles. It was found that CoV_2O_8 nanoparticles exhibited better cycling stability. $Co_3V_2O_8$ nanoparticles as a new class of high-performance electrode material for SCs were designed and synthesized by Liu et al., found that its specific capacitance was 505 $F \cdot g^{-1}$ at a current density of 0.625 $A \cdot g^{-1}$.[138] $Co_3V_2O_8$ thin sheets were synthesized via a succinct-operated hydrothermal method as SC electrode material by Huang et al., showing a remarkable specific capacity of 1320 F·g^{-1} at 1 A·g^{-1} and superior cycle stability.[36] Zhang et al. synthesized 3D $Co_3O_4/Co_3(VO_4)_2$ hybrid nanorods on the conductive substrate of nickel foam by the combination of hydrothermal synthesis and subsequent annealing treatment.[139] The electrode of three-dimensions $Co_3O_4/Co_3(VO_4)_2$ hybrid nanorod manifested satisfying capacitance of 847.2 F·g^{-1}, outstanding rate capability, and excellent cycling stability.

7.2 Nickel vanadate and its composites

Nickel vanadate is a good electrochemical material in SCs, its high theoretical SCs is up to 1992.5 F·g^{-1}.[36] Nickel vanadate and its composites have long cycling stability, low cost, high electrical conductivity, and multiple oxidation states, making it a suitable candidate in SC applications.[140] Kumar et al. fabricated 3D urchin-shaped $Ni_3(VO_4)_2$ hollow nanospheres by a facile, template-free hydrothermal method.[141] Fig. 12d shows the CV curves of $Ni_3(VO_4)_2$ nanospheres at various scan rates ranging from 5 to 100 mV·s^{-1}. The linear increase in peak current with an increase in scan rate suggests that the faradaic redox reaction kinetics and the ionic and electronic charge transport are rapid even at higher scan rates. Furthermore, the oxidation and the reduction peak potential shifted towards positive and negative directions, respectively. In addition, the different morphologies of nickel vanadate impressed electrochemical properties. The porous urchin-shaped $Ni_3(VO_4)_2$ nanospheres electrode exhibited a specific capacity of 402.8 C·g^{-1} at 1 A·g^{-1}, and had an enhanced rate capability and capacity retention of 88% after 1000 cycles. The 2D hierarchical porous nickel vanadate thin sheets were synthesized by Huang et al. via a succinct-operated hydrothermal method, its specific capacity was 1992.5 F·g^{-1} at a current density of 1 A·g^{-1} and with 83.9% capacity retention after 10 000 cycles.[36] $Ni_3V_2O_8$ was synthesized by Liu et al., which manufactured a high specific capacitance (1181 $F \cdot g^{-1}$) at a current density of 0.625 $A \cdot g^{-1}$, only 73% of the capacitance was retained after 1000 cycles.[138] In addition, 3D nanosheet arrays of $Ni_3(VO_4)_2$ directly grown on Ni foam through a facile one-step hydrothermal route was used as an electrode for non-enzymatic glucose detection. The irreversible catalytic oxidation reaction of glucose to gluconolactone was catalyzed by the $Ni(OH)_2$/NiOOH redox couple and can be shown in Fig. 13b.[142] The electrode possessed high sensitivity and selectivity along with long term stability, good flexibility and reusability. The $Ni_3V_2O_8$@PANI composite prepared by Liu et al. using an in situ chemical bath method, and found that it had outstanding electrochemical behaviors (specific capacitance value of 2565.7 $F \cdot g^{-1}$ at 5 $mV \cdot s^{-1}$, wide potential window, good rate capability).[143] Fig. 12c is a schematic illustration of the synthesis of electrode materials and the fabrication of the device. Size and shape controlled nickel oxide/nickel vanadate ($NiO/Ni_3V_2O_8$) nanocomposites were achieved by solvothermal method, its electrode estimated 653 $F \cdot g^{-1}$ specific capacitance at current density 1 $A \cdot g^{-1}$ due to nanorods regular arrangement with uniform size distribution.[144] Co-incorporated $NiV_2O_6/Ni(HCO_3)_2$ nanoflakes grown on nickel foam showed superior long-term durability with 106.2% retention of the initial capacity after 10 000 charging/discharging cycles at 100 $mA \cdot cm^{-2}$.[145]

Cobalt vanadate and nickel vanadate both have a good electrochemical performance. So what is the property of combining cobalt vanadate and nickel vanadate? Huang et al. prepared 2D hierarchical porous $M_3V_2O_8$ (M = Co, Ni and Co-Ni) thin sheets, and observed that the $Co_3V_2O_8$-$Ni_3V_2O_8$ nanocomposite possessed the specific capacitance of 2617.5 $F \cdot g^{-1}$.[36] As shown in Fig. 12g, $Co_3V_2O_8$-$Ni_3V_2O_8$ nanocomposite demonstrated higher capacity retention (91.4%) after 10 000 cycles in comparison to those of $Co_3V_2O_8$ and $Ni_3V_2O_8$. However, mesoporous $Co_3V_2O_8$-$Ni_3V_2O_8$ thin layers@porous carbon nanofibers were fabricated by Hosseini et al. for flexible all-solid-state SCs.[146]. It showed lower cycling stability (88.5% capacitance retention after 3000 cycles at 5.0 $A \cdot g^{-1}$) compared to $Co_3V_2O_8$-$Ni_3V_2O_8$ nanocomposite

7.3 Other mixed metal vanadates

Other mixed metal vanadates have rarely been studied for SCs in the past, such as zinc vanadate, aluminum vanadate, bismuth vanadate, and so on. Zinc vanadate was studied and had a good performance in many fields, including its photocatalytic properties[147, 148], luminescence characteristics [149], properties in lithium batteries [13], hydrogen storage properties [148], and magnetic properties [150]. However, there are challenges in the study of the pseudocapacitive properties of zinc vanadate, such as the complex and time-consuming of the synthesis approaches[150], the poor electrochemical properties (low specific capacitance and poor cycling performance).[151] Zinc vanadate was specifically studied due to its various morphologies (hierarchical microspheres, nanosheets, NWs, and so on) and its various binding modes ($Zn_3V_2O_8$, $Zn_3(OH)_2V_2O_7 \cdot 2H_2O$, $Zn_2V_2O_7$ and so on).

$Zn_3(OH)_2V_2O_7 \cdot 2H_2O$ NWs were successfully synthesized through a facile, rapid, and green microwave-assisted hydrothermal method, its electrode was 207.8 $F \cdot g^{-1}$ specific capacitance at a scan rate of 1 $mA \cdot cm^{-2}$, and only retained 53.50% of its initial capacitance.[151] The as-synthesized $Zn_2V_2O_7$ elliptical nanoparticles electrode exhibited a superior specific capacitance of 427.7 $F \cdot g^{-1}$ (at 1 $mA \cdot cm^{-2}$) and enhanced cycling performance, with 83.71% capacitance retained after 1000 cycles. Low et al. reported that graphene-$Zn_3V_2O_8$ nanocomposites were subjected to a facile solvothermal process and then thermal annealing treatment.[152] The synthesis of graphene-$Zn_3V_2O_8$ nanocomposite is shown in Fig. 12f. The specific capacitance of the nanocomposite was 564 $F \cdot g^{-1}$ at 0.8 $A \cdot g^{-1}$ in 2 M KOH aqueous electrolyte. Furthermore, the materials also showed outstanding rate capability and good cycling stability even after 5000 cycles.

$BiVO_4$, an n-type semiconducting material, is abundant, relatively inexpensive, and offers a broad range of oxidation states, and become a superior candidate for SC applications. Packiaraj et al. synthesized $BiVO_4$ nanoparticles by the simple hydrothermal method.[153] When used as an electrode for SCs, $BiVO_4$ nanoparticles obtained the maximum capacitance value of 1166 $F{\cdot}g^{-1}$ at 1 $A{\cdot}g^{-1}$. However, $BiVO_4$ has the disadvantage of poor electrical conductivity as a metal oxide. It is very important to combine carbon-based material of high electrical conductivity with $BiVO_4$. Graphene/bismuth vanadate composite was introduced via a hydrothermal process by Deng et al..[154] The specific surface area was 36 $m^2{\cdot}g^{-1}$ and the average pore size was about 23.5 nm. The GR/$BiVO_4$ monolith composite exhibited an impressive specific capacitance of 479 $F{\cdot}g^{-1}$ in a potential window of -1.1 to 0.7 V. Similarly, fabricating rGO/$BiVO_4$ hybrid nanostructures, obtained by Patil et al. that exhibited outstanding volumetric energy density of 1.6 $mWh{\cdot}cm^{-3}$ (33.7 $Wh{\cdot}kg^{-1}$) and ensured rapid energy delivery with the power density of 391 $mW{\cdot}cm^{-3}$ (8.0 $kW{\cdot}kg^{-1}$).[155]

Amorphous TMOs may exhibit unique physical and chemical properties with more active sites and isotropic nature active sites due to their disorder structures. And aluminum vanadate is one of the few species in SCs. Amorphous aluminum vanadate hierarchical microspheres were developed via a simple hydrothermal approach by Yan et al..[156] The amorphous aluminum vanadate electrode showed 497 $F{\cdot}g^{-1}$ at 1 $A{\cdot}g^{-1}$ and good stability and retention capacity of 89% after 10 000 cycles.

Li ion capacitors were firstly introduced and attracted much attention in 2001 because of its bridge between electrochemical capacitors and Li-ion batteries.[157] Wang et al. developed a quasi-solid-state Li ion capacitors with Li_3VO_4 based composites as anode and electrochemically-exfoliated graphene sheets as cathode in a gel polymer electrolyte.[158] A power density of 3870 W·kg^{-1} at energy density of 28 Wh·kg^{-1} can be achieved even in a gel polymer electrolyte.

The synthesized mixed metal vanadates for SCs have shown a good electrochemical performance, and its specific capacity is higher than that of vanadium oxide, vanadium sulfides and vanadium nitrogen, so it is the most promising vanadium-based material. Therefore, many mixed metal vanadates are worth developing for SCs.

8 Other V-based materials

Vanadium oxide has higher theoretical specific capacitance and potential window than those for other TMOs owing to the multiple vanadium oxidation states (V^{2+}, V^{3+}, V^{4+} and V^{5+}). Nest-like V_3O_7 was thoroughly investigated to the energy storage mechanism and found that V_3O_7 was converted to V_6O_{13} at the lowest potential of -0.6 V and V_2O_5 at the highest potential of 0.2 V. By annealing the precursor of V_3O_7@PPy prepared by an in situ photopolymerization method, NC-coated nest-like V_3O_7 (NC-V_3O_7) was fabricated by Zhao et al..[159] The synthesis process of NC-V_3O_7 NW is presented in Fig. 12b, respectively. The capacitance of NC-V_3O_7 remained 80.47% of the initial capacitance at 10 A·g^{-1} after 4000 cycles, which was much higher than that of V_3O_7 (23.16%). It was found that its superior capacitance and stability was attributed to the unique three-layer structure (C bonded both to V and N) stabilized V_3O_7 and supported high-speed ionic and electronic transmission channels.

V_6O_{13} has aroused widespread interest because of its high specific capacitance and good cycle ability for lithium batteries, but it is rarely used in SCs. Meanwhile, V_6O_{13} has the blended valence of V(IV) and V(V), increasing the electronic conductivity of the material. Zeng et al. utilizing a thermal decomposing and quenching method with NH_4VO_3 as the starting material, synthesized V_6O_{13} sheet with an average size of 2 μm and a thickness of about 200 nm.[160] The V_6O_{13} electrode maintained obvious capacitance performance in the voltage range of -0.2 to 0.8 V in 1 M $NaNO_3$ electrolyte. Moreover, Zhai et al. reported sulfur-doped, oxygen-deficient V_6O_{13-x} as an anode electrode via a two-step process.[161] The capacitance of 1353 $F{\cdot}g^{-1}$ achieved at a current density of 1.9 $A{\cdot}g^{-1}$ in 5 M LiCl solution since the Li^+ diffusion coefficient and charge transfer efficiency of the V_6O_{13-x} electrode was improved. However, V_6O_{13-x} was dissolved to form V(III) oxide as soluble vanadate ions during cycling in aqueous electrolyte, which make its rapid capacitance degradation. To suppress the irreversible chemical dissolution of V^{3+}, the sulfur-doped, oxygen-deficient V_6O_{13-x} was deposited a layer of thin carbonaceous film, which achieved outstanding capacitance retention of 92.3% after 10 000 cycles.

$VOPO_4{\cdot}2H_2O$ was considered as a high potential electrode material, which was attributed to its peculiar layered structure with VO_6 octahedra and PO_4 tetrahedra, safety, low cost, and environmental friendliness, possessed the higher potential than vanadium oxide. Luo et al. used reflux and hydrothermal methods to fabricate $VOPO_4{\cdot}2H_2O$, and found that the material synthesized by the reflux method (202 $F{\cdot}g^{-1}$ at 2 $mV{\cdot}s^{-1}$) had better capacitance than that by hydrothermal method (100 $F{\cdot}g^{-1}$ at 2 $mV{\cdot}s^{-1}$), because the former electrode material had a small resistance and the fast pseudocapacitance reaction.[162] To prepare the amorphous $VOPO_4$/graphene composite, Chen et al. firstly exfoliated bulk layered $VOPO_4{\cdot}2H_2O$ crystal, and then hydrothermal treatment with GO.[163] The amorphous $VOPO_4$ structure shortens the ion transport path, offers more reversible and fast faradic reaction sites and improves the unique layer-on-sheet nanohybrid structure. The synthesis of amorphous $VOPO_4$/graphene composites is shown in Fig. 13c. And compared with the different mass of $VOPO_4$/graphene composite, $VOPO_4$/graphene (2:1) composite electrode remained good cycling stability (retention 80% after 5000 cycles at 2 $A·g^{-1}$) than those of $VOPO_4$/graphene (1:2) composite and $VOPO_4$/graphene (4:1) composite. It is found in Fig. 13g that the amorphous $VOPO_4$/graphene (2:1) composite as an electrode material for SCs showed a high specific capacitance (508 $F·g^{-1}$ at 0.5 $A·g^{-1}$) and an excellent rate capability (359 $F·g^{-1}$ at 10 $A·g^{-1}$). By comparison, $VOPO_4$/graphene (2:1) composite electrode stills remained about 80% of its original value after 5000 cycles, as shown in Fig. 13h. Wu et al. reported α_I-vanadyl phosphate ultrathin nanosheets with less than six atomic layers, an inorganic graphene analogue, which constructed flexible ultrathin-film SCs and realized a high areal capacitance of 8360.5 $mF·cm^{-2}$.[164]. In addition, the hybrid $VOPO_4$/graphene film also was prepared, demonstrating excellent long-term cycling stability (96% after 2000 cycles). Similarly, different mass ratios of $VOPO_4$/rGO hybrid were introduced by He et al. by using a deintercalation-intercalation reaction process.[165] The electrode with a mass ratio of $VOPO_4/rGO = 1$ showed a high specific capacitance. Chen et al. synthesized vanadyl phosphate/carbon nanocomposites by a simple two-step approach, in which dodecylamine was intercalated layered $VOPO_4·2H_2O$ and then it was in situ carbonization at 400 °C.[166] According to the electrochemical results, the nanocomposite electrode exhibited a high specific capacitance of 469 $F·g^{-1}$ at a current density of 1 $A·g^{-1}$ and excellent rate performance.

Vanadium carbide (V_2CT_x) based MXene has a wide working potential window and sloping charge-discharges for Li-ion batteries. V_2CT_x was proposed for Na ion capacitors by Dall'Agnese et al., which showed a potential window ranging from 1 to 3.5 V versus Na^+/Na, being attractive as a positive electrode in Na ion capacitors.[167]

9 Conclusion and Outlook

All in all, this article describes the application of V-based materials in SCs. Meanwhile, their synthesis methods, morphology, and electrochemical performance are presented. V-based materials have attracted tremendous attention in electrochemistry due to various valences, abundant resources, and low cost. However, their poor electrical conductivity, low structure stability, inferior rate performances, and low specific capacitance and energy density limit its practical applications. Therefore, it is critical to design stable, porous, electrically conductive materials for SCs. According to the published articles, the future development direction of the material is as follows:

Firstly, the development of new materials still is an important task in energy storage. So far, the novel structure and hybrid materials are main explored means, which can enrich the treasure house of materials and create good conditions for further development of their properties. In this review, apart from V_2O_5, the rest of the V-based materials should be fully combined with metal/metal compounds, carbon-based materials, and conductive polymers because these materials can correspondingly increase their specific surface area, conductivity, and further increase their specific capacity, rate performance, cycle stability, energy density and power density. And V_2O_5 should further explore its corresponding novel composite materials. Moreover, for the same material, different synthesis methods will produce the same or different morphologies, and the corresponding electrochemical properties are also very different. At present, there is no specific synthesis method or specific synthesis conditions for V-based materials to have good performance. Therefore, a large number of experiments to explore new materials and synthesis methods are particularly important in the future development.

Secondly, preparing porous structured materials improves the specific surface area and active site. High specific surface area can offer more active sites, increase the contact between the material and electrolyte, generate more redox reactions, and shorten the electron and ion transport paths. As mentioned above, these will greatly improve the energy storage performance of materials. An excellent electrochemical behavior, which is related to the nature of the material, is also correlated to the morphology and synthesis method. Porous materials can effectively improve the utilization rate of materials and accelerate the transmission of ions/electrons. However, according to the reported large amount of publications, there are few materials with high specific area. In order to solve this problem, nano-scale materials with porous structure should be synthesized in future research.

Thirdly, ASCs are assembled by developing new electrode materials and electrolytes. In ASCs, V-based materials are used as the positive/negative electrode, while new electrode materials are utilized as the negative/positive electrode, which will broaden the operating voltage window and enhance the electrochemical performance. So it's important to choose and develop new electrodes. Besides, the electrolyte also has an influence on electrochemical behavior. For some V-based materials, organic electrolyte has better electrochemical performance than inorganic electrolyte. However, organic electrolytes are generally toxic and are not environmentally friendly in some applications. Environmentally friendly deep eutectic solvents (such as ULP), are a new low-cost neutral gel electrolyte and can promote the application of V-based materials in supercapacitors, which is worthy of reference and development. Meanwhile, the pH value of the electrolyte may affect the structure of V-based electrode material, resistivity and proton transmission rate, and even bring pollution to the environment. Therefore, it is still challenging and important to study the optimal pH in subsequent studies.

Lastly, in the research process of V-based materials, advanced characterization techniques are rarely mentioned. In order to understand the changes in the morphology of V-based materials during the electrochemical process and enhance the study of its mechanism, advanced characterization techniques should be studied.

In short, V-based materials are still challenging in SCs, such as the application of pure V_2O_3 and pure VS_4, the synthesis mechanism of VN, the research of various vanadates, and so on. These problems should be studied and discussed in depth in the future. Nowadays, V-based materials have shown a huge potential in practice application. Although there are many problems, it will become a research hot.

ACKNOWLEDGMENTS

This work is financially supported by the National Natural Science Foundation of China (No. 21101176 and 21676036), the Fundamental Research Funds for the Central Universities of Chongqing University (No. 2018CDQYCH0028, 2018CDXYHG0028 and 2019CDXYHG0013), the Graduate Research and Innovation Foundation of Chongqing (No. CYS18032), and the Large-scale Equipment Sharing Fund of Chongqing University (No. 201903150149 and 202003150020). S.W.C. thanks the National Science Foundation for partial support of the work (CHE-1710408 and CHE-1900235).

Conflicts of interest

The authors declare no competing financial interest.

References

1. T. Brousse, O. Crosnier, D. Bélanger and J. Long, in *Metal Oxides in Supercapacitors*, Elsevier, 2017, 1-24.
2. D. Dubal, O. Ayyad, V. Ruiz and P. Gomez-Romero, *Chem. Soc. Rev.*, 2015, **44**, 1777-1790.
3. M. Wu, J. Gao, S. Zhang and A. Chen, *J. Porous Mat.*, 2006, **13**, 407-412.
4. H. Hwang, D. Shin, T. Kim, S. Park, T. Yeo and W. Choi, *J. Mater. Chem. A*, 2018, **6**, 22998-23009.
5. C. Zhong, Y. Deng, W. Hu, J. Qiao, L. Zhang and J. Zhang, *Chem. Soc. Rev.*, 2015, **44**, 7484-7539.
6. M. Yu, Z. Wang, Y. Han, Y. Tong, X. Lu and S. Yang, *J. Mater. Chem. A*, 2016, **4**, 4634-4658.
7. X. Zhao, L. Mao, Q. Cheng, J. Li, F. Liao, G. Yang, L. Xie, C. Zhao and L. Chen, *Chem. Eng. J.*, 2020, **387**, 124081.
8. J. Theerthagiri, R. Senthil, P. Nithyadharseni, S. Lee, G. Durai, P. Kuppusami, J. Madhavan and M. Choi, *Ceram. Int.*, 2020, **46**, 14317-14345.
9. J. Shi, B. Jiang, C. Li, F. Yan, D. Wang, C. Yang and J. Wan, *Mater. Chem. Phys*, 2020, **245**, 122533.
10. M. Manikandan, K. Subramani, M. Sathish and S. Dhanuskodi, *RSC Adv.*, 2020, **10**, 13632-13641.
11. C. Zhao, X. Jia, K. Shu, C. Yu, G. Wallace and C. Wang, *J. Mater. Chem. A*, 2020, **8**, 4677-4699.
12. J. Yin, W. Zhang, N. Alhebshi, N. Salah and H. Alshareef, *Small Methods*, 2020, **4**,

1900853.

13. S. Vijayakumar, S. Lee and K. Ryu, *RSC Adv.*, 2015, **5**, 91822-91828.

14. Z. Shao, X. Cao, H. Luo and P. Jin, *NPG Asia Mater.*, 2018, **10**, 581-605.

15. C. Wu, F. Feng and Y. Xie, *Chem. Soc. Rev.*, 2013, **42**, 5157-5183.

16. D. Wegkamp and J. Staehler, *Prog. Surf. Sci.*, 2015, **90**, 464-502.

17. C. Armer, J. Yeoh, X. Li and A. Lowe, *J. Power Sources*, 2018, **395**, 414-429.

18. N. Chernova, M. Roppolo, A. Dillon and M. Whittingham, *J. Mater. Chem.*, 2009, **19**, 2526-2552.

19. E. Kianfar, *Microchem. J.*, 2019, **145**, 966-978.

20. Y. Wang and G. Cao, *Chem. Mater.*, 2006, **18**, 2787-2804.

21. R. Franz and C. Mitterer, *Surf. Coat. Tech.*, 2013, **228**, 1-13.

22. B. Gao, X. Li, K. Ding, C. Huang, Q. Li, P. Chu and K. Huo, *J. Mater. Chem. A*, 2019, **7**, 14-37.

23. V. Sharygin, G. Ripp, G. Yakovlev, Y. Seryotkin, N. Karmanov, I. Izbrodin, V. Grokhovsky and E. Khromova, *Minerals*, 2020, **10**, 1-19.

24. Y. Zhong, X. Xia, F. Shi, J. Zhan, J. Tu and H. Fan, *Adv. Sci.*, 2017, **4**, 1500286.

25. X. Xu, F. Xiong, J. Meng, X. Wang, C. Niu, Q. An and L. Mai, *Adv. Funct. Mater.*, 2020, **30**, 1904398.

26. Q. Wang, K. Kalantar-Zadeh, A. Kis, J. Coleman and M. Strano, *Nat. nanotechnol.*, 2012, **7**, 699.

27. C. Rout, B. Kim, X. Xu, J. Yang, H. Jeong, D. Odkhuu, N. Park, J. Cho and H. Shin, *J. Am. Chem. Soc.*, 2013, **135**, 8720-8725.

28. H. Fuess, E. Bertaut, R. Pauthenet and A. Durif, *Acta Crystallogr. B*, 1970, **26**, 2036-2046.

29. J. Xie, P. Yang, Y. Wang, T. Qi, Y. Lei and C. Li, *J. Power Sources*, 2018, **401**, 213-223.

30. R. Devan, R. Patil, J. Lin and Y. Ma, *Adv. Funct. Mater.*, 2012, **22**, 3326-3370.

31. R. Rakhi, D. Nagaraju, P. Beaujuge and H. Alshareef, *Electrochim. Acta*, 2016, **220**, 601-608.

32. Y. Zhang, X. Jing, Y. Cheng, T. Hu and C. Meng, *Inorg. Chem. Front.*, 2018, **5**, 2798-2810.

33. T. Hu, Y. Liu, Y. Zhang, Y. Nie, J. Zheng, Q. Wang, H. Jiang and C. Meng, *Micropor. Mesopor. Mat.*, 2018, **262**, 199-206.

34. X. Lu, M. Yu, T. Zhai, G. Wang, S. Xie, T. Liu, C. Liang, Y. Tong and Y. Li, *Nano Lett.*, 2013, **13**, 2628-2633.

35. Z. Zhang, X. Huang, H. Wang, S. Teo and T. Ma, *J. Alloy. Compd.*, 2019, **771**, 274-280.

36. B. Huang, W. Wang, T. Pu, J. Li, C. Zhao, L. Xie and L. Chen, *Chem. Eng. J.*, 2019, **375**, 121969.

37. J. Nag and R. Haglund Jr, *J. Phys.-Condens. Mat.*, 2008, **20**, 264016.

38. R. Kiruthiga, C. Nithya and R. Karvembu, *Electrochim. Acta*, 2017, **256**, 221-231.

39. Y. Wu, G. Gao, H. Yang, W. Bi, X. Liang, Y. Zhang, G. Zhang and G. Wu, *J. Mater. Chem. A*, 2015, **3**, 15692-15699.

40. A. Mauger and C. Julien, *AIMS Mater. Sci.*, 2018, **5**, 349-401.

41. R. Basu, S. Ghosh, S. Bera, A. Das and S. Dhara, *Sci. Rep.*, 2019, **9**, 1-11.

42. L. Yu, Y. Yi, T. Yao, Y. Song, Y. Chen, Q. Li, Z. Xia, N. Wei, Z. Tian, B. Nie, L. Zhang, Z. Liu and J. Sun, *Nano Res.*, 2019, **12**, 331-338.

43. G. Wee, H. Soh, Y. Cheah, S. Mhaisalkar and M. Srinivasan, *J. Mater. Chem.*, 2010, **20**, 6720-6725.

44. N. Ndiaye, T. Masikhwa, B. Ngom, M. Madito, K. Oyedotun, J. Dangbegnon and N.

Manyala, *Mater. Chem. Phys*, 2018, **214**, 192-200.

45. N. Ndiaye, M. Madito, B. Ngom, T. Masikhwa, A. Mirghni and N. Manyala, *AIP Adv.*, 2019, **9**, 1-9.

46. I. Reddy, A. Sreedhar, J. Shim and J. S. Gwag, *J. Electroanal. Chem.*, 2019, **835**, 40-47.

47. S. Fleischmann, M. Zeiger, N. Jaeckel, B. Kruener, V. Lemkova, M. Widmaier and V. Presser, *J. Mater. Chem. A*, 2017, **5**, 13039-13051.

48. S. Kaipannan, K. Govindarajan, S. Sundaramoorthy and S. Marappan, *ACS Omega*, 2019, **4**, 15798-15805.

49. M. Ates, M. Yildirim, O. Kuzgun and H. Ozkan, *J. Alloy. Compd.*, 2019, **787**, 851-864.

50. S. Shuang, L. Girardi, G. Rizzi, A. Sartorel, C. Marega, Z. Zhang and G. Granozzi, *Nanomaterials*, 2018, **8**, 544.

51. Y. Zhang, J. Zheng, T. Hu, F. Tian and C. Meng, *Appl. Surf. Sci.*, 2016, **371**, 189-195.

52. J. Wang, X. Zhang, Y. Zhang, A. Abas, X. Zhao, Z. Yang, Q. Su, W. Lan and E. Xie, *RSC Adv.*, 2017, **7**, 35558-35564.

53. W. Lv, C. Yang, G. Meng, R. Zhao, A. Han, R. Wang and J. Liu, *Sci. Rep.*, 2019, **9**, 1-8.

54. G. Ren, R. Zhang and Z. Fan, *Appl. Surf. Sci.*, 2018, **441**, 466-473.

55. X. Xia, D. Chao, C. Ng, J. Lin, Z. Fan, H. Zhang, Z. Shen and H. Fan, *Mater. Horiz.*, 2015, **2**, 237-244.

56. Y. Fan, D. Ouyang, B. Li, F. Dang and Z. Ren, *Nanoscale Res. Lett.*, 2018, **13**, 1-8.

57. X. Pan, Y. Zhao, G. Ren and Z. Fan, *Chem. Commun.*, 2013, **49**, 3943-3945.

58. M. Yu, Y. Zeng, Y. Han, X. Cheng, W. Zhao, C. Liang, Y. Tong, H. Tang and X. Lu, *Adv. Funct. Mater.*, 2015, **25**, 3534-3540.

59. G. Wang, X. Lu, Y. Ling, T. Zhai, H. Wang, Y. Tong and Y. Li, *ACS Nano*, 2012, **6**,

10296-10302.

60. X. Li, J. Fu, Z. Pan, J. Su, J. Xu, B. Gao, X. Peng, L. Wang, X. Zhang and P. Chu, *J. Power Sources*, 2016, **331**, 58-66.

61. X. Liu, R. Liu, L. Zeng, X. Huang, X. Chen, C. Zheng, Y. Xu, Q. Qian, M. Wei and Q. Chen, *New J. Chem.*, 2017, **41**, 5380-5386.

62. J. Zheng, Y. Zhang, X. Jing, X. Liu, T. Hu, T. Lv, S. Zhang and C. Meng, *Colloid. Surface. A.*, 2017, **518**, 188-196.

63. X. Zhang, Z. Bu, R. Xu, B. Xie and H. Li, *Funct. Mater. Lett.*, 2017, **10**, 1750077.

64. J. Zheng, Y. Zhang, C. Meng, X. Wang, C. Liu, M. Bo, X. Pei, Y. Wei, T. Lv and G. Cao, *Electrochim. Acta*, 2019, **318**, 635-643.

65. Z. Hou, Z. Wang, L. Yang and Z. Yang, *RSC Adv.*, 2017, **7**, 25732-25739.

66. B. Saravanakumar, K. Purushothaman and G. Muralidharan, *ACS Appl. Mater. Inter.*, 2012, **4**, 4484-4490.

67. J. Yang, T. Lan, J. Liu, Y. Song and M. Wei, *Electrochim. Acta*, 2013, **105**, 489-495.

68. A. Qian, K. Zhuo, M. Shin, W. Chun, B. Choi and C. Chung, *ChemSusChem*, 2015, **8**, 2399-2406.

69. Y. Liu, M. Clark, Q. Zhang, D. Yu, D. Liu, J. Liu and G. Cao, *Adv. Energy Mater.*, 2011, **1**, 194-202.

70. M. Deng, L. Yeh, Y. Lin, J. Chen and T. Chou, *ACS Appl. Mater. Inter.*, 2019, **11**, 29838-29848.

71. B. Pandit, D. Dubal and B. Sankapal, *Electrochim. Acta*, 2017, **242**, 382-389.

72. Y. Shao, M. El-Kady, J. Sun, Y. Li, Q. Zhang, M. Zhu, H. Wang, B. Dunn and R. Kaner, *Chem. Rev.*, 2018, **118**, 9233-9280.

73. N. Choudhary, C. Li, J. Moore, N. Nagaiah, L. Zhai, Y. Jung and J. Thomas, *Adv. Mater.*, 2017, **29**, 1605336.

74. Z. Liu, H. Zhang, Q. Yang and Y. Chen, *Electrochim. Acta*, 2018, **287**, 149-157.

75. A. Choudhury, J. Bonso, M. Wunch, K. Yang, J. Ferraris and D. Yang, *J. Power Sources*, 2015, **287**, 283-290.

76. L. Yao, C. Zhang, N. Hu, L. Zhang, Z. Zhou and Y. Zhang, *Electrochim. Acta*, 2019, **295**, 14-21.

77. D. Nagaraju, Q. Wang, P. Beaujuge and H. Alshareef, *J. Mater. Chem. A*, 2014, **2**, 17146-17152.

78. G. Yilmaz, X. Lu and G. Ho, *Nanoscale*, 2017, **9**, 802-811.

79. H. Ghaly, A. El-Deen, E. Souaya and N. Allam, *Electrochim. Acta*, 2019, **310**, 58-69.

80. C. Foo, A. Sumboja, D. Tan, J. Wang and P. Lee, *Adv. Energy Mater.*, 2014, **4**, 1400236.

81. S. Balasubramanian and K. Purushothaman, *Electrochim. Acta*, 2015, **186**, 285-291.

82. C. Zhu, D. Hu and Z. Liu, *Electrochim. Acta*, 2017, **229**, 155-165.

83. M. Tian, R. Li, C. Liu, D. Long and G. Cao, *ACS Appl. Mater. Inter.*, 2019, **11**, 15573-15580.

84. Z. Chen, V. Augustyn, J. Wen, Y. Zhang, M. Shen, B. Dunn and Y. Lu, *Adv. Mater.*, 2011, **23**, 791-795.

85. B. Kim, C. Kim, K. Yang, A. Rahy and D. Yang, *Electrochim. Acta*, 2012, **83**, 335-340.

86. I. Shakir, Z. Ali, J. Bae, J. Park and D. Kang, *Nanoscale*, 2014, **6**, 4125-4130.

87. D. Kim, J. Yun, G. Lee and J. Ha, *Nanoscale*, 2014, **6**, 12034-12041.

88. W. Sun, G. Gao, K. Zhang, Y. Liu and G. Wu, *Carbon*, 2018, **132**, 667-677.

89. W. Sun, G. Gao, Y. Du, K. Zhang and G. Wu, *J. Mater. Chem. A*, 2018, **6**, 9938-9947.

90. T. Qian, N. Xu, J. Zhou, T. Yang, X. Liu, X. Shen, J. Liang and C. Yan, *J. Mater. Chem. A*, 2015, **3**, 488-493.

91. J. Wang, H. Liu, H. Liu, W. Hua and M. Shao, *ACS Appl. Mater. Inter.*, 2018, **10**, 18816-18823.

92. W. Bi, J. Huang, M. Wang, E. Jahrman, G. Seidler, J. Wang, Y. Wu, G. Gao, G. Wu and G. Cao, *J. Mater. Chem. A*, 2019, **7**, 17966-17973.

93. M. Zhi, C. Xiang, J. Li, M. Li and N. Wu, *Nanoscale*, 2013, **5**, 72-88.

94. A. Lo, Y. Jheng, T. Huang and C. Tseng, *Applied energy*, 2015, **153**, 15-21.

95. Y. Huang, Y. Li, Z. Hu, G. Wei, J. Guo and J. Liu, *J. Mater. Chem. A*, 2013, **1**, 9809-9813.

96. Y. Zhang, Y. Zhao, S. Cao, Z. Yin, L. Cheng and L. Wu, *ACS Appl. Mater. Inter.*, 2017, **9**, 29982-29991.

97. T. Sun, Z. Li, X. Liu, L. Ma, J. Wang and S. Yang, *J. Power Sources*, 2017, **352**, 135-142.

98. J. Xu, F. Zheng, C. Xi, Y. Yu, L. Chen, W. Yang, P. Hu, Q. Zhen and S. Bashir, *J. Power Sources*, 2018, **404**, 47-55.

99. Y. Yang, D. Kim, M. Yang and P. Schmuki, *Chem. Commun.*, 2011, **47**, 7746-7748.

100. G. Nie, X. Lu, J. Lei, Z. Jiang and C. Wang, *J. Mater. Chem. A*, 2014, **2**, 15495-15501.

101. X. Wang, B. Shi, X. Wang, J. Gao, C. Zhang, Z. Yang and H. Xie, *J. Mater. Chem. A*, 2017, **5**, 23543-23549.

102. X. Zhong, L. Zhang, J. Tang, J. Chai, J. Xu, L. Cao, M. Yang, M. Yang, W. Kong and S. Wang, *J. Mater. Chem. A*, 2017, **5**, 17954-17962.

103. R. Manikandan, C. Raj, M. Rajesh, B. Kim, S. Park, B. Cho and K. Yu, *Electrochim. Acta*, 2017, **230**, 492-500.

104. M. Jayalakshmi, M. Rao, N. Venugopal and K. Kim, *J. Power Sources*, 2007, **166**, 578-583.

105. C. Guo, G. Yilmaz, S. Chen, S. Chen and X. Lu, *Nano Energy*, 2015, **12**, 76-87.

106. A. Glushenkov, D. Hulicova-Jurcakova, D. Llewellyn, G. Lu and Y. Chen, *Chem. Mater.*, 2010, **22**, 914-921.

107. A. Djire, P. Pande, A. Deb, J. Siegel, O. Ajenifujah, L. He, A. Sleightholme, P. Rasmussen and L. Thompson, *Nano Energy*, 2019, **60**, 72-81.

108. D. Zhang, J. Li, Z. Su, S. Hu, H. Li and Y. Yan, *J. Adv. Ceram.*, 2018, **7**, 246-255.

109. F. Ran, Z. Wang, Y. Yang, Z. Liu, L. Kong and L. Kang, *Electrochim. Acta*, 2017, **258**, 405-413.

110. W. Zhang, Y. Yang, M. Ravi, L. Kong, L. Kang and F. Ran, *Electrochim. Acta*, 2019, **306**, 113-121.

111. Q. Li, Y. Chen, J. Zhang, W. Tian, L. Wang, Z. Ren, X. Ren, X. Li, B. Gao, X. Peng, P. Chu and K. Huo, *Nano Energy*, 2018, **51**, 128-136.

112. N. Ouldhamadouche, A. Achour, R. Lucio-Porto, M. Islam, S. Solaymani, A. Arman, A. Ahmadpourian, H. Achour, L. Le Brizoual, M. Djouadi and T. Brousse, *J. Mater. Sci. Technol.*, 2018, **34**, 976-982.

113. J. Zhao, C. Li, Q. Zhang, J. Zhang, X. Wang, Z. Lin, J. Wang, W. Lv, C. Lu, C. Wong and Y. Yao, *J. Mater. Chem. A*, 2017, **5**, 6928-6936.

114. Y. Su and I. Zhitomirsky, *J. Power Sources*, 2014, **267**, 235-242.

115. C. Ghimbeu, E. Raymundo-Pinero, P. Fioux, F. Beguin and C. Vix-Guterl, *J. Mater. Chem.*, 2011, **21**, 13268-13275.

116. G. An, D. Lee and H. Ahn, *J. Mater. Chem. A*, 2017, **5**, 19714-19720.

117. Q. Zhang, X. Wang, Z. Pan, J. Sun, J. Zhao, J. Zhang, C. Zhang, L. Tang, J. Luo, B. Song, Z. Zhang, W. Lu, Q. Li, Y. Zhang and Y. Yao, *Nano Lett.*, 2017, **17**, 2719-2726.

118. X. Jiang, W. Lu, Y. Li, Y. Yu, X. Zhou, X. Liu and Y. Xing, *ChemElectroChem*, 2019, **6**, 3445-3453.

119. T. He, Z. Wang, X. Li, Y. Tan, Y. Liu, L. Kong, L. Kang, C. Chen and F. Ran, *J. Alloy. Compd.*, 2019, **781**, 1054-1058.

120. J. Liu, F. Li, W. Liu and X. Li, *Inorg. Chem. Front.*, 2019, **6**, 164-171.

121. J. Balamurugan, G. Karthikeyan, T. Tran Duy, N. Kim and J. Lee, *J. Power Sources*, 2016, **308**, 149-157.

122. C. Ji, J. Bi, S. Wang, X. Zhanga and S. Yang, *J. Mater. Chem. A*, 2016, **4**, 2158-2168.

123. X. Jiang, W. Lu, Y. Yu, M. Yang, X. Liu and Y. Xing, *Electrochim. Acta*, 2019, **302**, 385-393.

124. X. Zhou, C. Shang, L. Gu, S. Dong, X. Chen, P. Han, L. Li, J. Yao, Z. Liu, H. Xu, Y. Zhu and G. Cui, *ACS Appl. Mater. Inter.*, 2011, **3**, 3058-3063.

125. B. Wei, C. Shang, L. Shui, X. Wang and G. Zhou, *Mater. Res. Express*, 2019, **6**, 025801.

126. B. Pandit, L. Bommineedi and B. Sankapal, *J. Energy Chem.*, 2019, **31**, 79-88.

127. J. Feng, X. Sun, C. Wu, L. Peng, C. Lin, S. Hu, J. Yang and Y. Xie, *J. Am. Chem. Soc.*, 2011, **133**, 17832-17838.

128. Z. Guo, L. Yang, W. Wang, L. Cao and B. Dong, *J. Mater. Chem. A*, 2018, **6**, 14681-14688.

129. P. Zhang, L. Wang, F. Wang, D. Tan, G. Wang, S. Yang, M. Yu, J. Zhang and X. Feng, *Batteries & Supercaps*, 2019, **2**, 918-923.

130. L. Fang, Z. Zhang, X. Li, H. Zhou, K. Ma, L. Ge and K. Huang, *Colloid. Surface. A.*, 2016, **501**, 42-48.

131. X. Wang, Y. Zhang, J. Zheng, X. Liu and C. Meng, *J. Colloid. Interf. Sci.*, 2019, **554**, 191-201.

132. S. Ratha, S. Marri, N. Lanzillo, S. Moshkalev, S. Nayak, J. Behera and C. Rout, *J. Mater. Chem. A*, 2015, **3**, 18874-18881.

133. S. Ratha, S. Marri, J. Behera and C. Rout, *Eur. J. Inorg. Chem.*, 2016, 259-265.

134. M. Ramu, J. Chellan, N. Goli, P. Joaquim, V. Cristobal and B. Kim, *Adv. Funct. Mater.*, 2020, **30**, 1906586.

135. S. Wang, Y. Song, Y. Ma, Z. Zhu, C. Zhao and C. Zhao, *Chem. Eng. J.*, 2019, **365**, 88-98.

136. H. Sun, X. Chen, H. Chai, Y. Wang, D. Jia, Y. Cao and A. Liu, *Appl. Surf. Sci.*, 2019, **469**, 118-124.

137. Y. Teng, Y. Li, D. Yu, Y. Meng, Y. Wu, X. Zhao and X. Liu, *ChemistrySelect*, 2019, **4**, 956-962.

138. M. Liu, L. Kong, L. Kang, X. Li, F. Walsh, M. Xing, C. Lu, X. Ma and Y. Luo, *J. Mater. Chem. A*, 2014, **2**, 4919-4926.

139. W. Zhang, L. Kong, X. Ma, Y. Luo and L. Kang, *J. Power Sources*, 2014, **269**, 61-68.

140. M. Guo, J. Balamurugan, N. Kim and J. Lee, *Appl. Catal. B-Environ.*, 2018, **239**, 290-299.

141. R. Kumar, P. Rai and A. Sharma, *J. Mater. Chem. A*, 2016, **4**, 9822-9831.

142. R. Kumar, T. Bhuvana, P. Rai and A. Sharma, *J. Electrochem. Soc.*, 2018, **165**, B1-B8.

143. X. Liu, J. Wang and G. Yang, *ACS Appl. Mater. Inter.*, 2018, **10**, 20688-20695.

144. P. Vishnukumar, B. Saravanakumar, G. Ravi, V. Ganesh, R. Guduru and R. Yuvakkumar, *Mater. Lett.*, 2018, **219**, 114-118.

145. S. Zhao, K. Tao and Y. Gong, *Dalton T.*, 2019, **48**, 5315-5326.

146. H. Hosseini and S. Shahrokhian, *Chem. Eng. J.*, 2018, **341**, 10-26.

147. L. Pei, N. Lin, T. Wei, H. Liu and H. Yu, *J. Alloy. Compd.*, 2015, **631**, 90-98.

148. F. Butt, C. Cao, F. Idrees, M. Tahir, R. Hussain, R. Ahmed and W. Khan, *Int. J. Hydrogen*

Energy, 2015, **40**, 9359-9364.

149. S. Pitale, M. Gohain, I. Nagpure, O. Ntwaeaborwa, B. Bezuidenhoudt and H. Swart, *Physica B.*, 2012, **407**, 1485-1488.

150. S. Ni, S. Lin, Q. Pan, K. Huang, F. Yang and D. He, *J. Alloy. Compd.*, 2009, **477**, L1-L3.

151. Y. Li, Y. Teng, Z. Zhang, Y. Feng, P. Xue, W. Tong and X. Liu, *New J. Chem.*, 2017, **41**, 15298-15304.

152. W. Low, P. Khiew, S. Lim, C. Siong, C. Chia and E. Ezeigwe, *J. Alloy. Compd.*, 2019, **784**, 847-858.

153. R. Packiaraj, P. Devendran, S. Bahadur and N. Nallamuthu, *J. Mater. Sci.-Mater. El.*, 2018, **29**, 13265-13276.

154. L. Deng, J. Liu, Z. Ma, G. Fan and Z. Liu, *RSC Adv.*, 2018, **8**, 24796-24804.

155. S. Patil, D. Dubal, V. Deonikar, M. Tamboli, J. Ambekar, P. Gomez-Romero, S. Kolekar, B. Kale and D. Patil, *ACS Appl. Mater. Inter.*, 2016, **8**, 31602-31610.

156. Y. Yan, H. Xu, W. Guo, Q. Huang, M. Zheng, H. Pang and H. Xue, *Inorg. Chem. Front.*, 2016, **3**, 791-797.

157. F. Yu, T. Huang, P. Zhang, Y. Tao, F. Cui, Q. Xie, S. Yao and F. Wang, *Energy Storage Mater.*, 2019, **22**, 235-255.

158. F. Wang, Z. Liu, X. Yuan, J. Mo, C. Li, L. Fu, Y. Zhu, X. Wu and Y. Wu, *J. Mater. Chem. A*, 2017, **5**, 14922-14929.

159. D. Zhao, Q. Zhu, D. Chen, X. Li, Y. Yu and X. Huang, *J. Mater. Chem. A*, 2018, **6**, 16475-16484.

160. H. Zeng, Y. Zhao, Y. Hao, Q. Lai, J. Huang and X. Ji, *J. Alloy. Compd.*, 2009, **477**, 800-804.

161. T. Zhai, X. Lu, Y. Ling, M. Yu, G. Wang, T. Liu, C. Liang, Y. Tong and Y. Li, *Adv. Mater.*, 2014, **26**, 5869-5875.

162. Z. Luo, E. Liu, T. Hu, Z. Li and T. Liu, *Ionics*, 2015, **21**, 289-294.

163. N. Chen, J. Zhou, Q. Kang, H. Ji, G. Zhu, Y. Zhang, S. Chen, J. Chen, X. Feng and W. Hou, *J. Power Sources*, 2017, **344**, 185-194.

164. C. Wu, X. Lu, L. Peng, K. Xu, X. Peng, J. Huang, G. Yu and Y. Xie, *Nat. Commun.*, 2013, **4**, 1-7.

165. Y. He, X. Yang, Y. Bai, J. Zhang, L. Kang, Z. Lei and Z. Liu, *Electrochim. Acta*, 2015, **178**, 312-320.

166. N. Chen, J. Zhou, G. Zhu, Q. Kang, H. Ji, Y. Zhang, X. Wang, L. Peng, X. Guo, C. Lu, J. Chen, X. Feng and W. Hou, *Nanoscale*, 2018, **10**, 3709-3719.

167. Y. Dall'Agnese, P. Taberna, Y. Gogotsi and P. Simon, *J. Phys. Chem. Lett.*, 2015, **6**, 2305-2309.

Figure captions

Fig. 1. (a) The monoclinic insulator in the VO_2 crystal structure. (b) The rutile metal. (c) Common crystal structures in VN compounds. (d) The crystal structures of $V_2O_5{\cdot}H_2O$. (e) V_2O_5. (f) V_2O_3. (g) VS_2. (h) Schematic illustration of the chain-like structure of VS_4. (i) The schematic illustration for sodium storage mechanisms of VO_2(B). (a and b) Reprinted with permission.[16] Copyright 2015, Elsevier. (c) Reprinted with permission.[24] Copyright 2016, Wiley-VCH. (d, e, f and i) Reprinted with permission.[25] Copyright 2020, Wiley-VCH. (g) Reprinted with permission.[26] Copyright 2012, Nature Publishing Group. (h) Reprinted with permission.[27] Copyright 2013, American Chemical Society.

Fig. 2 (a) Schematic of the preparation of the VO_2 nanosheet electrode with the CMC binder on graphitized carbon paper. (b) Scanning electron micrograph of VO_2 nanoporous structure grown on carbon paper. (c) Bare CF. (d) Nyquist plots of VO_2 thin films. (e) The specific capacitance vs. cycle number at a constant scan rate of 100 $mV{\cdot}s^{-1}$. (f) Schematic illustration of the fabrication process of GF supported VO_2/HMB. (g) EIS spectra of 2D VO_2 microarrays. (h) The schematic diagram of preparation process for VO_2 NF@3DG hybrid. (i) Illustration of the formation process of 2D VO_2 mesoporous microarrays. (a) Reprinted with permission.[31] Copyright 2016, Elsevier. (b and c) Reprinted with permission.[41](d and e) Reprinted with permission.[46] Copyright 2019, Elsevier. (f) Reprinted with permission.[55] Copyright 2015, The Royal Society of Chemistry. (g and i) Reprinted with permission.[56] Copyright 2017, Nano Express. (h) Reprinted with permission.[52] Copyright 2017, The Royal Society of Chemistry.

Fig. 3 (a) Schematic illustration of encapsulating V_2O_3 nanorods into carbon core-shell structured composites. (b) Schematic illustration for the fabrication of porous V_2O_5/U-paper and 3D network V_2O_5/Pt/U-paper electrode. (c) A schematic illustration of the synthesis of V_2O_3@C core-shell structured composites. (d) A schematic illustration of the synthesis of highly dispersed VO-C. (e) The SEM of 3D network V_2O_5/Pt/U-paper. (f) Schematic of the fabrication of the flexible and self-supported V_2O_3/N-rGO film electrodes and the assembly of the all-solid-state flexible SCs devices. (g) Schematic representation of the fabricated FASC device based on V_2O_5 electrode with PVA-$LiClO_4$ gel electrolyte. (h) Capacitance retention for altered bending angles, inset displays CVs with various bending angles at 20 $mV·s^{-1}$ scan rate. (a) Reprinted with permission.[33]. Copyright 2017, Elsevier. (b and e) Reprinted with permission.[70] Copyright 2019, American Chemical Society. (c) Reprinted with permission.[62] Copyright 2017, Elsevier. (d) Reprinted with permission.[64] Copyright 2019, Elsevier. (f) Reprinted with permission.[65] Copyright 2017, The Royal Society of Chemistry. (g and h) Reprinted with permission.[71] Copyright 2017, Elsevier.

Fig. 4 (a) HGO and rGO/V_2O_5 synthesis diagram. (b) The schematic illustration for the synthetic process of rGO/V_2O_5 hybrid aerogels. (c) Schematic illustration of the assembly process. (d) Cyclic voltammograms of asymmetric device at its flat and bent state at 25 $mV·s^{-1}$, inset shows the device testing in the flat state. (e) FESEM images of carbon coated flowery V_2O_5. (f) SAED pattern of carbon coated flowery V_2O_5. (a) Reprinted with permission.[74] Copyright 2018, Elsevier. (b) Reprinted with permission.[76] Copyright 2018, Elsevier. (c) Reprinted with permission.[78] Copyright 2017, The Royal Society of Chemistry. (d) Reprinted with permission.[80] Copyright 2014, Wiley-VCH. (e and f) Reprinted with permission.[81]. Copyright 2015, Elsevier.

Fig. 5 (a) Schematic illustration of the preparation route of the HPVC. (b) Synthesis of MCM/V_2O_5 composites with a spray drying process for MCM preparation and followed by a wet-impregnation process to obtain composites. (c) Illustration of the mixed growth and self-assembly methodology for controlled synthesis of 3D V_2O_5/MWCNT core/shell hybrid aerogels. (d) EIS spectra of raw V_2O_5 powder, V_2O_5 aerogel, V_2O_5/MWCNT hybrid aerogels and MWCNTs. (e) Schematic illustration of the fabrication process of the LBL of ultrathin V_2O_5 anchored MWCNTs and graphene on Ni/Cu/Ni/Au coated textile fiber fabric for flexible SC applications. (f) Charge-discharge curve of MSC arrays where four MSC arrays are connected in parallel (4P) with the periodic irradiation of 254 nm UV light onto the integrated SnO_2 NW UV sensor during discharge (blue). The duration and period of UV pulse are both 5 s. For comparison, the self-discharge curve without the periodic irradiation of UV is shown (orange). (a) Reprinted with permission.[82] Copyright 2017, Elsevier. (b) Reprinted with permission.[83] Copyright 2019, American Chemical Society. (c and d) Reprinted with permission.[39] Copyright 2015, The Royal Society of Chemistry. (e) Reprinted with permission.[86] Copyright 2014, The Royal Society of Chemistry. (f) Reprinted with permission.[87] Copyright 2014, The Royal Society of Chemistry.

Fig. 6 (a) Schematic model of N-containing surface functional groups on N-CNFs. (b) Schematic illustration of the fabrication process and structure of the N-CNF/V_2O_5- aerogels. (c) SEM images and photographs of the N-GA@V_2O_5 NWAs. (d) Schematic illustration of the enhanced ionic transfer kinetics around Vö by the formation of a E. (e) Schematic illustration of the in situ interfacial synthesis process of V_2O_5@PPy NW membrane. (f) Nyquist plots of experimental impedance and their equivalent circuit analysis. (g) Cycle stability measurement at the current density of 0.5 $A \cdot g^{-1}$ and the initial profiles for the first four charge-discharge cycles, charge-discharge profiles after 6000 cycles, triangular shapes of the first and 12000th cycle, respectively. (h) Cycling performance of Vö-V_2O_5/CPs and V_2O_5-NFs at 10 $A \cdot g^{-1}$. (a, b, f and g) Reprinted with permission.[88] Copyright 2018, Elsevier. (c) Reprinted with permission.[89] Copyright 2018, The Royal Society of Chemistry. (d and h) Reprinted with permission.[92] Copyright 2019, The Royal Society of Chemistry. (e) Reprinted with permission.[91] Copyright 2018, American Chemical Society.

Fig. 7 (a) Crystal structure and Charge-discharge process of hierarchical VNBs/TNFs heterojunction composite. (b) Scheme and digital images showing the fabrication of LVO aerogel, LVO\PEDOT, and LVO\PEDOT\LMO. (c) Diagram of the charge transport in the V_2O_5/Ni_3S_2 nanoflake nanostructures. (d) Schematic illustration of the two-step method for the synthesis of the hierarchical $V_2O_5@Ni_3S_2$ nanomaterials. (e) FESEM images of hierarchical VNBs/TNFs heterojunction composite. (f) SEM images of the V_2O_5 nanorods. (g) SEM images of the resulting porous nanorods of VN. (h) Configuration of the ASCs. (i) Bode plots for the V1, V2 and V3 electrodes (inset shows the equivalent circuit of fit). (j) CV curves of the VN NW electrode collected at various scan rates. (k) Cycling performance of single VN electrode and symmetric VN SC devices collected at a scan rate of 100 $mV \cdot s^{-1}$ for 10 000 cycles in 5 M LiCl aqueous electrolyte and LiCl/PVA gel electrolyte. (a and e) Reprinted with permission.[98] Copyright 2018, Elsevier. (b and h) Reprinted with permission.[105] Copyright 2014, Elsevier. (c) Reprinted with permission.[101] Copyright 2014, The Royal Society of Chemistry. (d) Reprinted with permission.[102] Copyright 2017, The Royal Society of Chemistry. (f and g) Reprinted with permission.[106] Copyright 2009, American Chemical Society. (i) Reprinted with permission.[103] Copyright 2017, Elsevier. (j and k) Reprinted with permission.[34] Copyright 2013, American Chemical Society.

Fig. 8 (a) Schematic illustration of the preparation procedures of the VNNDs/CNSs from PANI intercalated $V_2O_5 \cdot 1.6H_2O$ organic-inorganic hybrid nanosheets. (b) A schematic of the process used to fabricate the porous VN NWs on the CNTF substrate. (c) Schematic illustration for adsorption of vanadate ions and preparation of electrode materials for SCs. (d) The normalized areal capacitance versus scan rate of VN/CNTs with different thicknesses of VN coating. (e) The cycling stability (black ball-line) and coulombic efficiency (blue ball-line) of the $ZnCo_2O_4$/VN ASC device over 4000 cycles; the inset shows the CV curves obtained at different cycle numbers at the scan rate of

100 mV·s^{-1}. (f) The Ragone plot (power density vs. energy density) of the assembled ASC device. (a) Reprinted with permission.[111] Copyright 2018, Elsevier. (b, e and f) Reprinted with permission.[112] Copyright 2017, Elsevier. (c) Reprinted with permission.[110] Copyright 2019, Elsevier. (d) Reprinted with permission.[113] Copyright 2017, The Royal Society of Chemistry.

Fig. 9 (a) Schematic illustration for VNNP@GO fabrication strategy. (b) Illustration of electrochemical reactions for a commercial VN. (c) VN/CF. (d) Cycling stability at different current densities of 4, 40, and 80 A·g^{-1} (2700, 27 000, and 54 000 W·kg^{-1}) over 10 000 cycles. (e) Schematic illustrations of the fabrication of the ACFSS. (f) The cross-sectional structure of the ACFSS. (g) Wrapping of an aligned CNT sheet around a modified CNT fiber. (h) Schematic illustration of the synthesis procedures for as-spun fibre, stabilized fibre, and VN/CF. (a) Reprinted with permission.[119]. Copyright 2018, Elsevier. (b, c, d and h) Reprinted with permission.[116] Copyright 2017, The Royal Society of Chemistry. (e, f and g) Reprinted with permission.[117] Copyright 2017, American Chemical Society.

Fig. 10 (a) Schematic illustration for the preparation of VN/N-G nanocomposites. (b) Schematic for the synthesis of the $Ni_{1-x}V_xO_2$ hierarchical hollow microspheres and the subsequent nitridation process. (c) Schematic illustration for the fabrication of VN/NG composite. (d) HR-TEM images of VN/NG composite. (e) FESEM morphology of Ti_2V_1-HMs. (f) TEM of Ti_2V_1-HMs. (a) Reprinted with permission.[120] Copyright 2019, The Partner Organisations. (b) Reprinted with permission.[122] Copyright 2016, The Royal Society of Chemistry. (c and d) Reprinted with permission.[121] Copyright 2016, Elsevier. (e and f) Reprinted with permission.[125] Copyright 2018, IOP.

Fig. 11 (a) The synthesis illustration of $NiCo_2S_4$@VS_2. (b) Schematic illustration for the chemical synthesis of VS_2 by SILAR method. (c) The VS_2 precursor with NH_3 molecules intercalated into the S-V-S layers. (d) Effusion of NH_3 molecules away from the stacked layers, breaking down the c axis periodicity and resulting in the formation of ultrathin VS_2 nanosheets. (e) Vacuum-filtration assembly of the as synthesized VS_2 nanosheets into transferrable thin films on mixed cellulose membrane. (f) Schematic diagram of the formation of the ZnO/VS_2 nanoarchitecture. (g) Two asymmetric SCs were connected in series to light an OUC LED panel. (h) Schematic illustration of charge storage and transfer merits of $NiCo_2S_4@VS_2$. (a and h) Reprinted with permission.[35] Copyright 2018, Elsevier. (b) Reprinted with permission.[126] Copyright 2018, Elsevier. (c) Reprinted with permission.[127, 130] Copyright 2016, Elsevier. (d, e and f) Reprinted with permission.[115] Copyright 2011, American Chemical Society. (g) Reprinted with permission.[128] Copyright 2018, The Royal Society of Chemistry.

Fig. 12 (a) Schematic illustration of the formation processes of the 3D porous $Co_2V_2O_7·3.3H_2O$ microflowers. (b) Synthesis protocol adopted for preparation of $Ni_3(VO_4)_2$ nanosheet arrays/Ni foam electrode and electrochemical sensing mechanism. (c) Schematic illustration of the synthesis of electrode materials and the fabrication of the device. (d) CV curve of $Ni_3(VO_4)_2$ nanospheres at various scan rates. (e) Cycle test of the $Co_2V_2O_7·3.3H_2O$ microflowers at a current density of 5 $A·g^{-1}$. (f) Schematic illustration of graphene-2D $Zn_3V_2O_8$ hexagonal sheet nanocomposite via solvothermal approach. (g) Cycling performance over 10 000 GCD cycles at 10 $A·g^{-1}$. (a and e) Reprinted with permission.[136] Copyright 2018, Elsevier. (b) Reprinted with permission.[159] Copyright 2018, ECS. (c) Reprinted with permission.[143] Copyright 2018, American Chemical Society. (d) Reprinted with permission.[141] Copyright 2016, The Royal Society of Chemistry. (f) Reprinted with permission.[152]. Copyright 2019, Elsevier. (g) Reprinted with permission.[36] Copyright 2019, Elsevier.

Fig. 13 (a) Schematic illustration displaying the synthesis process of ferox fruit-like patronite nanostructures on flexible CC under the pH controlled growth medium. (b) Schematic synthesis process for nest-like V_3O_7. (c) Schematic illustration of the formation procedure of the nest-like NC-V_3O_7 nanosheets self-assembled by NWs. (d) Schematic illustration of the preparation of VS_4/CNTs composites. (e) Cycling stability of VS_4-CC@VS-3 SSC device for 1000 charge/discharge cycles at 10 $mA\cdot cm^{-2}$. (f) GCD tests of VRCS@Co. (g) Rate performance of $VOPO_4$/graphene composites. (h) Cycling performance of $VOPO_4$/graphene composites. (a and e) Reprinted with permission.[134] Copyright 2019, Wiley-VCH. (b) Reprinted with permission.[142] Copyright 2018, The Royal Society of Chemistry. (c, g and h) Reprinted with permission.[163] Copyright 2017, Elsevier. (d) Reprinted with permission.[131] Copyright 2019, Elsevier. (f) Reprinted with permission.[135] Copyright 2019, Elsevier.

Table captions

Table 1 The advantages and disadvantages of electrode materials for SCs

Table 2 The comparison of various VO_2 and its nanocomposites as electrode materials for SCs.

Table 3 The comparison of various V_2O_3/C nanocomposites as electrode materials for SCs.

Table 4 The comparison of various V_2O_5 and its nanocomposites as electrode materials for SCs.

Table 5 The comparison of various VN and its nanocomposites as electrode materials for SCs.

Table 6 The comparison of various vanadium sulfide and its nanocomposites as electrode materials for SCs.

Table 7 The comparison of other vanadium-based materials as electrode materials for SCs.

Table 8 The comparison of various mixed metal vanadates nanostructures as electrode materials for SCs.

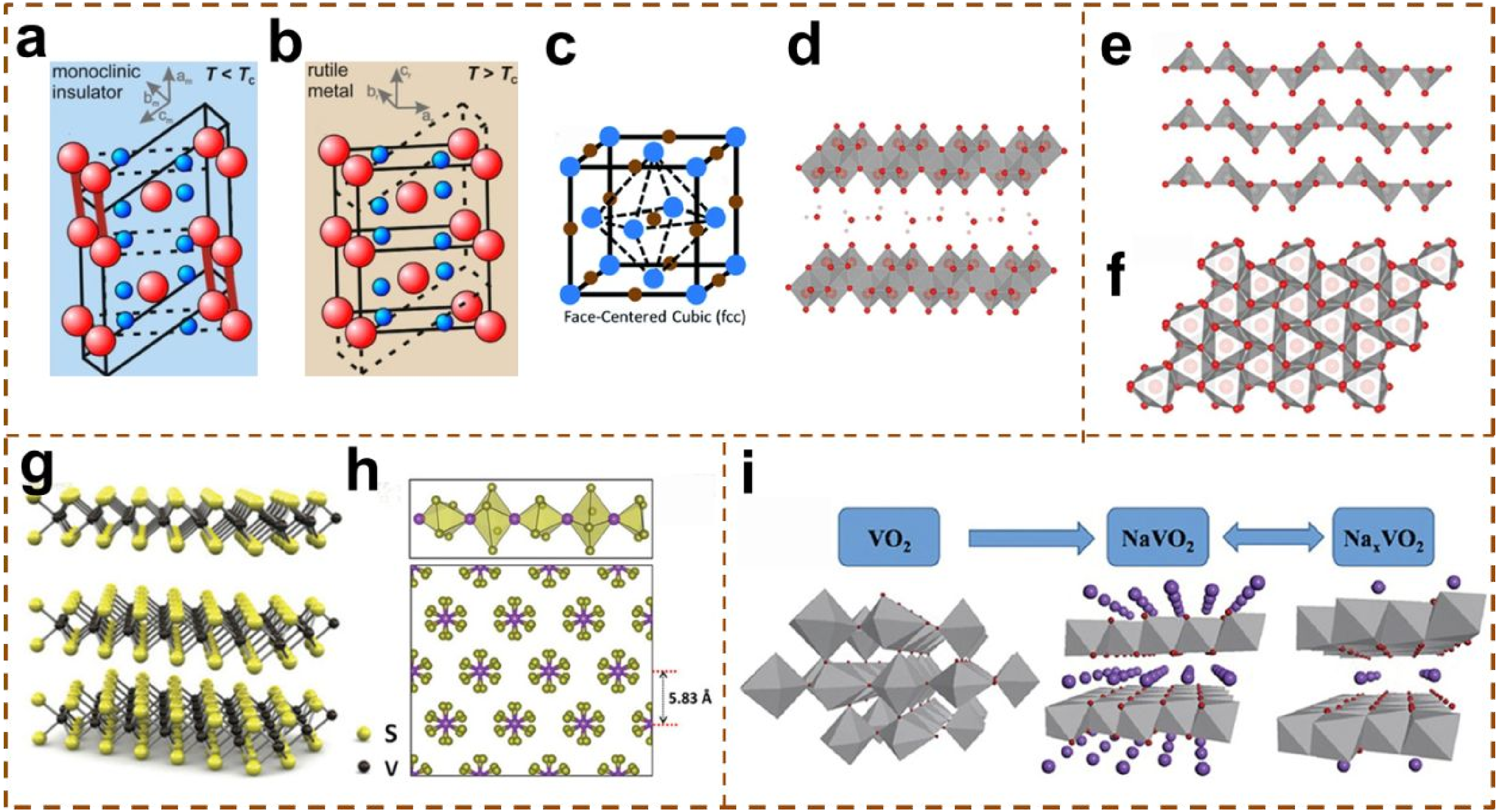
a
monoclinic insulator
a_m
b_m
c_m
$T < T_c$
b
rutile metal
c_r
b_r
a_r
$T > T_c$
c
Face-Centered Cubic (fcc)
d
e
f
g
h
5.83 Å
S
V
i
VO_2
$NaVO_2$
Na_xVO_2

Fig. 1

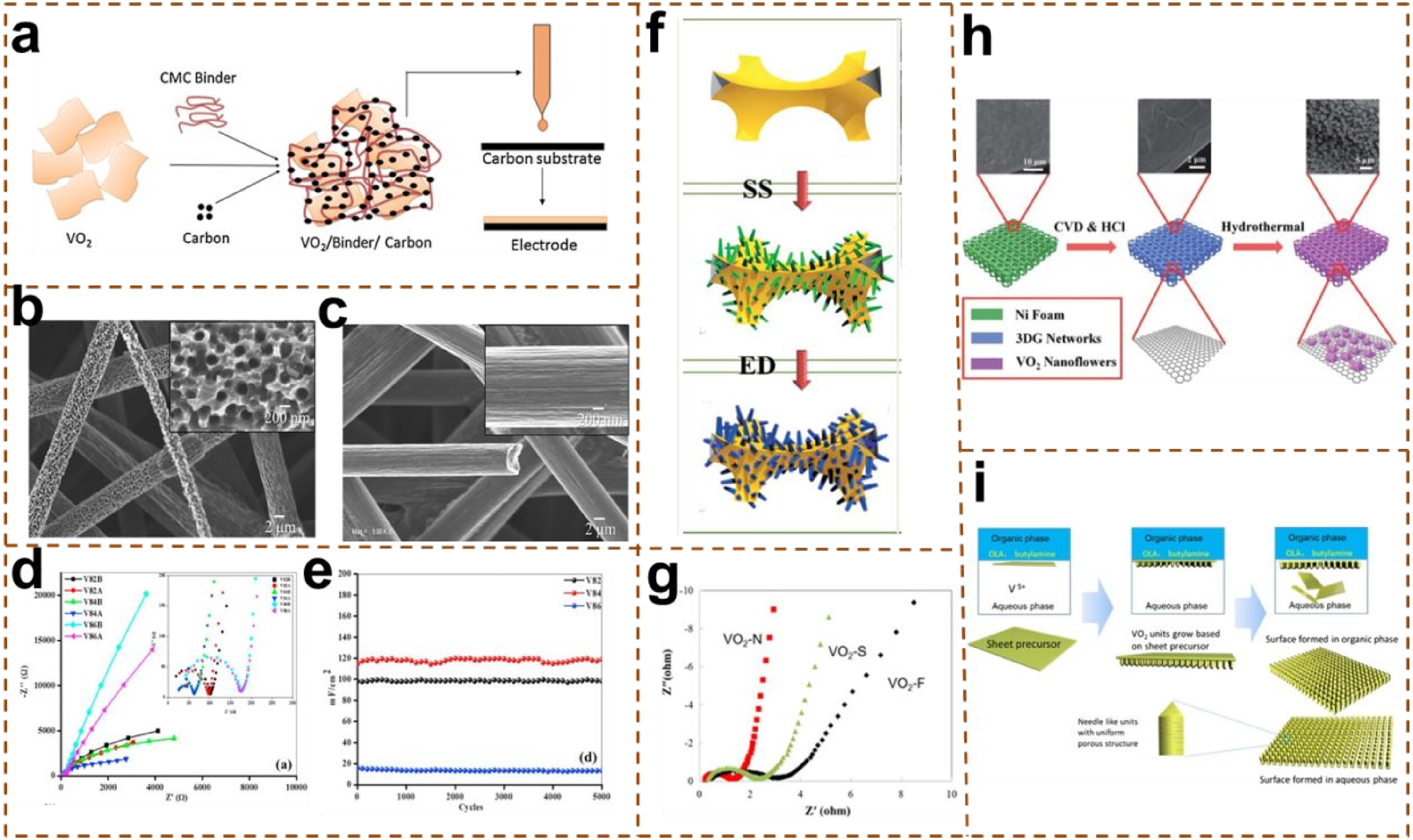
a
CMC Binder
VO2
Carbon
VO2/Binder/ Carbon
Carbon substrate
Electrode
b
200 nm
2 μm
c
200 nm
2 μm
d
V82B
V82A
V84B
V84A
V86B
V86A
-Z'' (Ω)
Z' (Ω)
0
2000
4000
6000
8000
10000
5000
15000
20000
(a)
e
V82
V84
V86
mF/cm2
Cycles
0
1000
2000
3000
4000
5000
20
40
60
80
100
120
140
160
180
200
(d)
f
SS
ED
g
VO2-N
VO2-S
VO2-F
Z''(ohm)
Z' (ohm)
0
2
4
6
8
10
-2
-4
-6
-8
-10
h
10 μm
2 μm
5 μm
CVD & HCl
Hydrothermal
Ni Foam
3DG Networks
VO2 Nanoflowers
i
Organic phase
OLA、butylamine
V5+
Aqueous phase
Sheet precursor
VO2 units grow based on sheet precursor
Surface formed in organic phase
Needle like units with uniform porous structure
Surface formed in aqueous phase

Fig. 2

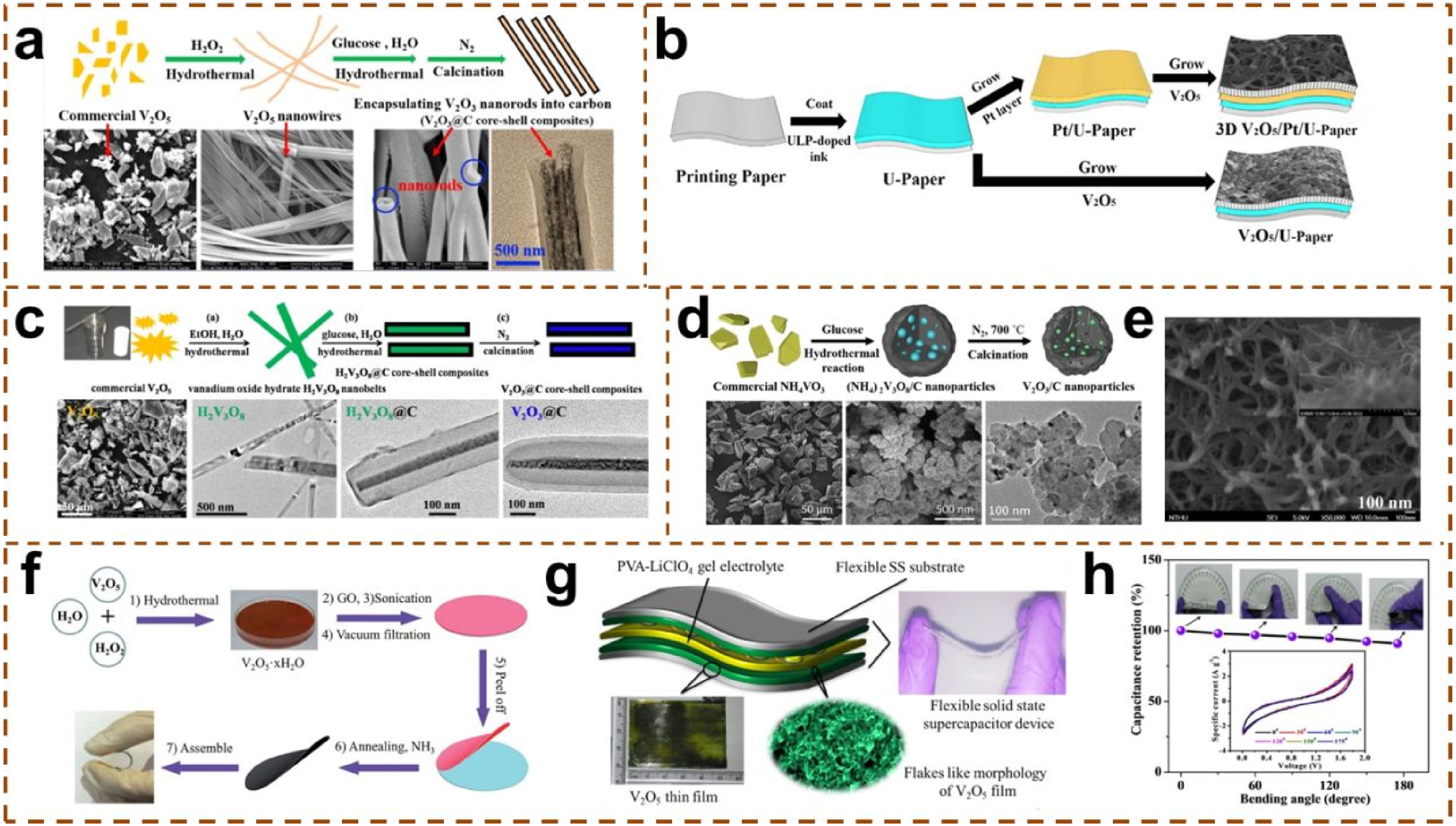
a
H₂O₂
Hydrothermal
Glucose , H₂O
Hydrothermal
N₂
Calcination
Commercial V₂O₅
V₂O₅ nanowires
Encapsulating V₂O₃ nanorods into carbon
(V₂O₃@C core-shell composites)
nanorods
500 nm
b
Printing Paper
Coat
ULP-doped ink
U-Paper
Grow Pt layer
Pt/U-Paper
Grow
V₂O₅
3D V₂O₅/Pt/U-Paper
Grow
V₂O₅
V₂O₅/U-Paper
c
(a)
EtOH, H₂O
hydrothermal
(b)
glucose, H₂O
hydrothermal
(c)
N₂
calcination
H₂V₃O₈@C core-shell composites
commercial V₂O₅
vanadium oxide hydrate H₂V₃O₈ nanobelts
V₂O₃@C core-shell composites
V₂O₅
H₂V₃O₈
H₂V₃O₈@C
V₂O₃@C
50 μm
500 nm
100 nm
100 nm
d
Glucose
Hydrothermal reaction
N₂, 700 °C
Calcination
Commercial NH₄VO₃
(NH₄)₂V₃O₈/C nanoparticles
V₂O₃/C nanoparticles
50 μm
500 nm
100 nm
e
100 nm
f
V₂O₅
H₂O
+
H₂O₂
1) Hydrothermal
V₂O₅·xH₂O
2) GO, 3)Sonication
4) Vacuum filtration
5) Peel off
6) Annealing, NH₃
7) Assemble
g
PVA-LiClO₄ gel electrolyte
Flexible SS substrate
Flexible solid state supercapacitor device
V₂O₅ thin film
Flakes like morphology of V₂O₅ film
h
Capacitance retention (%)
Bending angle (degree)
150
100
50
0
0
60
120
180
Specific current (A g⁻¹)
Voltage (V)

Fig. 3

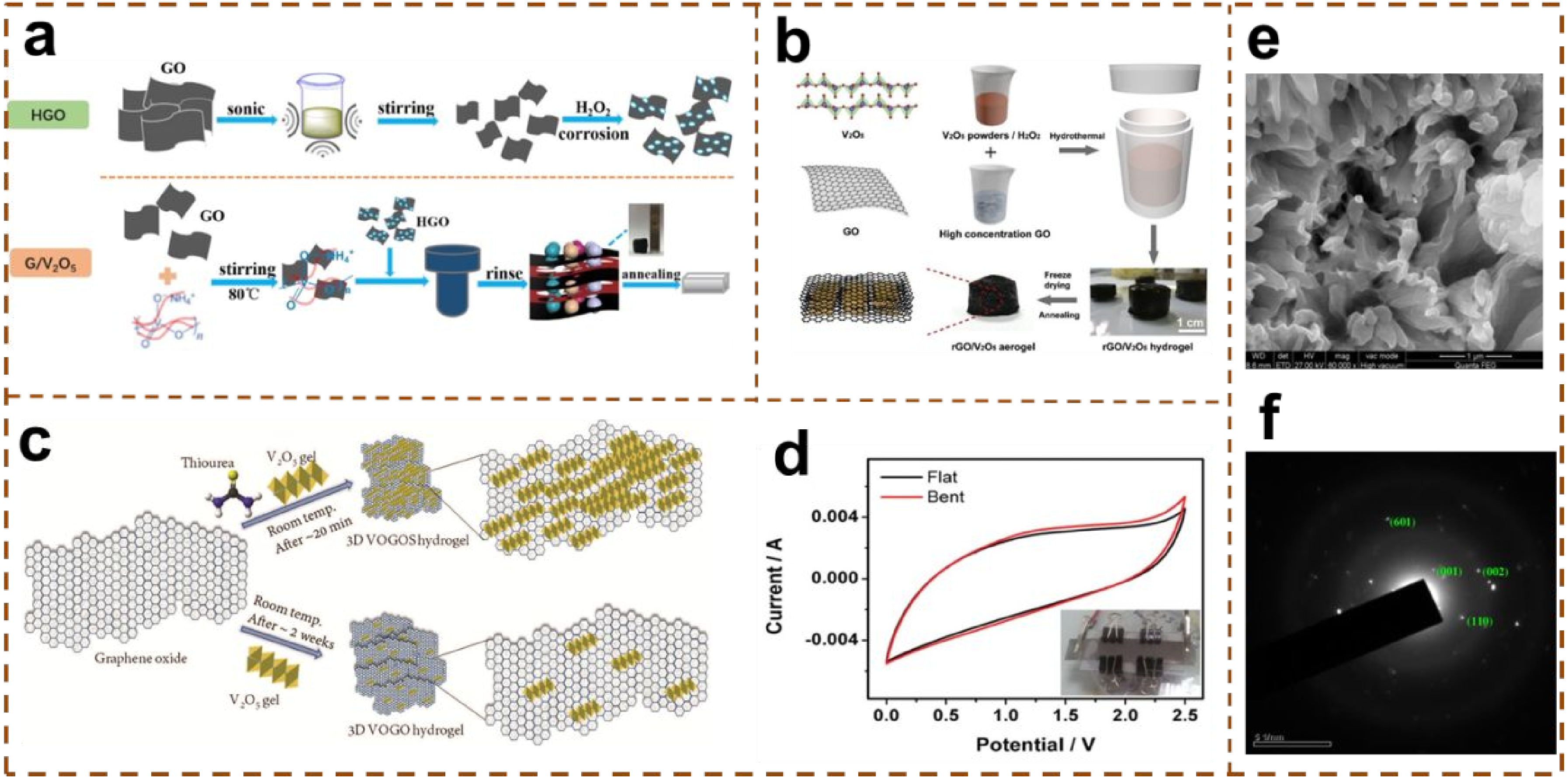
a
HGO
GO
sonic
stirring
H2O2
corrosion
G/V2O5
GO
HGO
stirring
80℃
rinse
annealing
b
V2O5
V2O5 powders / H2O2
+
Hydrothermal
GO
High concentration GO
Freeze drying
Annealing
1 cm
rGO/V2O5 aerogel
rGO/V2O5 hydrogel
e
1 μm
f
(601)
(001)
(002)
(110)
5 1/nm
c
Thiourea
V2O5 gel
Room temp.
After ~20 min
3D VOGOS hydrogel
Graphene oxide
Room temp.
After ~ 2 weeks
V2O5 gel
3D VOGO hydrogel
d
Flat
Bent
0.004
0.000
-0.004
Current / A
0.0
0.5
1.0
1.5
2.0
2.5
Potential / V

Fig. 4

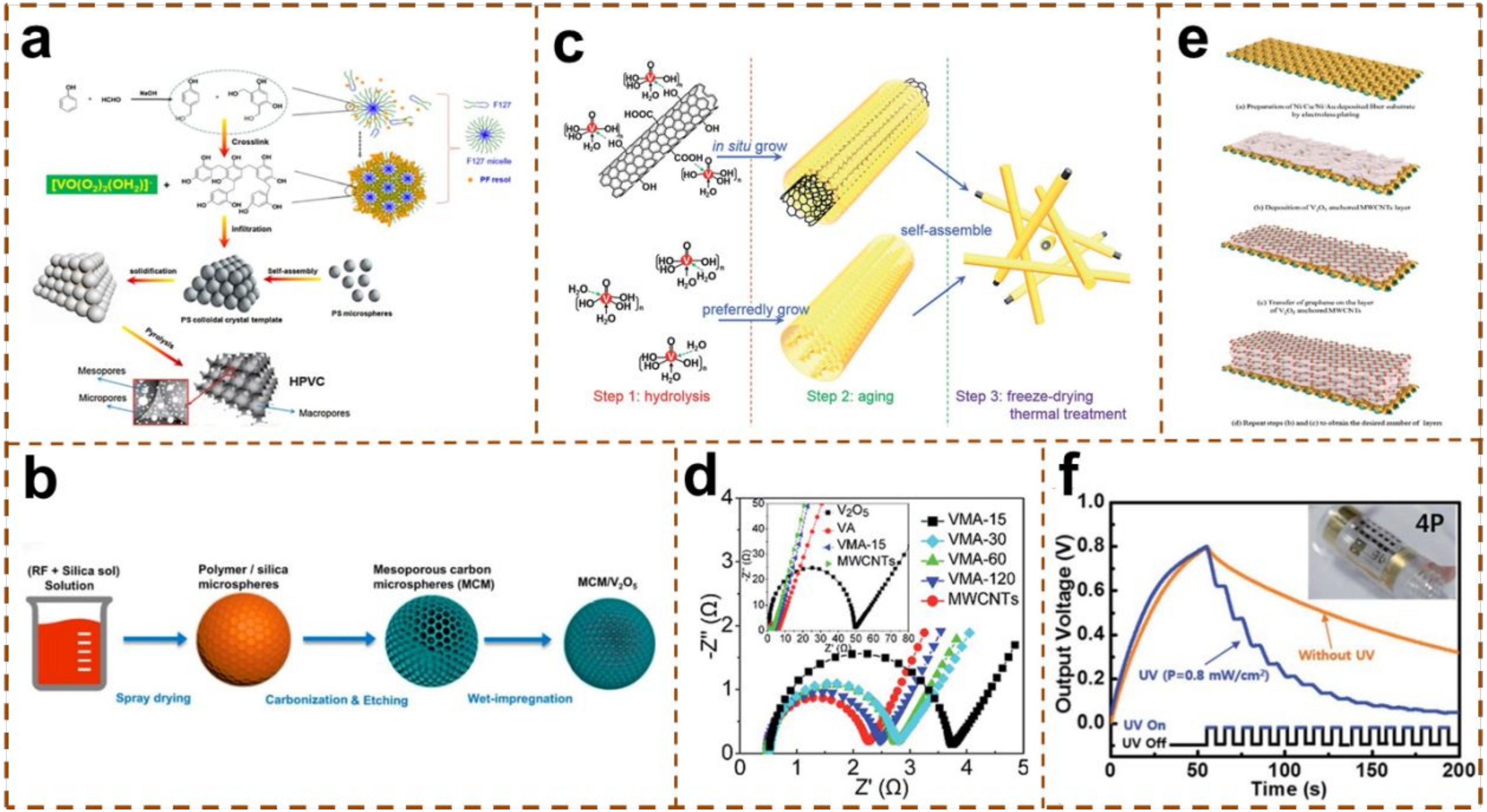
a
HCHO
NaOH
Crosslink
F127
F127 micelle
PF resol
[VO(O2)2(OH2)]-
infiltration
solidification
Self-assembly
PS colloidal crystal template
PS microspheres
Pyrolysis
Mesopores
Micropores
HPVC
Macropores
c
in situ grow
self-assemble
preferredly grow
Step 1: hydrolysis
Step 2: aging
Step 3: freeze-drying
thermal treatment
e
(a) Preparation of Ni/Cu/Ni/Au deposited fiber substrate by electroless plating
(b) Deposition of V2O5 anchored MWCNTs layer
(c) Transfer of graphene on the layer of V2O5 anchored MWCNTs
(d) Repeat steps (b) and (c) to obtain the desired number of layers
b
(RF + Silica sol) Solution
Polymer / silica microspheres
Mesoporous carbon microspheres (MCM)
MCM/V2O5
Spray drying
Carbonization & Etching
Wet-impregnation
d
-Z'' (Ω)
Z' (Ω)
V2O5
VA
VMA-15
MWCNTs
VMA-15
VMA-30
VMA-60
VMA-120
MWCNTs
f
Output Voltage (V)
Time (s)
4P
Without UV
UV (P=0.8 mW/cm2)
UV On
UV Off

Fig. 5

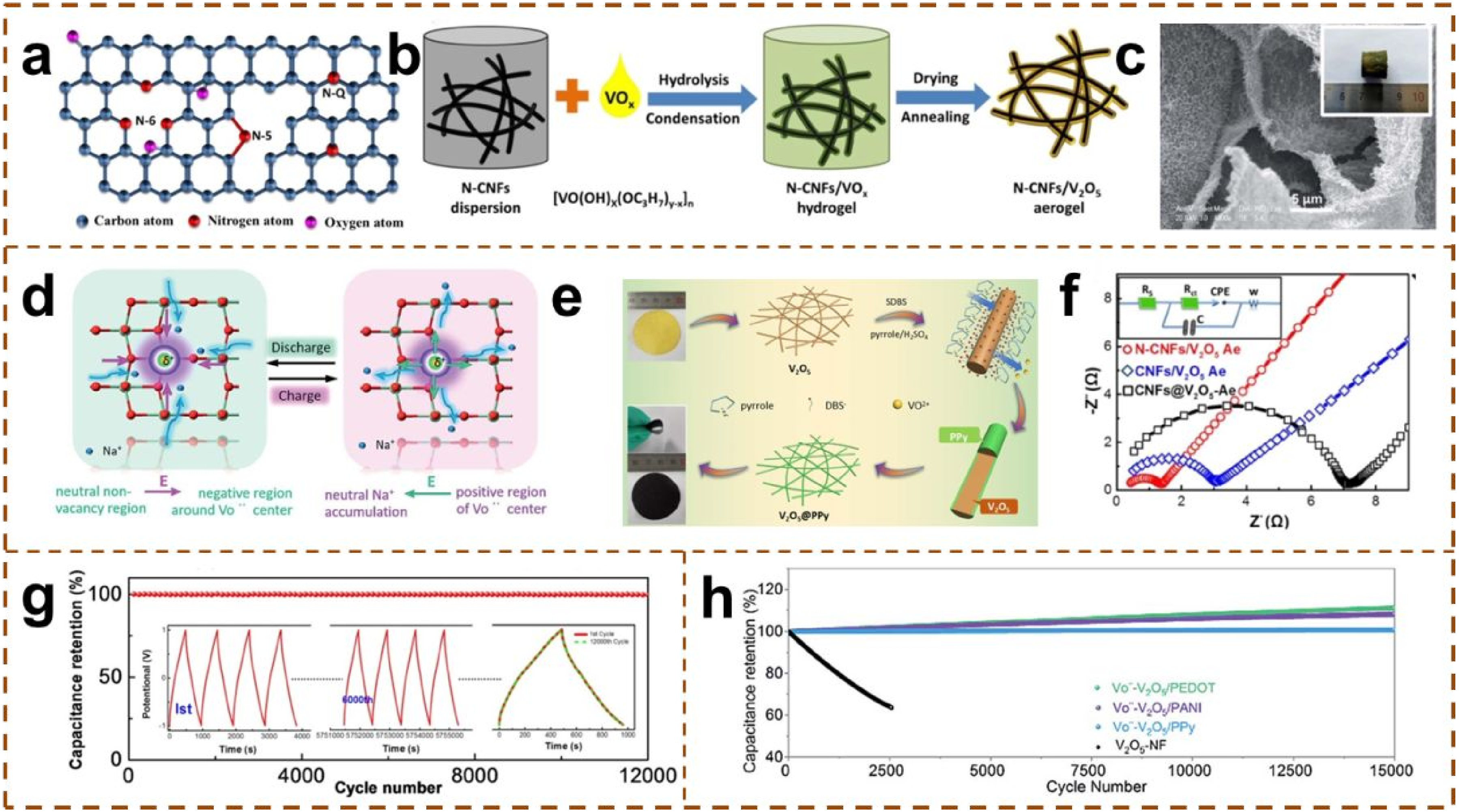
a
N-Q
N-6
N-5
Carbon atom
Nitrogen atom
Oxygen atom
b
N-CNFs dispersion
VOx
[VO(OH)x(OC3H7)y-x]n
Hydrolysis
Condensation
N-CNFs/VOx hydrogel
Drying
Annealing
N-CNFs/V2O5 aerogel
c
5 μm
d
Discharge
Charge
Na+
neutral non-vacancy region
E
negative region around Vo·· center
neutral Na+ accumulation
positive region of Vo·· center
e
V2O5
SDBS
pyrrole/H2SO4
pyrrole
DBS-
VO2+
PPy
V2O5@PPy
f
Rs
Rct
CPE
W
C
N-CNFs/V2O5 Ae
CNFs/V2O5 Ae
CNFs@V2O5-Ae
-Z'' (Ω)
Z' (Ω)
g
Capacitance retention (%)
Cycle number
Potentional (V)
Time (s)
Ist
6000th
1st Cycle
12000th Cycle
h
Capacitance retention (%)
Cycle Number
Vo··-V2O5/PEDOT
Vo··-V2O5/PANI
Vo··-V2O5/PPy
V2O5-NF

Fig. 6

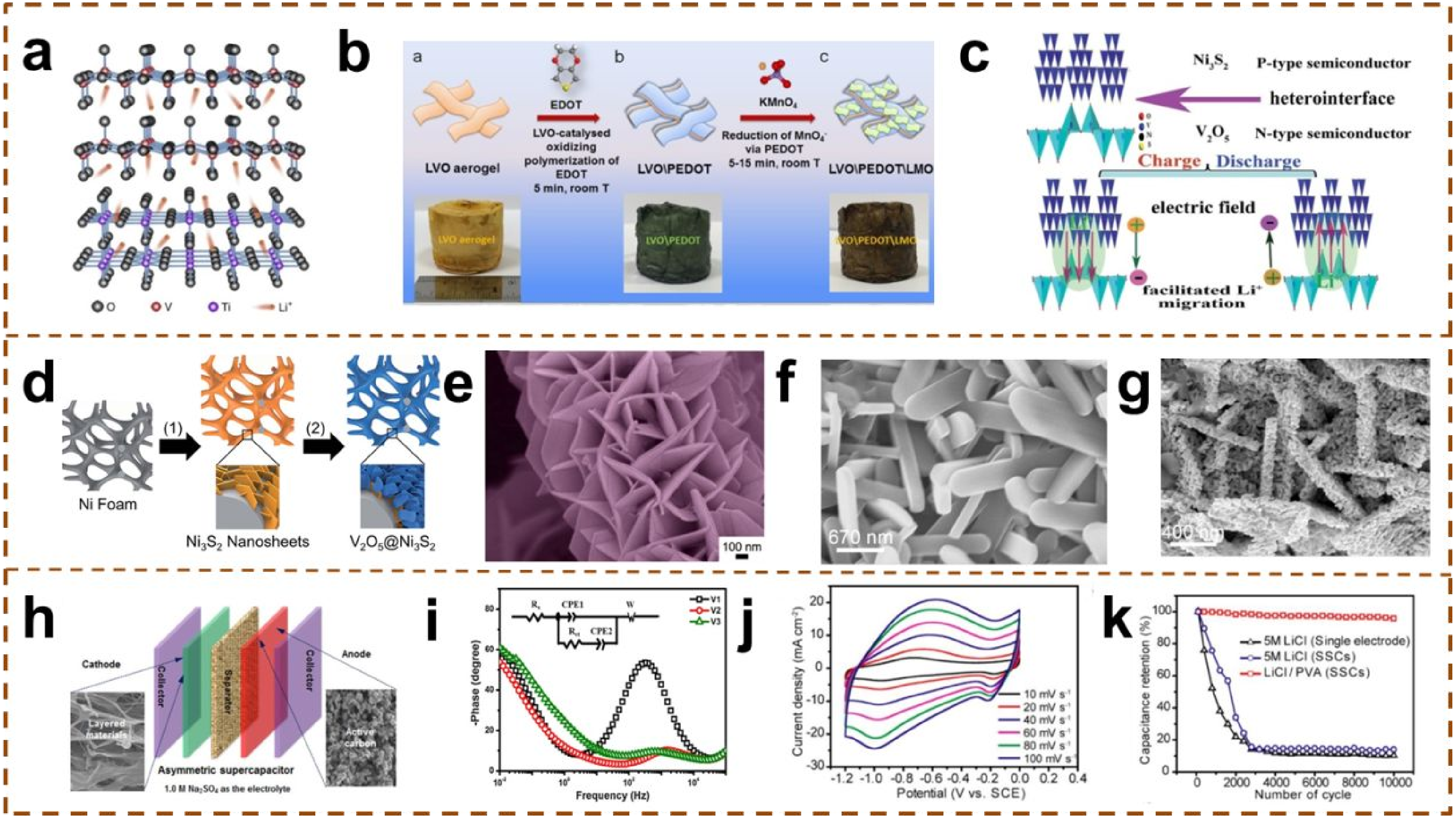
a
O
V
Ti
Li⁺
b
a
EDOT
LVO-catalysed oxidizing polymerization of EDOT 5 min, room T
b
KMnO₄
Reduction of MnO₄⁻ via PEDOT 5-15 min, room T
c
LVO aerogel
LVO\PEDOT
LVO\PEDOT\LMO
c
Ni₃S₂ P-type semiconductor
heterointerface
V₂O₅ N-type semiconductor
Charge Discharge
electric field
facilitated Li⁺ migration
d
Ni Foam
(1)
Ni₃S₂ Nanosheets
(2)
V₂O₅@Ni₃S₂
e
100 nm
f
670 nm
g
400 nm
h
Cathode
Collector
Separator
Anode
Layered materials
Active carbon
Asymmetric supercapacitor
1.0 M Na₂SO₄ as the electrolyte
i
Rₛ CPE1 W
R꜀ₜ CPE2
V1
V2
V3
-Phase (degree)
Frequency (Hz)
j
Current density (mA cm⁻²)
Potential (V vs. SCE)
10 mV s⁻¹
20 mV s⁻¹
40 mV s⁻¹
60 mV s⁻¹
80 mV s⁻¹
100 mV s⁻¹
k
Capacitance retention (%)
Number of cycle
5M LiCl (Single electrode)
5M LiCl (SSCs)
LiCl / PVA (SSCs)

Fig. 7

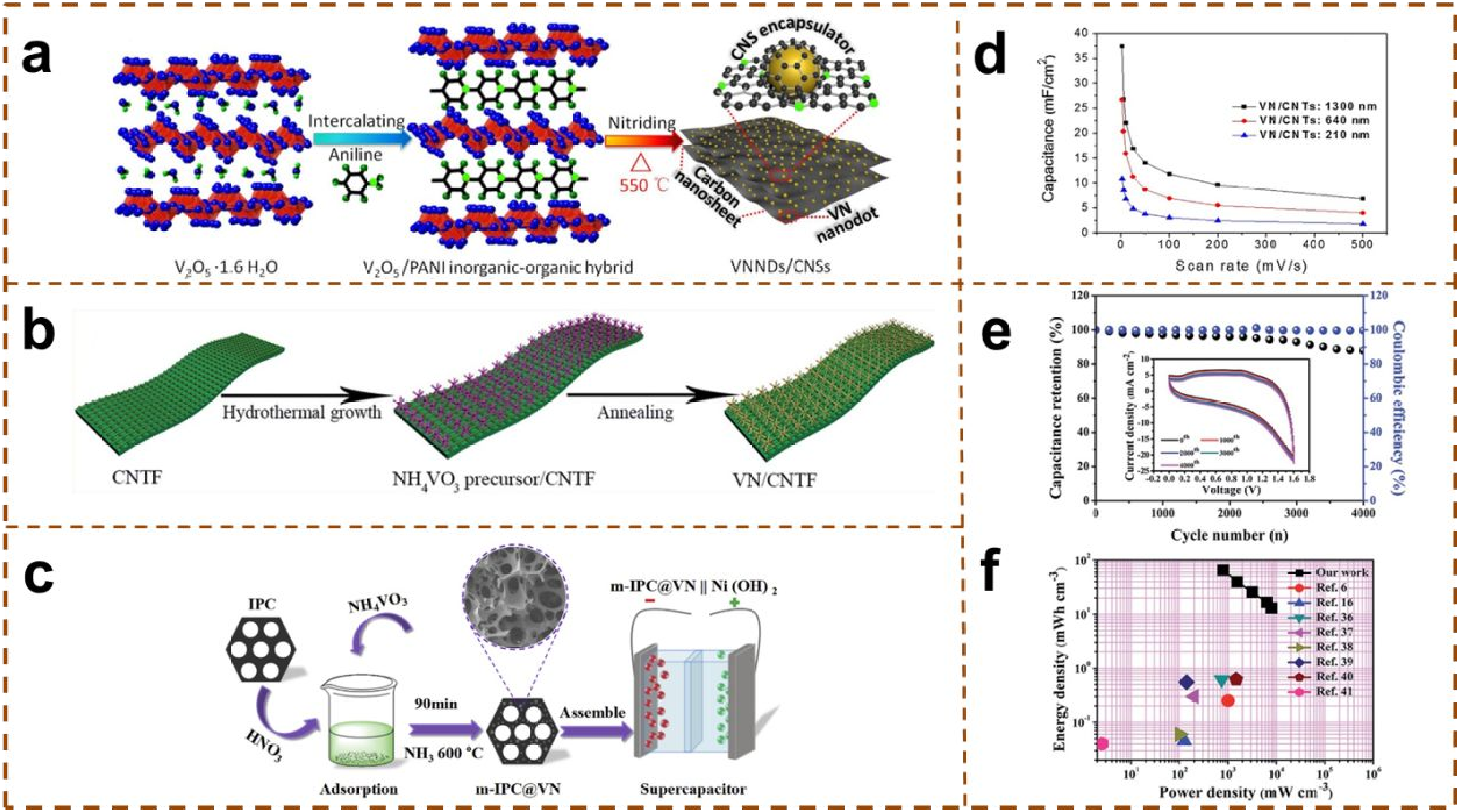
a
Intercalating
Aniline
Nitriding
△
550 ℃
CNS encapsulator
Carbon nanosheet
VN nanodot
V_2O_5·1.6 H_2O
V_2O_5/PANI inorganic-organic hybrid
VNNDs/CNSs
b
Hydrothermal growth
Annealing
CNTF
NH_4VO_3 precursor/CNTF
VN/CNTF
c
IPC
NH_4VO_3
HNO_3
90min
NH_3 600 °C
Assemble
m-IPC@VN || Ni (OH) 2
Adsorption
m-IPC@VN
Supercapacitor
d
Capacitance (mF/cm^2)
Scan rate (mV/s)
VN/CNTs: 1300 nm
VN/CNTs: 640 nm
VN/CNTs: 210 nm
e
Capacitance retention (%)
Coulombic efficiency (%)
Cycle number (n)
Current density (mA cm^{-2})
Voltage (V)
f
Energy density (mWh cm^{-3})
Power density (mW cm^{-3})
Our work
Ref. 6
Ref. 16
Ref. 36
Ref. 37
Ref. 38
Ref. 39
Ref. 40
Ref. 41

Fig. 8

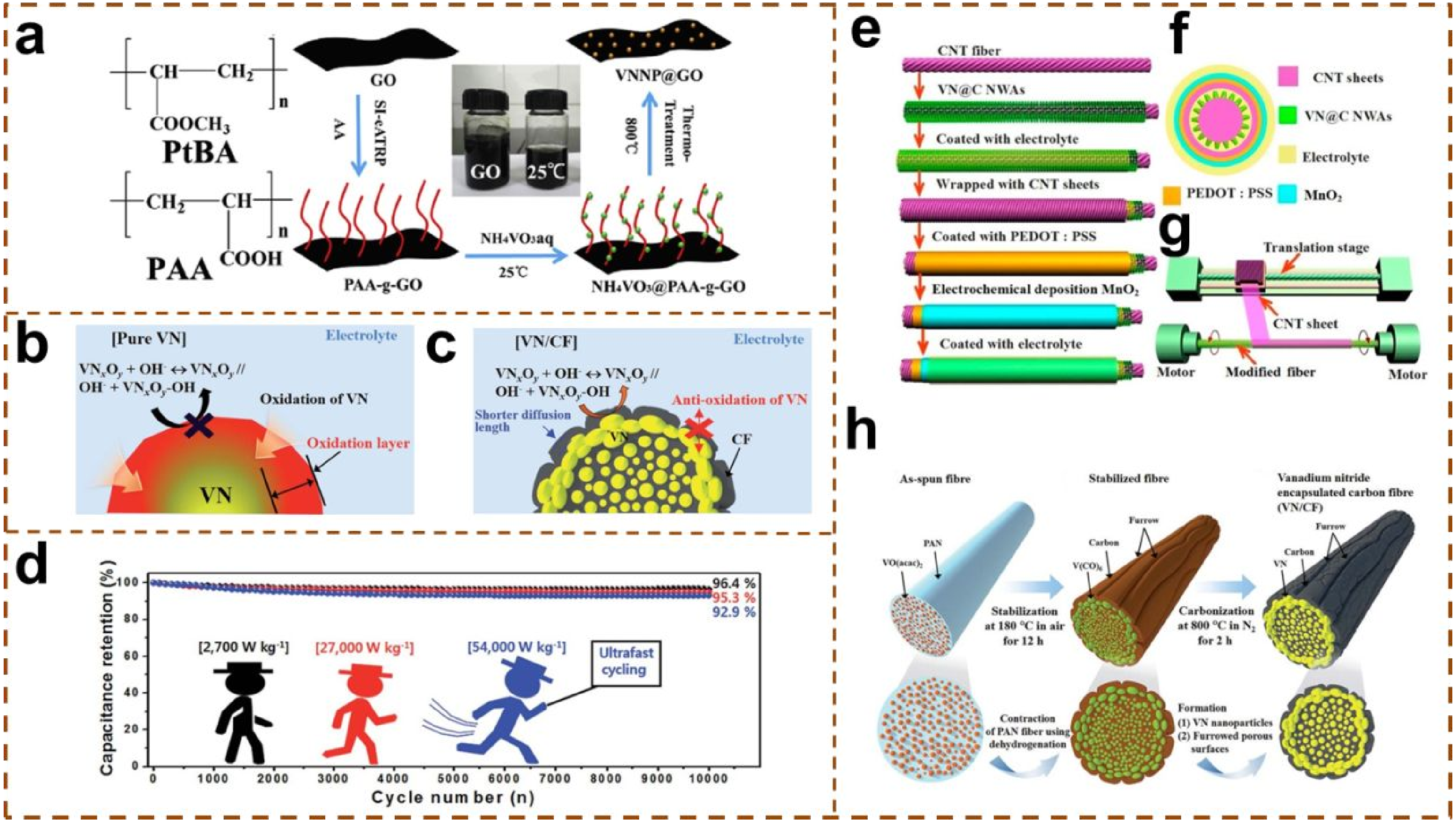
a
CH
CH2
n
COOCH3
PtBA
CH2
CH
n
PAA
COOH
GO
AA
SI-eATRP
PAA-g-GO
GO
25℃
NH4VO3aq
25℃
NH4VO3@PAA-g-GO
800℃
Thermo-Treatment
VNNP@GO
b
[Pure VN]
Electrolyte
VNxOy + OH- ↔ VNxOy // OH- + VNxOy-OH
Oxidation of VN
Oxidation layer
VN
c
[VN/CF]
Electrolyte
VNxOy + OH- ↔ VNxOy // OH- + VNxOy-OH
Anti-oxidation of VN
Shorter diffusion length
VN
CF
d
Capacitance retention (%)
Cycle number (n)
[2,700 W kg-1]
[27,000 W kg-1]
[54,000 W kg-1]
Ultrafast cycling
96.4 %
95.3 %
92.9 %
e
CNT fiber
VN@C NWAs
Coated with electrolyte
Wrapped with CNT sheets
Coated with PEDOT : PSS
Electrochemical deposition MnO2
Coated with electrolyte
f
CNT sheets
VN@C NWAs
Electrolyte
PEDOT : PSS
MnO2
g
Translation stage
CNT sheet
Motor
Modified fiber
Motor
h
As-spun fibre
PAN
VO(acac)2
Stabilization at 180 °C in air for 12 h
Stabilized fibre
Furrow
Carbon
V(CO)x
Carbonization at 800 °C in N2 for 2 h
Vanadium nitride encapsulated carbon fibre (VN/CF)
Furrow
Carbon
VN
Contraction of PAN fiber using dehydrogenation
Formation (1) VN nanoparticles (2) Furrowed porous surfaces

Fig. 9

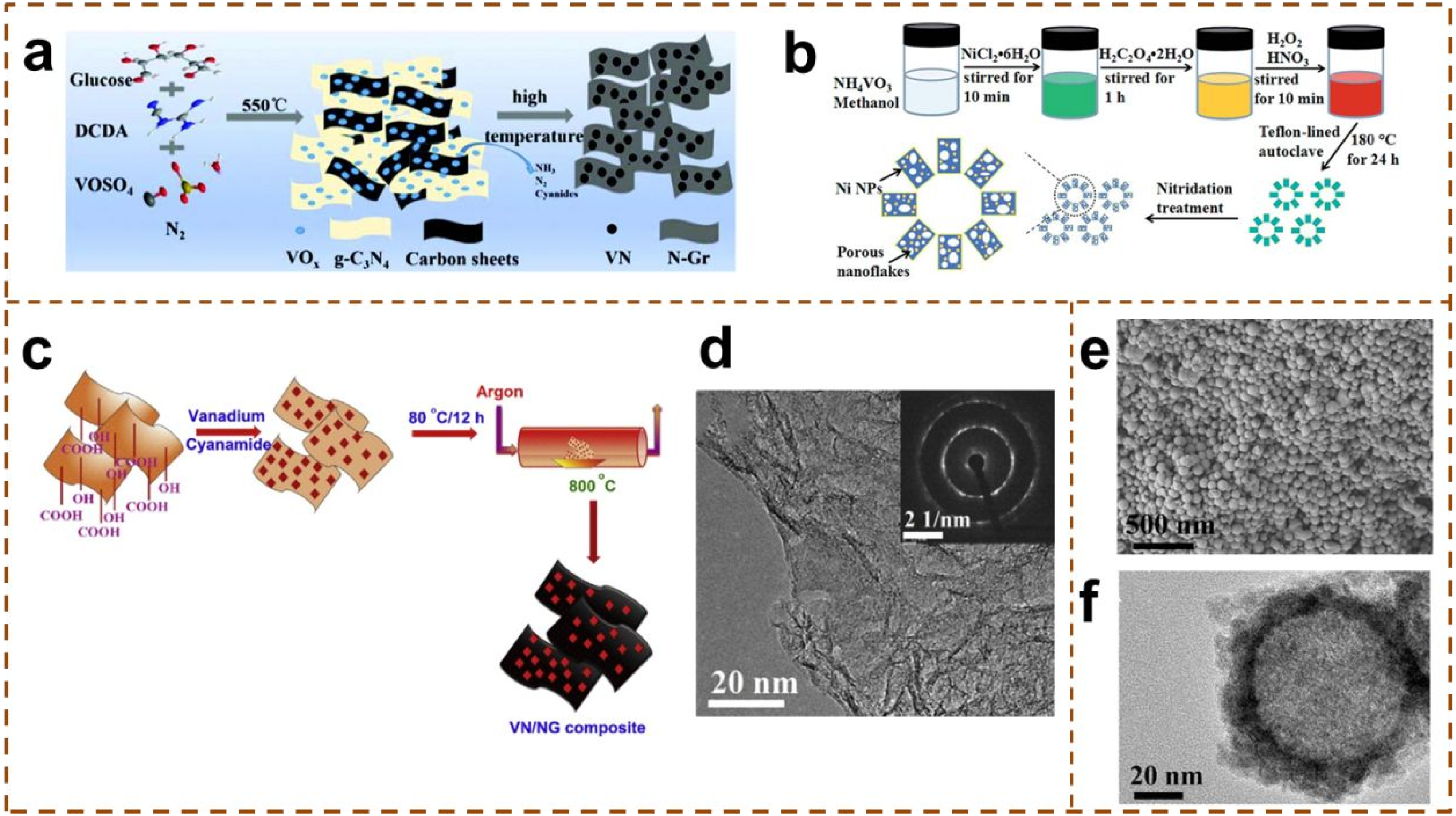
a
Glucose
DCDA
$VOSO_4$
N_2
550℃
high temperature
NH_3
N_2
Cyanides
VO_x
$g-C_3N_4$
Carbon sheets
VN
N-Gr
b
NH_4VO_3
Methanol
$NiCl_2•6H_2O$
stirred for 10 min
$H_2C_2O_4•2H_2O$
stirred for 1 h
H_2O_2
HNO_3
stirred for 10 min
Teflon-lined autoclave
180 °C for 24 h
Nitridation treatment
Ni NPs
Porous nanoflakes
c
OH
COOH
Vanadium
Cyanamide
80 °C/12 h
Argon
800 °C
VN/NG composite
d
2 1/nm
20 nm
e
500 nm
f
20 nm

Fig. 10

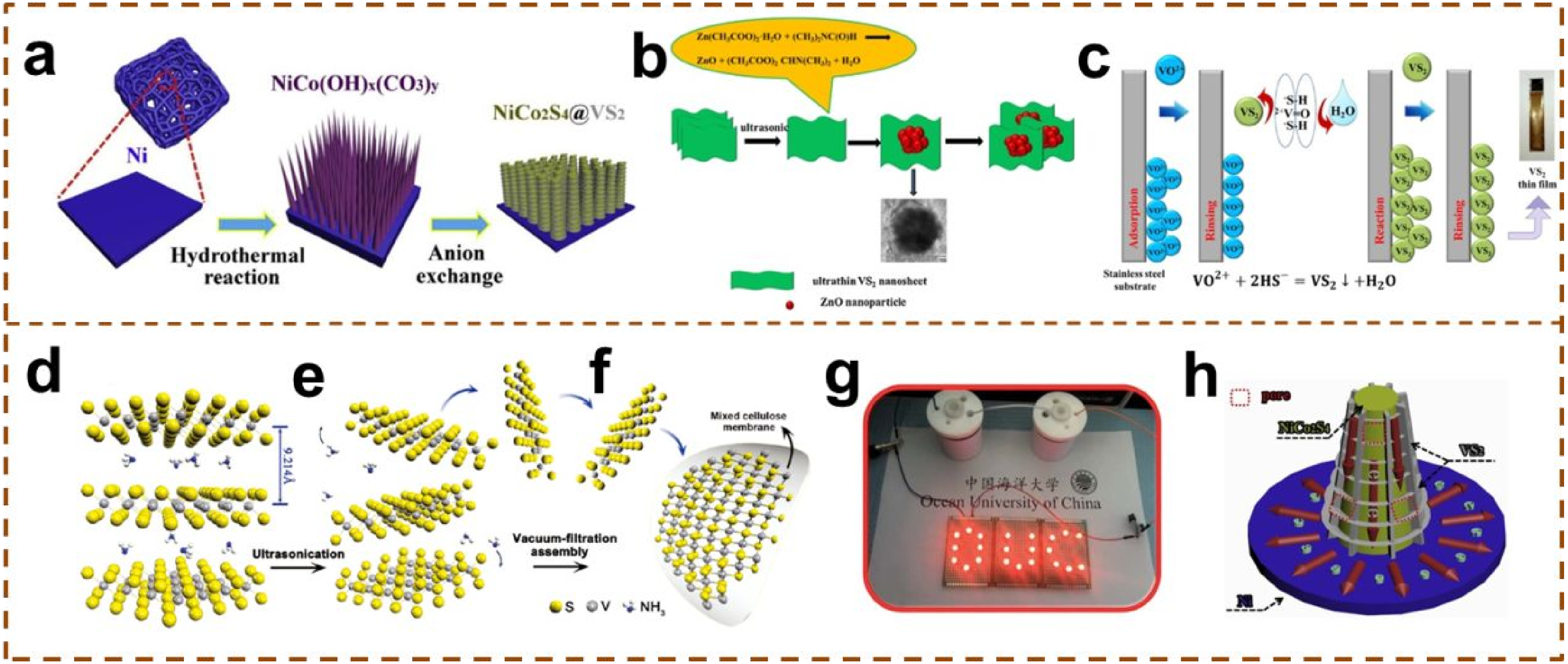
a
Ni
NiCo(OH)x(CO3)y
NiCo2S4@VS2
Hydrothermal reaction
Anion exchange
b
Zn(CH3COO)2·H2O + (CH3)2NC(O)H ⟶
ZnO + (CH3COO)2 CHN(CH3)2 + H2O
ultrasonic
ultrathin VS2 nanosheet
ZnO nanoparticle
c
VO2+
VS2
S-H
V=O
S-H
H2O
Adsorption
Rinsing
Reaction
Rinsing
VS2 thin film
Stainless steel substrate
VO2+ + 2HS− = VS2 ↓ +H2O
d
9.214Å
e
Ultrasonication
f
Vacuum-filtration assembly
Mixed cellulose membrane
S
V
NH3
g
中国海洋大学
Ocean University of China
h
pore
NiCo2S4
VS2
Ni

Fig. 11

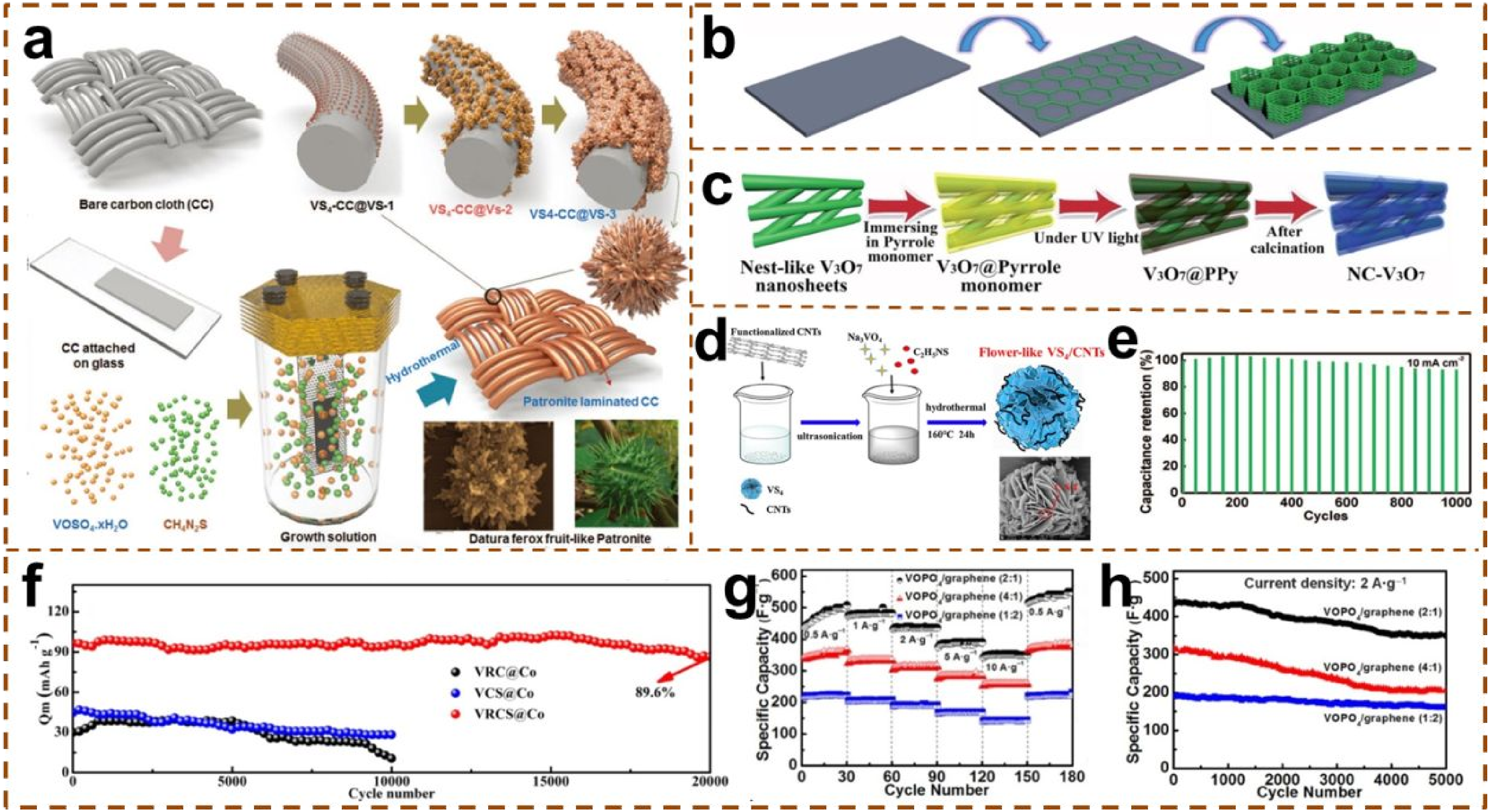
a
Bare carbon cloth (CC)
VS4-CC@VS-1
VS4-CC@Vs-2
VS4-CC@VS-3
CC attached on glass
VOSO4.xH2O
CH4N2S
Growth solution
Hydrothermal
Patronite laminated CC
Datura ferox fruit-like Patronite
b
c
Nest-like V3O7 nanosheets
Immersing in Pyrrole monomer
V3O7@Pyrrole monomer
Under UV light
V3O7@PPy
After calcination
NC-V3O7
d
Functionalized CNTs
Na3VO4
C2H5NS
ultrasonication
hydrothermal
160°C 24h
Flower-like VS4/CNTs
VS4
CNTs
e
Capacitance retention (%)
10 mA cm-2
Cycles
0 200 400 600 800 1000
0 20 40 60 80 100
f
Qm (mAh g-1)
Cycle number
0 5000 10000 15000 20000
0 30 60 90 120
VRC@Co
VCS@Co
VRCS@Co
89.6%
g
Specific Capacity (F·g-1)
Cycle Number
0 30 60 90 120 150 180
0 100 200 300 400 500 600
VOPO4/graphene (2:1)
VOPO4/graphene (4:1)
VOPO4/graphene (1:2)
0.5 A·g-1
1 A·g-1
2 A·g-1
5 A·g-1
10 A·g-1
0.5 A·g-1
h
Current density: 2 A·g-1
Specific Capacity (F·g-1)
Cycle Number
0 1000 2000 3000 4000 5000
0 100 200 300 400 500
VOPO4/graphene (2:1)
VOPO4/graphene (4:1)
VOPO4/graphene (1:2)

Fig. 12

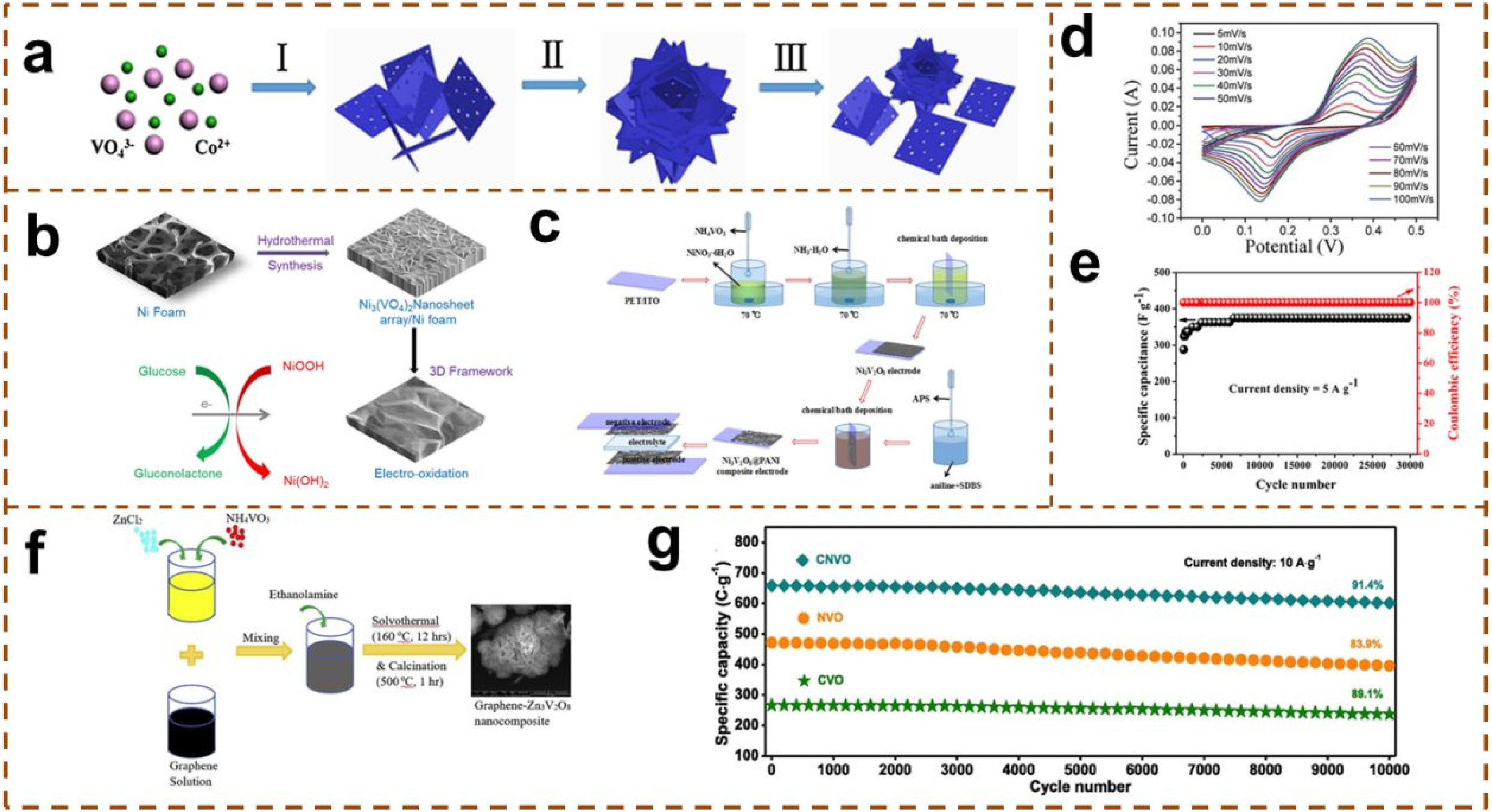
a
VO$_4^{3-}$
Co^{2+}
I
II
III
b
Ni Foam
Hydrothermal Synthesis
Ni$_3$(VO$_4$)$_2$Nanosheet array/Ni foam
3D Framework
Glucose
NiOOH
e-
Gluconolactone
Ni(OH)$_2$
Electro-oxidation
c
PET/ITO
NH$_4$VO$_3$
NiNO$_3$·6H$_2$O
70 ℃
NH$_3$·H$_2$O
chemical bath deposition
Ni$_3$V$_2$O$_8$ electrode
APS
aniline+SDBS
Ni$_3$V$_2$O$_8$@PANI composite electrode
negative electrode
electrolyte
positive electrode
d
Current (A)
Potential (V)
5mV/s
10mV/s
20mV/s
30mV/s
40mV/s
50mV/s
60mV/s
70mV/s
80mV/s
90mV/s
100mV/s
0.10
0.08
0.06
0.04
0.02
0.00
-0.02
-0.04
-0.06
-0.08
-0.10
0.0
0.1
0.2
0.3
0.4
0.5
e
Specific capacitance (F g^{-1})
Coulombic efficiency (%)
Current density = 5 A g^{-1}
Cycle number
0
5000
10000
15000
20000
25000
30000
500
400
300
200
100
120
100
80
60
40
20
f
ZnCl$_2$
NH$_4$VO$_3$
Graphene Solution
Mixing
Ethanolamine
Solvothermal (160 ºC, 12 hrs)
& Calcination (500 ºC, 1 hr)
Graphene-Zn$_3$V$_2$O$_8$ nanocomposite
g
Specific capacity (C·g^{-1})
Cycle number
Current density: 10 A·g^{-1}
CNVO
NVO
CVO
91.4%
83.9%
89.1%
800
700
600
500
400
300
200
100
0
1000
2000
3000
4000
5000
6000
7000
8000
9000
10000

Fig. 13

Table 1

Materials	Advantage	Disadvantage
Metal nitride	Small resistance, high chemical stability and thermal stability, and low cost	Low specific capacity
Metal sultride	Large electrical conductivity, mechanical and thermal durability, and high specific capacity	Poor stability
Metal telluride	High conductivity, and special physical and chemical proporties	Complex synthesis
Carbon material	Large specific surface area, long cycle stability, high conductivity, and chemical stability	Low specific capacitance, large resistance
Conducting polymer	High conducitvity	Poor stability
Tranditional metal oxides	Great mechanical strength, high thermal and chemical stability, bio- and environmental compatibility, and flexible surface chemistry and architecture	High internal resistance and cost
V-based materials	Unique layered structure, various valence, low cost, and easy availability	Poor thermal stability

Table 2

Nano-structures (dimension)	Synthetic method	Electrolyte	Potential window (V)	Maximum SC	Current density	Cycling stability (%)	Ref.
VO_2-6 h nanosheets (2D)	Solvothermal method	6 M KOH	0.0~0.5	663 $F\cdot g^{-1}$	5 $mV\cdot s^{-1}$	99.4% (9000 cycles)	44
VO_2 nanosheet (2D)	Hydrothermal method	1 M $LiClO_4$/PPC	-0.3~1.1	405 $F\cdot g^{-1}$	1 $A\cdot g^{-1}$	82% (6000 cycles)	31
VO_2 monoclinic nanosheets (2D)	Solvothermal method	6 M KOH	0.0~0.5	47 $mAh\cdot g^{-1}$	1 $A\cdot g^{-1}$	89% (10 000 cycles)	45
Monoclinic VO_2 nanorod thin films (2D)	Radio-frequency reactive magnetron sputtering	0.1 M NaOH	0.0~0.8	486 $mF\cdot cm^{-2}$	10 $mV\cdot s^{-1}$	100% (5000 cycles)	46
VO_2 nanoporous structure (2D)	CVD technique.	Na_2SO_4	0.0~0.5	20.7 $mF\cdot cm^{-2}$	0.3 $mA\cdot cm^{-2}$	93.7% (5000 cycles)	41
VO_2(B) hollow spheres (3D)	Hydrothermal method	1 M Na_2SO_4/CMC	-0.5~1.0	336 $F\cdot g^{-1}$	2 $mA\cdot cm^{-2}$	68% (10 000 cycles)	32
VO_2(B)/C core-shell composites	Hydrothermal method	1 M Na_2SO_4	-0.6~0.8	203 $F\cdot g^{-1}$	0.2 $A\cdot g^{-1}$	10.4% (100 cycles)	51
VO_2 NFs@3DG	CVD–hydrothermal method	0.5 M K_2SO_4	-0.6~0.6	507 $F\cdot g^{-1}$	3 $mA\cdot cm^{-2}$	63.5% (3000 cycles)	52
VO_2(B) nanobelts/rGO composite	Hydrothermal method	0.5 M K_2SO_4	-1.0~0.0	353 $F\cdot g^{-1}$	1 $A\cdot g^{-1}$	78% (10 000 cycles)	53
VO_2 nanoparticle/EOGF	Hydrothermal method	5 M LiCl	0.0~0.8	119 $mF\cdot cm^{-2}$	2 $mV\cdot s^{-1}$	70% (1500 cycles)	54
GF + VO_2/HMB	The chemical vapour deposition method	1 M K_2SO_4	-0.3~1.5	485 $F\cdot g^{-1}$	2 $A\cdot g^{-1}$	97.5% (5000 cycles)	55
Hydrogen treated VO_2	Thermal treatment method	1 M Na_2SO_4	0.0~0.8	300 $F\cdot g^{-1}$	1 $A\cdot g^{-1}$	96% (1000 cycles)	57
VO_2-N microarray	An organic–inorganic liquid interface	1 M Na_2SO_4	0.0~0.6	265 $F\cdot g^{-1}$	1 $A\cdot g^{-1}$	100% (3000 cycles)	56

Table 3

Nano-structures	Synthetic method	Electrolyte	Potential window (V)	Maximum SC	Current density	Cycling stability (%)	Ref.
V_2O_3@C core-shell composites	Heat treatment method	1 M Na_2SO_4	-0.2~0.8	223 $F\cdot g^{-1}$	0.1 $A\cdot g^{-1}$	39.7% (100 cycles)	62
V_2O_3@C core-shell nanorods	Hydrothermal method	5 M LiCl	-1.0~-0.3	228 $F\cdot g^{-1}$	0.5 $A\cdot g^{-1}$	86% (1000 cycles)	33
V_2O_3 nanofoam@activated carbon composites	Solvothermal method	1 M $NaNO_3$	-0.4~0.6	185 $F\cdot g^{-1}$	0.05 $A\cdot g^{-1}$	49% (100 cycles)	63
V_2O_3/C nanocomposites	Hydrothermal method	5 M LiCl	-1.0~-0.4	458.6 $F\cdot g^{-1}$	0.5 $A\cdot g^{-1}$	86% (1000 cycles)	64
V_2O_3/N-rGO nanoflakes	Hydrothermal method	1 M Na_2SO_4	-0.2~0.6	216 $mF\cdot cm^{-2}$	1 $mA\cdot cm^{-2}$	81% (10 000 cycles)	65

Table 4

Nano-structures (Dimension)	Synthetic method	Electrolyte	Potential window (V)	Maximum SC	Current density	Cycling stability (%)	Ref.
V_2O_5 nanofibers (1D)	Electrospinning method	2 M KCl 1 M $LiClO_4$/PPC	-0.2~0.7 0.0~3.0	190 F·g^{-1} 250 F·g^{-1}	0.1 A·g^{-1}	—	43
V_2O_5 nanoporous network (2D)	Capping-agent-assisted precipitation technique	0.5 M K_2SO_4	0.0~1.0	304 F·g^{-1}	100 mA·g^{-1}	76% (600 cycles)	66
$V_2O_5\cdot H_2O$ (2D)	Hydrothermal method	2 M KCl	-0.2~0.8	349 F·g^{-1}	5 mV·s^{-1}	—	68
V_2O_5 complex (2D)	CBD	2 M $LiClO_4$	0.0~1.0	735 F·g^{-1}	1 mV·s^{-1}	71% (1000 cycles)	71
Hollow spherical V_2O_5 (3D) Hollow spherical V_2O_5/PPy (3D)	Solvothermal method	5 M $LiNO_3$	-0.2~0.8	479 F·g^{-1} 566 F·g^{-1}	5 mV·s^{-1}	43% (100 cycles) 70% (100 cycles)	67
V_2O_5 nanofibers (3D)	Sol-gel method	1 M KCl ULP gel	0.0~1.6 0.0~4.0	— 160 F·g^{-1}	— 1 A·g^{-1}	72.2% (5000 cycles) 91% (5000 cycles)	70
rGO/V_2O_5 hybrid aerogel composite	modified Hummer's method	1 M LiClO4/PPC	-0.8~0.8	384 F·g^{-1}	0.1 A·g^{-1}	82.2% (10 000 cycles)	74
VNF/graphene nanohybrid	Hydrothermal and In-situ chemical method	1 M LiTFSI in acetonitrile	-0.4~1.2	218 F·g^{-1}	1 A·g^{-1}	87% (700 cycles)	75
rGO/V_2O_5 nanobelts hybrid	Hydrothermal method	0.5 M K_2SO_4	-0.5~0.5	310.1 F·g^{-1}	1 A·g^{-1}	90.2% (5000 cycles)	76
rGO/V_2O_5 nanosheet	modified Hummers method	1 M KCl	0.0~0.8	635 F·g^{-1}	1 A·g^{-1}	94% (3000 cycles)	77
V_2O_5–graphene hybrid	modified Hummers method	1 M Na_2SO_4	0.0~1.6	484 F·g^{-1}	0.6 A·g^{-1}	80% (10 000 cycles)	78
V_2O_5@rGO nanorods	Sol-gel method/modified	0.75 M $NaPF_6$	0.0~3.0	289 F·g^{-1}	0.01 A·g^{-1}	85% (1000 cycles)	38

	Hummers method	in ethylene carbonate (EC)–diethyl carbonate (DEC) (1:1 in volume)					
3DG -wrapped V_2O_5 nanospheres	Hydrothermal method	1 M Na_2SO_4	0.0~0.8	612.5 $F \cdot g^{-1}$	1 $A \cdot g^{-1}$	89.6% (10 000 cycles)	79
rGO/V_2O_5	modified Hummers method	1 M $LiClO_4$/PPC	-0.8~0.8	129.7 $F \cdot g^{-1}$	0.1 $A \cdot g^{-1}$	85% (8000 cycles)	80
Carbon coated flower V_2O_5	Co-precipitation method	1 M K_2SO_4	-0.1~0.8	417 $F \cdot g^{-1}$	0.5 $A \cdot g^{-1}$	100% (2000 cycles)	81
V_2O_5/C (HPVC) nanocomposites	—	2 M $LiNO_3$	0.0~1.0	492.1 $F \cdot g^{-1}$	5 $mV \cdot s^{-1}$	93% (10 000 cycles)	82
MCM/V_2O_5	Spray drying and wet impregnation method	1 M $Al_2(SO_4)_3$	0.0-1.6	290 $F \cdot g^{-1}$	0.5 $A \cdot g^{-1}$	88% (10 000 cycles)	83
CNT/V_2O_5 nanocomposite	Hydrothermal method	1 M $LiClO_4$/PPC	1.6~4.0	228 $C \cdot g^{-1}$	20 $mV \cdot s^{-1}$	80% (10 000 cycles)	84
V_2O_5/carbon nanofiber composites	Electrospinning method	6 M KOH	0.0~1.0	150 $F \cdot g^{-1}$	1 $mA \cdot cm^{-2}$	—	85
V_2O_5/MWCNT core/shell hybrid aerogels	Sol–gel method	1 M Na_2SO_4	-0.1~1.0	625 $F \cdot g^{-1}$	0.5 $A \cdot g^{-1}$	120% (20 000 cycles)	39
Ultrathin V_2O_5 anchored MWCNTs and graphene composites	LBL technique	2 M KCl	-0.6~0.6	2590 $F \cdot g^{-1}$	1 $mV \cdot s^{-1}$	96% (5000 cycles)	86
MWNT/V_2O_5 NW composites	Sol-gel method	PVA-LiCl	0.0~0.8	80 $F \cdot cm^{-3}$	10 $mV \cdot s^{-1}$	82% (10 000 cycles)	87
3D N-CNFs/V_2O_5 aerogels	—	1 M Na_2SO_4	-1.0~1.0	595.1 $F \cdot g^{-1}$	0.5 $A \cdot g^{-1}$	97% (12 000 cycles)	88

V_2O_5 NW/3D N-GA	Solvothermal methhod	8 M LiCl	-0.3~0.7	710 F·g^{-1}	0.5 A·g^{-1}	95% (20 000 cycles)	89
3D V_2O_5/PPy core/shell nanostructures	—	5 M $LiNO_3$	-0.2~0.8	448 F·g^{-1}	0.5 A·g^{-1}	81% (1000 cycles)	90
V_2O_5@PPy core−shell NW	Hydrothermal and in situ interfacial synthesis approach	1 M Na_2SO_4	-0.4~0.5	344 F·g^{-1}	0.2 A·g^{-1}	82.5% (2000 cycles)	91
V_2O_5-Conductive polymer nanocables	—	1 M Na_2SO_4	-1.0~1.0	614 F·g^{-1}	0.5 A·g^{-1}	111% (15 000 cycles)	92
V_2O_5/TiO_2 composites	Hydrothermal method	1 M $LiNO_3$	-0.2~0.8	587 F·g^{-1}	0.5 A·g^{-1}	92% (1000 cycles)	98
V_2O_5-doped-α-Fe_2O_3 composite nanotubes	Electrospinning method	3 M KOH	-0.1~0.6	183 F·g^{-1}	1 A·g^{-1}	81.5% (200 cycles)	100
V_2O_5/Ni_3S_2 nanoflakes	Hydrothermal method	2 M NaOH	0.0~0.5	3060 F·g^{-1}	1 mV·s^{-1}	85% (2500 cycles)	101
V_2O_5@Ni_3S_2 hybrid nanoarray	Hydrothermal method	1 M KOH	0.0~0.6	854 F·g^{-1}	1 A·g^{-1}	60% (1000 cycles)	102
V_2O_5/$Na_{0.33}V_2O_5$	Co-precipitation technique	1 M $LiClO_4$	-0.2~0.6	334 F·g^{-1}	1 A·g^{-1}	96% (1000 cycles)	103
SnO_2–V_2O_5–CNT	Solid-state and hydrothermal method	0.1 M KCl	0.0~0.8	121.39 F·g^{-1} (Anodic) 119.85 F·g^{-1} (Cathodic)	100 mV·s^{-1} 100 mV·s^{-1}	85.8% (100 cycles) (Anodic) 87.2% (100 cycles) (Cathodic)	104
V_2O_5/PEDOT/MnO_2 nanosheets	Hydrothermal method	1 M Na_2SO_4	0.0~0.8	266.4 F·g^{-1}	2 mV·s^{-1}	93.5% (3000 cycles)	105

Table 5

Nano-structures (Dimension)	Synthetic method	Electrolyte	Potential window (V)	Maximum SC	Current density	Cycling stability (%)	Ref.
VN (0D)	Temperature-programmed method	1 M KOH	-0.2~0.6	186 $F\cdot g^{-1}$	1 $A\cdot g^{-1}$	—	106
VN (0D)	Temperature-programmed reaction method	0.1 M KOH	-1.1~0.1	—	—	93% (2700 cycles)	107
Porous VN NW (1D)	Hydrothermal method	LiCl/PVA gel	-1.2~0.0	298.5 $F\cdot g^{-1}$	10 $mV\cdot s^{-1}$	95% (10 000 cycles)	34
VN nanofibers (1D)	Electrospinning method	LiCl/PVA gel	0.0~1.0	110.8 $F\cdot g^{-1}$	5 $mV\cdot s^{-1}$	75.1% (2000 cycles)	108
Nano-VN/IPC	Surface-initiated electrochemical mediated ATRP and heat-treatment approach	2 M KOH	-1.2~0.0	284 $F\cdot g^{-1}$	0.5 $A\cdot g^{-1}$	65% (10 000 cycles)	109
m-IPC@VN	Ultra-concentrated emulsion polymerization technology	6 M KOH	-1.2~0.0	260 $F\cdot g^{-1}$	0.5 $A\cdot g^{-1}$	91.1% (1000 cycles)	110
VNNDs/CNSs	Hydrothermal method	KOH/PVA	-1.0~0.1	1203.6 $F\cdot cm^{-3}$	1.1 $A\cdot cm^{-3}$	90% (10 000 cycles)	111
VN/CNT	ECR-PECVD	0.5 M K_2SO_4	-1.0~0.4	37.5 $mF\cdot cm^{-2}$	2 $mV\cdot s^{-1}$	85% (20 000 cycles)	112
Porous VN NWs/CNTF	one-step hydrothermal process	PVA-KOH	-1.2~-0.2	196.43 $mF\cdot cm^{-2}$	1 $mA\cdot cm^{-2}$	87.9% (4000 cycles)	113
VN-MWCNT materials	Chemical method	0.5 M Na_2SO_4	-0.9~0.0	160 $F\cdot g^{-1}$	2 $mV\cdot s^{-1}$	80% (1000 cycles)	114
VN/CF	Hydrothermal and annealing method	6 M KOH	-1.2~0.0	800 $F\cdot g^{-1}$	4 $A\cdot g^{-1}$	92.9% (10 000 cycles)	116

VN@CNWAs/CNT fiber	Two-step approach	1 M Na_2SO_4	-1.2~-0.2	715 mF·cm^{-2}	1 mA·cm^{-2}	90% (6000 cycles)	117
VN/NC nanocomposites	—	2 M KOH	-1.2~0.0	299 F·g^{-1}	1 A·g^{-1}	74.8% (5000 cycles)	118
VN-G	CVD	PVA/KOH gel	0.0~1.0	53 F·g^{-1}	10 mV·s^{-1}	90% (3000 cycles)	42
VNNP/GO composites	SI-eATRP technique	2 M KOH	-1.2~0.0	109.7 F·g^{-1}	1 A·g^{-1}	93% (5000 cycles)	119
VN/N-doped Graphene nanocomposites	Two-step heating method	2 M KOH	-1.0~0.2	342.1 F·g^{-1}	0.5 A·g^{-1}	—	120
VN/NG composite	modified Hummers method	6 M KOH	-1.0~0.0	445 F·g^{-1}	1 A·g^{-1}	98.66% (10 000 cycles)	121
Ni/VN HHMS	Solvothermal and annealing method	2 M KOH	-1.0~0.0	143.2 F·g^{-1}	0.5 A·g^{-1}	87% (1000 cycles)	122
3-Ni/VN/NCs-7 composite	Calcining method	2 M KOH	-1.2~0.0	236 F·g^{-1}	1 A·g^{-1}	85.8% (5000 cycles)	123
Core-shell TiN-VN fibers	Electrospinning and annealing method	1 M KOH	-1.2~-0.2	262 F·g^{-1}	2 mV·s^{-1}	88% (500 cycles)	124
TiVN composite	Solvethermal method	6 M KOH	-0.6~0.2	729 F·g^{-1}	2 A·g^{-1}	85.9% (300 cycles)	125

Table 6

Nano-structures (Dimension)	Synthetic method	Electrolyte	Potential window (V)	Maximum SC	Current density	Cycling stability (%)	Ref.
VS_2 thin film (2D)	SILAR method	2 M KCl	-0.6~0.2	247 $F\cdot g^{-1}$	0.5 $mA\cdot cm^{-2}$	89% (6000 cycles)	126
VS_2 nanosheets (2D)	Hydrothermal method	$BMIMBF_4$-PVA	-0.6~0.6	317 $F\cdot g^{-1}$	0.1 $A\cdot m^{-2}$	90% (1000 cycles)	127
VS_2 nanoplates (2D)	colloidal method	1 M KOH	-0.2~0.8	2200 $F\cdot g^{-1}$	1 $A\cdot g^{-1}$	85% (5000 cycles)	128
ZnO/VS_2 nanocomposite	A simple solution method	2 M KOH	-0.3~0.7	2695.7 $F\cdot g^{-1}$	1 $A\cdot g^{-1}$	92.7% (5000 cycles)	130
$NiCo_2S_4$@ VS_2	Hydrothermal method	3 M KOH	0.0~0.6	1023.4 $C\cdot g^{-1}$	0.45 $A\cdot g^{-1}$	96% (2000 cycles)	35
VS_4/CNTs composite	Hydrothermal method	1 M $LiClO_4$	-1.2~1.2	330 $F\cdot g^{-1}$	1 $A\cdot g^{-1}$	63% (5000 cycles)	131
VS_4/rGO	modified Hummer's method	1 M Na_2SO_4	-0.1~0.8	877 $F\cdot g^{-1}$	0.5 $A\cdot g^{-1}$	90% (1000 cycles)	132
VS_4/CNTs/rGO hybrid	Hydrothermal method	0.5 M K_2SO_4	-0.8~0.8	558.7 $F\cdot g^{-1}$	1 $A\cdot g^{-1}$	97% (1000 cycles)	133
VS_4-CC@VS-3	Hydrothermal method	1 M [EMIM] [OTf]	0.0~2.0	536 $mF\cdot cm^{-2}$	1 $mA\cdot cm^{-2}$	93% (1000 cycles)	134
VS_4/rGO/CoS_2@Co	Hydrothermal method	1 M KOH	-0.2~0.55	1353 $F\cdot g^{-1}$	0.625 $A\cdot g^{-1}$	89.6% (20 000 cycles)	135

Table 7

Nano-structures (Dimension)	Synthetic method	Electrolyte	Potential window (V)	Maximum SC	Current density	Cycling stability (%)	Ref.
$Co_3V_2O_8$ nanoparticles (0D)	Microwave-assisted hydrothermal synthesis method	6 M KOH	0.0~0.6	159.7 C·g^{-1}	1 mA·cm^{-2}	94.6% (1000 cycles)	137
$Co_3V_2O_8$ nanoparticles (0D)	Co-preparation method	2 M KOH	-0.2~0.6	505 F·g^{-1}	0.625 A·g^{-1}	92.6% (1000 cycles)	138
$BiVO_4$ nanoparticles (0D)	—	KOH	-0.6~0.8	1166 F·g^{-1}	1 A·g^{-1}	85% (500 cycles)	153
$Zn_2V_2O_7$ (1D)	Hydrothermal method	6 M KOH	0.0~0.6	427.7 F·g^{-1}	1 mA·cm^{-2}	83.71% (1000 cycles)	151
$Co_3V_2O_8$ thin sheets (2D)	Hydrothermal	6 M KOH	-0.2~0.7	1320 F·g^{-1}	1 A·g^{-1}	89.1% (10 000 cycles)	36
$Ni_3V_2O_8$ nanoflake (2D)	Dropwise	2 M KOH	-0.2~0.6	1181 F·g^{-1}	0.625 A·g^{-1}	92.6% (1000 cycles)	138
$Ni_3V_2O_8$ thin sheets (2D)	Hydrothermal method	6 M KOH	-0.2~0.7	1992.5 F·g^{-1}	1 A·g^{-1}	83.9% (10 000 cycles)	36
3D porous hydrated cobalt pyrovanadate microflowers (3D)	Co-preparation method	2 M KOH	-0.1~0.5	351 F·g^{-1}	1 A·g^{-1}	103% (3000 cycles)	136
CoV_2O_6 micron blocks (3D)	Microwave-assisted hydrothermal synthesis method	6 M KOH	0.0~0.6	114.1 C·g^{-1}	1 mA·cm^{-2}	81.91% (1000 cycles)	137
Aluminum vanadate (3D)	Hydrothermal method	1.0 M Na_2SO_4	0.0-1.0	497 F·g^{-1}	1 A·g^{-1}	89% (10 000 cycles)	156
3D $Co_3O_4/Co_3(VO_4)_2$ hybrid nanorods	Hydrothermal-annealing	2 M KOH	-0.2~0.5	847.2 F·g^{-1}	0.5 A·g^{-1}	99.3% (5000 cycles)	139
3D urchin-shaped $Ni_3(VO_4)_2$ hollow nanospheres	Hydrothermal method	6 M KOH	0.0~0.5	402.8 C·g^{-1}	1 A·g^{-1}	88% (1000 cycles)	141
Co-Incorporated $NiV_2O_6/Ni(HCO_3)_2$ nanoflake grown on nickel foam	Hydrothermal method	6 M KOH	-0.2~0.7	7.94 F·cm^{-2}	1 mA·cm^{-2}	106.2% (10 000 cycles)	145
$NiO/Ni_3V_2O_8$ nanocomposite	Solvothermal method.	—	0.0~0.6	653 F·g^{-1}	1 A·g^{-1}	96% (1000 cycles)	144
$Ni_3V_2O_8$@PANI Composite	Situ chemical bath method	2 M KOH	-0.2~0.6	2565.7 F·g^{-1}	5 mV·s^{-1}	88% (20 000 cycles)	142
$Ni_3V_2O_8$/NG	hydrothermal technique	3 M KOH	-0.1~0.6	1898 F·g^{-1}	1 A·g^{-1}	83.3% (20 000 cycles)	140

$Co_3V_2O_8$–$Ni_3V_2O_8$ nanocomposite	hydrothermal method	6 M KOH	-0.2~0.7	2617.5 $F\cdot g^{-1}$	1 $A\cdot g^{-1}$	91.4% (10 000 cycles)	36
$Co_3V_2O_8$-$Ni_3V_2O_8$ thin layers@porous carbon nanofibers	Hydrothermal method	3 M KOH	-0.1~0.6	1731 $F\cdot g^{-1}$	1 $A\cdot g^{-1}$	85.5% (3000 cycles)	146
Graphene-$Zn_3V_2O_8$ nanocomposites	Solvothermal process	2 M KOH	-1.0~1.0	564 $F\cdot g^{-1}$	0.8 $A\cdot g^{-1}$	85% (5000 cycles)	152
GR/$BiVO_4$	Hydrothermal method	2 M NaOH	-1.1~0.7	479 $F\cdot g^{-1}$	5 $A\cdot g^{-1}$	91% (2500 cycles)	154
rGO/$BiVO_4$	Hydrothermal method	6 M KOH	-1.0~0.6	115 $F\cdot g^{-1}$	0.15 $mA\cdot cm^{-2}$	80.3% (2000 cycles)	155
Li_3VO_4/carbon nanofibers	Solid-state method	Li ion conducting gel polymer electrolyte	0.2~2.0	178 $F\cdot g^{-1}$	0.6 $A\cdot g^{-1}$	86% (2400 cycles)	158

Table 8

Nano-structures (Dimension)	Synthetic method	Electrolyte	Potential window (V)	Maximum SC	Current density	Cycling stability (%)	Ref.
Sulfur-doped V_6O_{13-x} NW (1D)	Two-step process	5 M LiCl	-1.0~0.0	1353 $F \cdot g^{-1}$	1.9 $A \cdot g^{-1}$	47.7% (10 000 cycles)	161
V_6O_{13} sheets (2D)	Thermal decomposing and quenching method	1 M $NaNO_3$	-0.2~0.8	285 $F \cdot g^{-1}$	50 $mA \cdot g^{-1}$	98% (300 cycles)	160
$VOPO_4 \cdot 2H_2O$ (2D)	Reflux method	6 M H_3PO_4	0.0~1.0	184 $F \cdot g^{-1}$	0.2 $A \cdot g^{-1}$	—	162
NC-V_3O_7	In situ photopolymerization method	1 M Na_2SO_4	-0.6~0.2	660.63 $F \cdot g^{-1}$	0.5 $A \cdot g^{-1}$	80.47% (4000 cycles)	159
$VOPO_4$/graphene composite	Hydrothermal method,	1 M H_2SO_4	-0.1~0.9	508 $F \cdot g^{-1}$	0.5 $A \cdot g^{-1}$	80% (5000 cycles)	163
$VOPO_4$/graphene film	Ultrasonication method	PVA/LiCl	0.0~1.2	—	—	96% (2000 cycles)	164
Vanadyl phosphate/rGO nanosheet	Controllable nanosheet reassemble technology	0.5 M K_2SO_4	-0.5~0.3	378 $F \cdot g^{-1}$	0.5 $mV \cdot s^{-1}$	64% (1000 cycles)	165
Vanadyl phosphate/carbon nanocomposites	—	6 M KOH	-0.2~0.7	469 $F \cdot g^{-1}$	1 $A \cdot g^{-1}$	77% (5000 cycles)	166

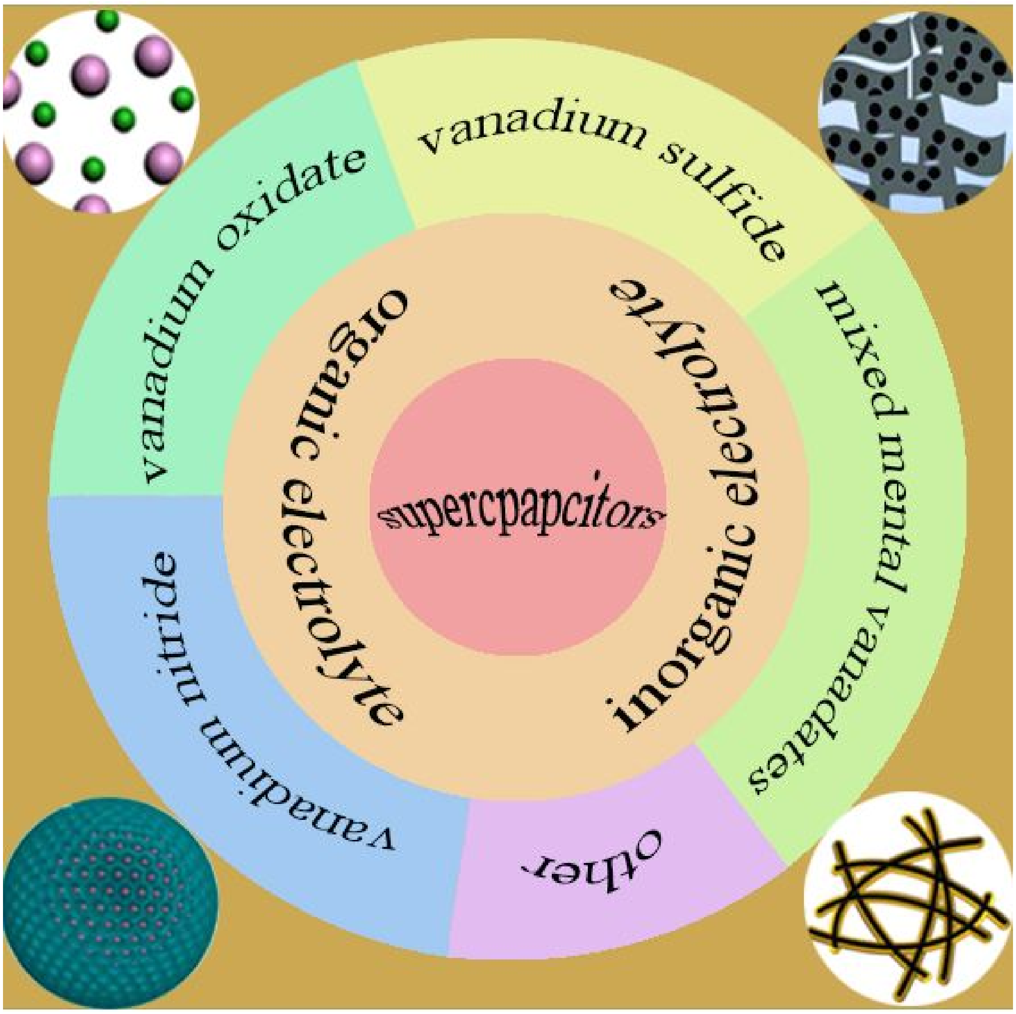
supercpapcitors
organic electrolyte
inorganic electrolyte
vanadium oxidate
vanadium sulfide
mixed mental vanadates
other
vanadium nitride